

Politecnico di Torino







Politecnico di Torino

Master's Degree in Nanotechnologies for ICTs

Exploiting the proximity effect to tune the properties of bilayer superconducting nanowire detectors

Aron Fiore

Student ID: 339433

Supervisors: Prof. Karl K. Berggren
Prof. Dario Daghero

September 2026

Abstract

Superconducting nanowire single photon detectors (SNSPDs) exploit the superconducting state to convert single absorbed photons into measurable voltage pulses. They are increasingly employed in applications such as quantum key distribution, qubit readout, deep space communication, and biomedical imaging. Different materials are used to fabricate these devices, with each material platform offering a distinct balance of performance metrics, including operating temperature, optical absorption, dark counts, maximum count rate, and timing jitter. Because these figures of merit depend on distinct and often competing physical mechanisms, optimizing one metric often entails compromises in others.

This thesis focuses on exploiting the proximity effect by engineering bilayer devices with intermediate properties between those of the starting thin films, allowing us to fine-tune the metrics of our detectors beyond the tradeoffs imposed by using only a single material. The physics of the bilayers was modeled using the Usadel equations, and their sensitivity to light with a set of kinetic equations for nonequilibrium superconductivity. Nanowires of various lengths (1 µm to 1.34 mm) and widths (75 nm to 400 nm) were fabricated on 5 nm-thick bilayers with different contributions of NbN and MoSi.

The devices were tested at cryogenic temperatures (1.3 K to 5.0 K) using continuous-wave lasers at wavelengths of 1550 nm and 780 nm. All detectors exhibited hysteretic current-voltage characteristics, and their single-photon sensitivities were measured. Increasing the NbN contribution resulted in higher switching currents and critical temperatures, whereas the incorporation of MoSi enhanced photon sensitivity. Under the tested conditions, intermediate NbN/MoSi compositions exhibited the highest photon sensitivity at elevated operating temperatures, enabling improved detector performance compared with either constituent material alone.

Acknowledgments

Much of the work presented in this thesis would not have been possible without the technical and human contribution of the friends and collaborators who stood by my side along the way.

I would like to thank Prof. Karl K. Berggren for his guidance during this project, for constantly reminding me of the correct way to conduct scientific research, and for giving me the possibility to work in such a stimulating group.

I would like to thank Prof. Dario Daghero for his timely and precise feedback on this work and for helping me understand how to present frontier research to a broader audience with a diverse background.

I would also like to thank Alejandro Simon for his supervision during this work and for encouraging me to always push my limits a little further. The extensive work documented in these months is the result of this constant motivation.

A special mention goes to the people who contribute to making the Quantum Nanostructures and Nanofabrication Group such a prolific environment to work in. Thank you to Reed Foster for always finding the time to guide me, both in the lab and through the code, and for the continuous interest in my work. Thank you to Ari willner for the help in depositing and characterizing the numerous samples. Thank you to Dorothy Fleischer and Rinske Wijtmans for their help in managing the cumbersome bureaucratic procedures. Thank you to the members of the *E-beamers* for welcoming me onto the team, better luck next time.

I wish to acknowledge the staff of MIT.nano and Characterization.nano for their invaluable support inside and outside the cleanroom, and for making what almost feels like magic happen. A special thanks goes to Aubrey Penn and James Daley.

Thank you to my family for believing in me during this path and for constantly supporting me.

I am extremely grateful to my dear Susanna for always being there when I needed her and for her immense patience during these long and busy years.

Thank you to my MNIS colleagues for the myriad of issues, assignments, exams, and adventures faced together. A special mention goes to the *Triumvirate(+1)*.

Finally, I want to thank all the people who made this period truly unforgettable. Thank you to Davide and Federica M. for the warm welcome and for making me feel at home since the very first moment. A special thanks to the *Salsa pirats*, especially Enrico and Federica I., for the countless snatched meals, bike rides, and capsizes. I am grateful to the volunteers of the MIT Sailing Pavilion and Metropolis for making these months unbelievably fun.

Contents

Abstract **i**

1 Introduction **1**
1.1 SNSPDs . . . 1
1.1.1 The superconducting state . . . 1
1.1.2 Detection process . . . 2
1.1.3 Figures of merit . . . 3
1.2 Proximity effect . . . 10
1.3 Scope and objectives of this thesis . . . 12

2 Theory and modeling **14**
2.1 Usadel equations . . . 14
2.1.1 Material parameters . . . 17
2.1.2 Boundary conditions . . . 18
2.1.3 Switching current . . . 19
2.1.4 Critical temperature . . . 20
2.1.5 Real-axis spectral properties . . . 23
2.1.6 Thickness dependence . . . 26
2.2 Kinetic equations . . . 28
2.2.1 Microscopic description . . . 28
2.2.2 Electron-phonon spectral functions . . . 32
2.2.3 Debye approximation . . . 32
2.2.4 BCS interaction and critical temperature . . . 33
2.2.5 Photon absorption and perturbation time evolution . . . 35
2.2.6 Extraction of the characteristic time constant . . . 37
2.2.7 Energy-equivalent effective temperature . . . 38
2.2.8 Approximations and applications . . . 40

3 Material choice and design **42**
3.1 NbN and MoSi properties . . . 42
3.2 Layout design . . . 43
3.2.1 Positive resist . . . 44
3.2.2 Tapers . . . 46

3.2.3 Booster meanders . . . 47

4 Device fabrication **49**
4.1 Thin film sputtering . . . 49
4.2 Electron-beam lithography . . . 51
4.2.1 Resist spinning . . . 52
4.2.2 Proximity effect correction . . . 52
4.2.3 Development . . . 54
4.3 Etching . . . 55
4.3.1 Overetching and resist burning . . . 56
4.4 Stripping . . . 56
4.5 Wirebonding to a PCB . . . 57

5 Device characterization **60**
5.1 Thickness measurement . . . 60
5.1.1 Ellipsometry . . . 60
5.1.2 Resistance . . . 62
5.1.3 Transmission Electron Microscope . . . 64
5.2 Critical temperature in the MPMS . . . 67
5.2.1 Diffusion coefficient . . . 69
5.3 Scanning Electron Microscope . . . 72
5.4 ICE cryostat . . . 74
5.4.1 I-V curve . . . 77
5.4.2 Dynamic measurements . . . 79
5.4.3 Trigger sweep . . . 80
5.4.4 Linearity check . . . 81
5.4.5 Photon Count Rate . . . 82

6 Discussion **84**
6.1 Critical temperature as function of composition . . . 85
6.2 Switching current as function of composition . . . 87
6.3 Temperature dependence of switching and retrapping currents . . . 89
6.4 Photon sensitivity in the kinetic equations . . . 90
6.4.1 Debye phonon density of states . . . 90
6.4.2 Gap suppression . . . 91
6.4.3 Effective electron and phonon temperatures . . . 93
6.5 Saturation of the photon count rates . . . 94
6.6 Maximum operating temperature . . . 96

7 Conclusions and future work **99**
7.1 Future work . . . 101

List of Figures

1.1 SNSPD detection dynamics 4

2.1 Current density dependence on the superfluid momentum 19
2.2 Bilayer T_c comparison from literature, Usadel solver and experimental measurements 21
2.3 Quasiparticle density of states of the bilayer 25
2.4 Pairing potential of the bilayer 26
2.5 Superconducting gap dependence on temperature and current density . . . 26
2.6 Quasiparticle density of states for a thicker bilayer 27
2.7 BCS modeling of the superconducting gap temperature dependence 34
2.8 Time evolution of the gap suppression 38

3.1 Straight and meandered nanowire shapes 44
3.2 Device layout for positive- and negative-tone resist 45
3.3 Pads layout for positive- and negative-tone resist 45
3.4 Tapers to prevent current crowding 46
3.5 Booster meanders to prevent latching 48
3.6 Layout of the complete devices 48

4.1 Overview of the complete fabrication workflow 49
4.2 Proximity Effect Correction (PEC) 53
4.3 SEM images of the device bonding pads 54
4.4 SEM images of the 5nm NbN sample with critical fabrication results 57
4.5 Wirebonding the sample to the PCB 59

5.1 Detaching the lamella from the sample, following FIB milling 64
5.2 Bright-field TEM imaging of the sample 65
5.3 EDS analysis of the sample 67
5.4 Optical microscope image of the MPMS PCB 68
5.5 Resistance vs temperature at different applied magnetic fields 68
5.6 Critical temperature vs applied magnetic field 71
5.7 Charging effect 73
5.8 SEM images of successfully fabricated devices 73
5.9 SEM images of failed fabrications 74

5.10 Setup in the ICE cryostat 75
5.11 Schematic of the opto-electronic setup for the SNSPDs characterization . . 76
5.12 Hysteretic current-voltage characteristic 79
5.13 Oscilloscope image of the pulse generated by a detection event 79
5.14 Trigger sweep 80
5.15 Linearity check 82
5.16 Photon Count Rate 83

6.1 Thickness dependence of the critical temperature and critical temperature of the bilayers 86
6.2 Switching current density of the fabricated devices 88
6.3 Constriction factor of the fabricated devices 89
6.4 Switching and retrapping currents as function of temperature 90
6.5 Debye phonon density of states $F(\omega)$ for all the bilayers 91
6.6 Gap time evolution for all the samples 92
6.7 Downconversion characteristic time 93
6.8 Electronic and phononic effective temperature 93
6.9 Hyperbolic tangent fits of the measured PCR curves. 95
6.10 Comparison of the saturation parameter σ 96
6.11 Absolute and normalized maximum operating temperature for each bilayer 97
6.12 PCR curve at 4.0 K 98

List of Acronyms and symbols

SNSPD Superconducting Nanowire Single-Photon Detector

BCS Bardeen, Cooper, Schrieffer

DC Direct Current

DC Alternating Current

NbN Niobium nitride

MoSi Molybdenum silicide

PCB Printed Circuit Board

SMP Sub Miniature Push-on

PVD Physical Vapor Deposition

EBL Electron-Beam Lithography

IPA Isopropyl Alcohol

PEC Proximity Effect Correction

RIE Reactive Ion Etching

SEM Scanning Electron Microscope

TEM Transmission Electron Microscope

EDS Energy-Dispersive X-ray Spectroscopy

FIB Focused Ion Beam

EDS Energy-Dispersive X-ray Spectroscopy

MPMS Magnetic Property Measurement System

List of Symbols

Symbol	Description	Unit
Δ	Superconducting energy gap	meV
T_c	Critical temperature	K
ξ	Superconducting coherence length	nm
ℓ	Electronic mean free path	Å
d	Thickness	nm
j	current density	$\mathrm{mA/\mu m^2}$
q	Superfluid momentum	$\mathrm{nm^{-1}}$
I_b	Bias current	µA
I_sw	Switching current	µA
I_dep	Depairing current	µA
C	Constriction factor	dimensionless
L_k	Kinetic inductance	nH
σ	Saturation coefficient	dimensionless
D	Electron diffusion coefficient	$\mathrm{cm^2\,s^{-1}}$
Θ_D	Debye temperature	K
$f(E,t)$	Quasiparticle distribution function	dimensionless
$n(\Omega,t)$	Phonon distribution function	dimensionless
τ_DC	Characteristic energy down-conversion time	ps
T_eff	Effective quasiparticle temperature	K
T_ph	Effective phonon temperature	K

1 Introduction

1.1 SNSPDs

1.1.1 The superconducting state

Some materials, when cooled below a material-dependent critical temperature, transition to a particular state called superconductivity. It is an inherently quantum phenomenon that leads to macroscopic effects, such as zero DC resistance and the expulsion of magnetic field from the material, known as the Meissner effect [1].

According to John Bardeen, Leon Cooper, and Robert Schrieffer (BCS theory [2]), superconductivity arises from an effective attractive interaction between electrons, mediated by lattice vibrations. These dynamics allow electrons near the Fermi surface to bind into pairs known as Cooper pairs. These pairs give rise to a macroscopic quantum condensate that can sustain a dissipationless supercurrent and is described by a single wavefunction. An energy gap Δ opens up in the electronic density of states at the Fermi level, which separates the superconducting ground state from the excitation of quasiparticles. This holds for low enough temperatures such that the thermal excitation is not enough to overcome this gap. The maximum temperature for which we can observe superconductivity in a material is denoted by T_c. The weak-coupling limit holds when the effective attractive interaction between electrons is relatively weak. In this regime, the zero-temperature superconducting gap is related to the critical temperature by

$$2\Delta(0) \approx 3.52\ k_\mathrm{B} T_\mathrm{c} \tag{1.1}$$

A useful macroscopic description of the superconducting condensate is offered by the complex order parameter

$$\Psi(\mathbf{r}) = |\Psi(\mathbf{r})| e^{i\phi(\mathbf{r})} \tag{1.2}$$

where the magnitude $|\Psi|$ represents the local strength of the superconducting condensate, while ϕ is the phase. This order parameter goes to zero when superconductivity is completely suppressed. In the Ginzburg-Landau description [3], spatial variations of the order parameter occur over a characteristic length scale called coherence length ξ. This is the length scale over which superconducting correlations exist and thus plays an important role in nanoscale superconducting structures.

As we approach the critical temperature, the superconducting gap reduces and it completely vanishes at T_c. Below this threshold, the condensate can carry electrical current without dissipation (zero resistance), as long as the current, magnetic field, or deposited energy do not exceed the superconducting pair-breaking limit. This dependence of superconductivity on both the microscopic energy scale and the macroscopic state of the condensate is particularly relevant for single-photon detection.

Superconducting Nanowire Single-Photon Detectors (SNSPDs) are nanostructured devices built from superconducting materials that exploit this sensitivity of the superconducting state to a localized perturbation. They consist of superconducting wires patterned with features on the order of tens to hundreds of nanometers. The detectors are built so that an absorbed photon can locally perturb the superconducting state and trigger a resistive transition. Through the bias and the readout electronics, this process is detected as a voltage pulse.

The combination of high detection efficiency, low dark-count rate, and excellent temporal resolution makes SNSPDs attractive for applications such as quantum key distribution [4][5][6], qubit readout chains [7][8], deep space communication [9][10][11], and biomedical imaging [12][13][14][15]. Different materials offer distinct advantages for SNSPD fabrication and operation, but improving one performance metric often comes at the expense of others. Consequently, no single material simultaneously optimizes all relevant detector properties.

1.1.2 Detection process

The superconducting state can be inhibited by many concurrent processes. Once enough energy is injected into the system (via thermal excitation, the electrical current passing through the material, or the optical absorption of photons), Cooper pairs are broken, and the system transitions into the resistive state. If it is then allowed to relax and dissipate the excess energy, it can revert back to the more stable state of the superconducting condensate. In the case of SNSPDs, the detection process begins with the absorption of a photon by the superconducting nanowire. The photon energy is transferred to the electronic system and subsequently redistributed among the quasiparticles and phonons through a nonequilibrium relaxation. The resulting perturbation locally modifies the superconducting state, and the detailed evolution of this nonequilibrium transition depends on photon energy, bias current, temperature, material properties and nanowire geometry. Additional stochastic effects affect the detection dynamics and several models have been proposed to describe the microscopic detection mechanism [16][17].

The superconducting nanowire is typically biased with a direct current (DC) I_b slightly below the experimentally measured switching current I_{sw}. The superconducting current forced through the device brings it close enough to instability that a single photon absorbed in the material has sufficient additional energy to overcome the superconducting gap Δ and produce a hotspot: this is a localized region in which the order parameter of the

superconducting condensate is suppressed and the material reverts to a resistive state. The bias current is then diverted around the resistive hotspot and keeps flowing in the remaining superconducting sections. Note that at this point, there is still a superconducting path that offers zero resistance, so the voltage measured at the extremities of the nanowire is virtually zero. Due to the hotspot formation, the same bias current is forced to flow in a smaller area, increasing the current density. If in the initial stable conditions we were already close to I_{sw}, this is enough to suppress the superconductivity in the regions around the hotspot where the current was diverted. The hotspot growth causes a further reduction of the superconducting section, producing a positive feedback in the process. Once a sufficiently extended resistive region forms, the bias current is diverted from the nanowire into the external readout circuit. The resulting current distribution produces a voltage drop across the detector, following Ohm's law $V = I_b\, R$. The detector therefore converts the absorption of a single photon into a measurable electrical signal.

After the detection event, the deposited energy is dissipated through several relaxation channels, including electron-phonon interactions, phonon escape into the substrate and thermal diffusion. As the perturbation relaxes, the superconducting state in the nanowire is restored. The device can again support the bias current without any voltage drop and it is ready to detect another photon. The detector must also be electrically designed so that the bias current I_b does not return to the nanowire branch too quickly after the detection event. If this happens before the nanowire has completely relaxed, Joule heating can maintain it in a stable resistive state by continuously dissipating energy with a power $P = RI^2$. This phenomenon is known as latching. More considerations can be found in section 3.2.3.

1.1.3 Figures of merit

The complex detection dynamic of SNSPDs can be characterized by numerous parameters. In the following, we present the key figures of merit that enable us to assess their performances and highlight the highest values demonstrated to date.

The *critical temperature* T_c is the maximum temperature at which the material can still sustain the superconducting state. For SNSPDs, however, the maximum practical operating temperature is often more relevant because it determines the practical conditions required for reliable photon detection. Although a higher T_c can provide a larger thermal margin and relax cooling requirements, it does not necessarily translate into efficient detector operation at higher temperatures. Being able to operate farther below the superconducting transition generally also improves detector performance.
However, T_c also affects photon sensitivity. As explained in sec. 1.1, the critical temperature is directly related to the superconducting gap. Therefore, higher-T_c materials possess a more robust superconducting state, but it is also harder for a low-energy photon to create a strong enough perturbation to trigger a detection event. Consequently, increasing the operating temperature while maintaining high detection efficiency remains challenging. Reliable

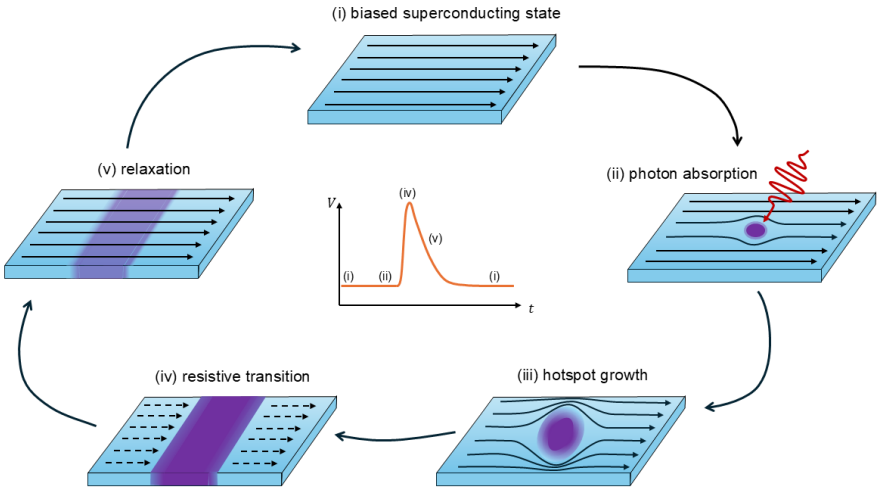


Figure 1.1: SNSPD detection dynamics. (i) In the equilibrium condition, the nanowire is in the superconducting state, biased with a current I_b, and it shows zero electrical resistance. (ii) An absorbed photon deposits energy in the thin film and locally perturbs the superconducting state, generating a hotspot. (iii) The resistive hotspot forces the current lines to bend, causing the current density to increase in the remaining superconducting sections of the nanowire. When it locally reaches a critical value, that region transitions to the resistive state, contributing to the hotpost growth and to the current deviation. (iv) Once the resistive region extends across the whole width of the nanowire there is no zero-resistance path for the current and we observe a voltage drop across the nanowire. (v) After the resistive transition, the excess energy can be dissipated and the nanowire can return to the superconducting state [18].

operation above 4.2 K is particularly attractive: this is the liquid helium temperature, and once this threshold is surpassed the cooling requirements become immensely less demanding. The most common SNSPD materials include polycrystalline nitrides such as NbN [19] and NbTiN [20], which are characterized by relatively high T_c (up to 16 K [21] and 15 K, respectively) and fast reset times. Amorphous materials such as WSi, MoSi and MoGe generally have lower T_c (5 K, 7.5 K, 7.4 K [22] respectively) but can provide high internal detection efficiency and improved long-wavelength sensitivity.
Although SNSPD operation has been demonstrated using MgB_2 [23], which has a bulk critical temperature near 39 K [24], its photon-detection performance remains limited. More broadly, the existence of a high superconducting critical temperature alone does not guarantee efficient single-photon detection at high operating temperatures.

The *switching current* I_{sw} is the experimentally measured current at which the material switches from the superconducting to the resistive state. It is related to the theoretical depairing current, which is the intrinsic current limit of a homogeneous superconducting condensate, beyond which the superflow becomes unstable and superconductivity can no longer be sustained. Microscopically, in the case of type II superconductors, this corresponds to vortex entry in the film [25]. Both NbN and MoSi investigated in this work belong to this class. In ideal conditions, the descriptions provided by the depairing current and vortex-entry barrier disappearance coincide. Real SNSPDs, however, deviate from these predictions because of edge effects, fluctuation-induced switching, current crowding, irregularities in the film, or fabrication-dependent geometric constrictions that cause a

reduction in the cross section. Consequently, the experimentally measured I_{sw} can be lower than the theoretical depairing current. The ratio between these quantities is referred to as the constriction factor C and represents an important indicator when interpreting experimental performances. The switching current is strictly an experimentally measured value: if the nanowire is biased near the threshold, the probability of a spontaneous transition increases with time. The switching current is experimentally determined by gradually increasing the bias current and monitoring the limit value at which the nanowire becomes resistive. A slower increase means keeping the nanowire biased close to the limit of instability for a longer time. The measured I_{sw} can thus also depend on the current ramp rate.
A larger switching current is desired for better electrical readout of the signal. Since the voltage pulses generated during a detection event originate from the bias current diverting into the load, a higher I_{sw} (and, consequently, higher I_b) leads to a larger pulse amplitude. This increases the signal-to-noise ratio and makes it easier to distinguish the pulse from the background amplifier noise. In the same way, a larger switching current can also improve the timing resolution.

The *timing resolution*, or *timing jitter*, quantifies the uncertainty in the measured arrival time of a photon. The total timing jitter of an SNSPD detection system originates from several contributions, that can be divided into extrinsic and intrinsic components.

Extrinsic contributions arise from the measurement system rather than from the microscopic detection process of the superconducting nanowires. Electrical and amplifier noise can shift the threshold-crossing time of the detection pulse. The timing uncertainty associated with voltage noise in the readout arises because the arrival time is typically determined by the crossing of a fixed voltage threshold V_{th} on the rising edge of the detector pulse. In an individual detection event, an instantaneous voltage fluctuation δV shifts the measured crossing time by δt from the nominal threshold-crossing time t_0 [26]. Linearizing the pulse waveform $\overline{V}(t)$ around t_0 leads to

$$\delta t \simeq -\frac{\delta V}{\left.\dfrac{d\overline{V}}{dt}\right|_{t_0}} \tag{1.3}$$

In the small-noise limit, the standard deviation of the noise-induced timing fluctuation can then be written as

$$\sigma_t \simeq \frac{\sigma_V}{\left|\left.\dfrac{d\overline{V}}{dt}\right|_{t_0}\right|}. \tag{1.4}$$

where σ_t is the standard deviation of the distribution of threshold-crossing time arising from the electronic noise, while σ_V is the standard deviation of the voltage-noise distribution. The quantity $d\overline{V}/dt\Big|_{t_0}$ is the slew rate of the rising-edge waveform. Thus, a larger slew rate yields a smaller uncertainty in the threshold-crossing time and, consequently, in the photon arrival time. Increasing the bias current leads to larger pulse amplitude and rising-edge

slope.

A second contribution to the measured timing jitter is geometric jitter. Photon absorption creates a local resistive region that redistributes the bias current and causes a transient voltage perturbation in the nanowire. A superconducting nanowire possesses a kinetic inductance L_{k}, which arises from the kinetic energy of the Cooper pairs carrying the supercurrent. Even though the nanowire has zero DC resistance, its inductive character opposes rapid changes in current. For a sufficiently long nanowire, its non-negligible kinetic inductance means that the device should be considered as a distributed transmission line rather than as a lumped element. The electrical transient therefore propagates at a finite velocity along the nanowire until it reaches its terminals and, consequently, the readout electronics. The time at which the pulse is observed depends not only on the photon-arrival time and on the hotspot-formation dynamics, but also on the distance between the photon-absorption site and the readout terminal [27].

Intrinsic timing jitter originates from stochastic processes occurring during the photon-detection process itself, including the initial down-conversion of the photon energy, the local suppression of superconductivity, and the subsequent growth of a resistive region [16]. These processes lead to event-to-event variations in the detection latency. One such source of variation is given by Fano fluctuations, which are variances in the number of microscopic excitations generated when a fixed amount of energy is deposited in a material, arising from statistical variations in how the energy of an absorbed photon is partitioned between the electronic and phononic systems. In an SNSPD, following photon absorption, the initially excited electrons relax through a stochastic down-conversion cascade that produces both quasiparticles and phonons. The energy retained in the local electronic system determines the number of quasiparticles available to suppress the superconducting order parameter. This dynamics varies from one photon-absorption event to another [17]. The phonons produced during this conversion are not necessarily lost. Phonons with energy greater than 2Δ can break additional Cooper pairs and generate quasiparticles, contributing to the suppression of superconductivity. However, a fraction of the phonon energy can escape into the substrate or diffuse away from the absorption site. Thus, photons with the same initial energy can deposit different amounts of energy into the local quasiparticle system and these fluctuations can contribute to the intrinsic timing jitter. Finally, spatial inhomogeneity provides an additional intrinsic contribution. Local variations in nanowire thickness, disorder, superconducting gap, or critical current modify the energy required to initiate a resistive transition, thus affecting the detection dynamics and consequently the electrical pulse arrival time.

The relative importance of these contributions depends on the detector geometry and operating conditions. In long meandered nanowires, geometric and electronic contributions tend to be more relevant, whereas in short devices fabricated with a high fidelity to the design pattern intrinsic microscopic contributions can become measurable. In the context of the present work, however, timing jitter is not the primary metric used to characterize

our devices. Regarding the broader SNSPD technology, sub-3 ps temporal resolution in photon detection was achieved [28]

Detection efficiency represents the probability that an incident photon actually produces a measurable output pulse. This process can be split into many contributions: the probability that the photon hits the active area of the device, the probability that the photon is absorbed in the superconducting film, and the probability that the perturbation introduced leads to a detection event. The first two contributions consist mainly of optical engineering.

In fiber-coupled SNSPDs, the optical mode from a single-mode fiber has a Gaussian profile. One solution to ensure the maximum possible coupling is to fabricate detectors with larger active area, by employing meander structures. On one hand, this design choice relaxes alignment tolerances and increases the probability that photons land on the active region. On the other hand, this also implies having a longer nanowire. For a uniform wire, the kinetic inductance L_{k} is proportional to the number of squares l/w, where l is the unfolded wire length and w is its width. Since the current-recovery time after a detection event scales approximately as $\tau_{\mathrm{reset}} \simeq L_{\mathrm{k}}/R_{\mathrm{load}}$, large-area meanders generally reset more slowly. Moreover, a longer nanowire length also comes with a higher probability of defects or constrictions, which may greatly reduce the switching current. Thus, the active area must be balanced against speed, fabrication yield and geometric timing jitter.

Photons that reach the active area must still be absorbed in the superconducting thin film. Because the nanowire is only a few nanometers thick, a bare device can exhibit substantial optical reflection and transmission losses. High-efficiency SNSPDs therefore often incorporate optical structures, such as a dielectric spacer and a metallic mirror, that form an optical cavity [29]. The cavity is designed so that the optical field reflected at the nanowire-substrate interface interferes destructively with the field that transmits through the nanowire and is reflected by the mirror. This destructive interference suppresses the net reflected optical field, increasing the absorption in the superconducting film. Such cavity structures can strongly enhance absorptance at a chosen design wavelength. However, the achieved results depend on wavelength, as well as refractive indices and thicknesses of the layers. Consequently, a cavity is commonly optimized for a particular application wavelength.

Finally, the absorbed photons must perturb the superconducting state enough that the hotspot can grow and lead to a complete resistive transition before it can be dissipated. This contribution is called internal detection efficiency and it depends strongly on the microscopic detection process. From a layout design perspective, narrower wires are usually more sensitive to low-energy photons, while wider wires may absorb more total optical power but require a stronger local perturbation to switch. Regarding the composition, materials with lower superconducting gap, lower condensation energy or slower quasiparticle relaxation can require less photon energy to produce a detection event.

Detection efficiencies as high as $99.5^{+0.5}_{-2.07}$ % [30] have been demonstrated.

Dark counts are detection events that occur in the absence of intentionally incident photons. These pulses follow similar dynamics as the normal detection events, meaning a perturbation of the superconducting condensate that leads to a resistive transition. They can originate from intrinsic superconducting fluctuations, such as thermally activated vortex crossings [31][32], quantum phase slips [33][34], and current-induced switching events [18]. They can also arise from extrinsic sources such as stray light, blackbody radiation coupled through the optical fibers, electrical noise, or insufficient thermal and electromagnetic shielding.

The dark count rate is expressed as the maximum number of dark counts detected in a period of 1 s. Experimentally, this is often obtained as the number of dark counts detected divided by the acquisition period.

The dark count rate usually rapidly increases as the bias current I_b approaches the switching current, because the electrical energy injected into the system effectively reduces the height of the energy barrier for a fluctuation-induced transition to the resistive state. SNSPDs operation therefore introduces a tradeoff, as a higher I_b improves detection efficiency, but can also increase the probability of dark counts. In applications where genuine events are intrinsically rare, such as searches for dark matter, even a low dark-count rate can constitute a significant background. Minimizing spurious detection events is therefore essential for preserving the sensitivity and accuracy of the measurement. Dark count rates as low as 6×10^{-6} counts/s [35] (about 1 count per 2 days) are possible.

Wavelength sensitivity of an SNPSD is determined by whether a photon with a specific energy can generate a sufficiently strong local perturbation in the nanowire. The photon energy is related to the wavelength by $E = h\nu = hc/\lambda$, so longer-wavelength photons carry less energy. As anticipated, the device must be biased close to I_sw. The bias determines how small of a local perturbation of the superconducting state is sufficient to drive the nanowire into the resistive state. The closer I_b is to I_sw, the weaker the perturbation required for a detection event. Detection at longer wavelengths is therefore more demanding, since the absorbed photon creates fewer quasiparticles and leads to a weaker suppression of the superconducting state. Moreover, to be able to detect low-energy photons we must bias the device closer to the transition threshold, making it easier for dark count events to occur.

As discussed for the detection efficiency, the maximum detectable wavelength is influenced by material parameters, such as the superconducting gap, the diffusion constant and the condensation energy. Device geometry also plays a role, as narrower and thinner wires are more sensitive to low-energy photons, because a given deposited energy perturbs a more dominant fraction of the nanowire cross-section. This comes at the cost of more delicate and less reliable fabrication processes.

The optical engineering of the device also changes depending on the wavelength, as discussed for the case of optical cavities. Similarly, each material's optical absorption also has a wavelength dependency.

SNSPDs are employed as detectors for a broad range of wavelengths. The visible and near-visible range (400-700nm) is relevant for applications such as fluorescence microscopy [15] and biomedical imaging [13][14], and devices such as quantum emitters [36] and color centers in solids [37][38]. Near-infrared wavelengths (780nm) are used for quantum memories and free-space quantum optics [39]. This wavelength is also often used for benchmarking of detectors' internal efficiency. An especially important application range is the telecommunication wavelengths, and in particular among them the 1550 nm [40]. This wavelength is widely used because standard silica optical fibers have very low attenuation near this value, and so they are the primary choice for long-distance fiber-based quantum communication and quantum key distribution [41][42][43]. Longer wavelengths in the mid-infrared are also increasingly investigated for molecular spectroscopy [44][45][46], because many molecules have vibrational absorption lines in this range. Other applications include gas sensing [47], thermal radiation measurements [48], free-space communication [49]. However, mid-infrared photons carry a significantly lower energy than telecommunication-band photon: the device must be engineered so that even a small deposited energy can trigger the detection event. This favors materials with lower superconducting gap, thinner films, narrower wires and operation closer to the switching current.
Detection up to a wavelength of 29 µm has been published [50].

The *recovery time* (or *reset time*) describes how rapidly the nanowire returns to the superconducting state following a resistive transition that led to a detection event. After a photon-induced hotspot forms, the locally excited quasiparticle population relaxes through electron-electron interactions, electron-phonon coupling, phonon escape into the substrate, and thermal diffusion. During the resistive transition, the direct bias current I_b is diverted into the readout circuit, which typically has a lower resistance (50 Ω) than the resistive nanopatterned wire (~ kΩ). As discussed for the timing jitter, the electrical recovery is then characterized by the kinetic inductance L_k of the nanowire and the impedance of the readout circuit R_{load}, with a time scale of $\tau_{\text{reset}} \sim \frac{L_k}{R_{\text{load}}}$. The kinetic inductance of the device depends both on the material choice and the geometry of the nanowire. Shorter nanowires and materials with lower kinetic inductance generally allow for faster reset times, permitting the device to detect successive photon arrivals and leading to higher count rates. However, the electrical recovery must also be compatible with the thermal relaxation of the quasiparticle population: if the current returns too quickly to the device branch, before the material has had the possibility to sufficiently relax, the detector can latch into a stable resistive state. This means that after the first transition it will just behave as a resistor, and will not be able to detect any successive photon arrival.

1.2 Proximity effect

The superconducting proximity effect occurs when materials with different superconducting properties are brought into good electrical contact. In the resulting hybrid structure, superconducting pair correlations are not strictly confined to one superconducting material, but can diffuse into the adjacent layer [51]. This diffusion of superconducting correlations allows the properties of one material to influence the other, providing a means of engineering superconducting properties that cannot be obtained from either material alone.

The simplest system exhibiting this physical phenomenon is a bilayer consisting of a superconductor and a normal metal. If the two layers are coupled through a transparent interface, superconducting pair correlations extend from the superconducting material into the normal metal over a characteristic length scale related to the coherence length [52, 53]. A transparent interface is an interface whose electrical resistance is sufficiently small that it does not constitute a significant barrier to electronic transmission between the two layers. Microscopically, this requires intimate contact between the materials, with minimal oxidation or contamination of insulating material at the interface. Although the normal metal itself does not have an intrinsic superconducting order parameter, a nonzero pair amplitude can be induced in it by its coupling to the superconductor. At the same time, superconductivity in the respective layer is weakened near the interface because Cooper pairs tend to extend in the normal metal, in a region where the attractive pairing interaction is weaker or nonexistent.

Looking at the mathematical picture, two related but distinct quantities are useful for describing the proximity effect. The superconducting order parameter Δ measures the local strength of the superconducting condensate, and is related to the microscopic pairing interaction. As the system approaches the limit of superconductivity, for example, when the temperature reaches T_c, or when superconductivity is weakened by current, magnetic fields or other pair-breaking mechanisms, the order parameter decreases and vanishes at the resistive transition. The anomalous Green's function F instead describes the presence of Cooper-pair correlations [52]. Their relation can be expressed schematically as

$$\Delta(\mathbf{r}) \propto \lambda(\mathbf{r}) F(\mathbf{r}) \tag{1.5}$$

where $\lambda(\mathbf{r})$ is the local attractive electron-electron interaction responsible for superconductivity. The $\mathbf{r}$ dependence represents how these quantities can vary spatially across a heterostructure. A normal metal does not have attractive interaction responsible for intrinsic superconductivity. In our description, this corresponds to $\lambda = 0$, and thus the superconducting order parameter Δ also vanishes. However, the anomalous Green's function F can remain nonzero in the normal metal due to the propagation of superconducting pair correlations from the adjacent superconducting layer [54]. The proximity effect can be understood as the spatial redistribution of superconducting correlations across an interface.

Disordered superconducting thin films, such as those commonly employed in SNSPDs,

are often described in the dirty limit. This regime is valid when elastic electronic mean free path ℓ is much shorter than the superconducting coherence length ξ, $\ell \ll \xi$. Electrons then undergo many elastic scattering events over the characteristic length scale of superconductivity variations, and their motion can be described as diffusive rather ballistic [52, 54]. In this regime, the relevant material parameter is the electronic diffusion coefficient D_{S}, which characterizes the rate at which electrons diffuse through the disordered superconducting film and therefore determines the spatial extent over which superconducting correlations can propagate. The corresponding material coherence length is given by

$$\xi_S = \sqrt{\frac{\hbar D_S}{2\pi k_{\mathrm{B}} T_{\mathrm{c}}}} \tag{1.6}$$

where $\hbar$ is the reduced Planck constant, D_S is the electronic diffusion coefficient, T_{c} is the superconducting critical temperature and k_{B} is the Boltzmann constant. If the thicknesses of the layers are much larger than their respective coherence lengths, the proximity-induced modifications are confined near the interface. If, instead, the layer thicknesses are comparable to or smaller than the coherence length, superconducting correlations from one material can extend through the entire thickness of the bilayer.

In particular, for ultrathin superconducting bilayers, the Cooper limit is the condition in which the thicknesses of the layers are smaller than the coherence lengths of the respective materials and the interface between the two is sufficiently transparent [51]. When this happens, the pair amplitude is nearly uniform across the whole bilayer stack and the system can be treated approximately as a single effective superconducting film, whose properties are determined by the weighted contributions of the two original materials. Within a simplified weak-coupling treatment, the effective pairing interaction can be written as

$$\lambda_{\mathrm{eff}} = \frac{N_1 d_1 \lambda_1 + N_2 d_2 \lambda_2}{N_1 d_1 + N_2 d_2} \tag{1.7}$$

where N_i, d_i and λ_i are respectively the density of states at the Fermi level, the thickness and the pairing interaction of the layer i [52].
When applied to a bilayer of two different superconductors, the proximity effect produces a mutual averaging of their superconducting properties: the higher-T_{c} material tends to enhance superconducting correlations in the lower-T_{c} material, while the latter suppresses the order parameter and the critical temperature of the former. As a result, the bilayer can exhibit an effective critical temperature, switching current, superconducting gap, and kinetic inductance that is intermediate between that of the two original films. The exact values depend not only on the thicknesses of the two layers, but also on their interaction. The interface transparency, the diffusion constants, the densities of states and resistivities of each material all play a role in the effective resultant hybrid device.

This tunability is hence particularly useful for superconducting nanowire single-photon detectors, whose detection principle relies exactly on a superconducting gap low enough that an absorbed photon can perturb it and provoke a resistive transition, but high enough

that stochastic fluctuations do not alter the state of the device significantly.

1.3 Scope and objectives of this thesis

It is apparent that the SNSPD design and operation is a complex engineering problem, in which many tradeoffs coexist. The device performances are affected by a combination of material properties, device geometry, optical design and operating conditions. As discussed in the previous sections, the optimization of one performance metric often results in the worsening of another.

For instance, increasing the active area can improve the optical coupling and thus the detection efficiency, but it also increases the nanowire length and kinetic inductance, leading to longer reset times and increased timing jitter. Reducing the width of the nanowires can enhance the sensitivity of the detector, but it could also decrease the switching current and negatively affect the fabrication yield. In a similar manner, the choice of the material strongly affects the critical temperature, superconducting gap, switching current, kinetic inductance, and wavelength sensitivity.

Traditionally, many of these tradeoffs were addressed by selecting one specific superconducting material and then optimizing the nanowire geometry and other elements such as optical cavities and the interface with the substrate.

This thesis explores an additional route for engineering SNSPD properties: the use of proximity-coupled superconducting bilayers. This introduces an additional knob to fine tune the performances of our detectors, beyond the possibilities offered by the few standard superconducting materials used to build these devices.

This work focuses on NbN/MoSi (niobium nitride / molybdenum silicide) bilayers, chosen to combine two material platforms with different superconducting and detector properties. The scope is to take advantage at the same time of the higher T_c typical of niobium nitride and the high sensitivity provided by molybdenum silicide. By varying the relative contribution of these materials in a bilayer stack, the goal is to access intermediate superconducting properties and evaluate how these depend on the material structure and how they translate into SNSPD performances.

The scope of this thesis includes the full process, from material selection to device characterization, as well as the theory to model the proximity effect. Firstly, the equilibrium superconducting properties of our devices are modeled using the Usadel equations, and the photon sensitivity is analyzed through BCS kinetic equations. Then, the motivation for choosing NbN and MoSi is discussed in terms of their superconducting properties and demonstrated SNSPD performances. Finally, the device layouts are designed to explore the geometry dependence, and how this propagates on the different compositions.
Detectors with different widths (75 nm to 400 nm), lengths (1 µm to 1.34 mm) and shapes (straight nanowires or meanders) are fabricated on bilayers with compositions ranging from 5 nm of pure NbN to 5 nm of pure MoSi, with 1 nm variations.

The devices are fully characterized at 1.3 K, and an additional temperature sweep up to 5.0 K investigates the maximum temperature for which light and dark counts could be distinguished. The characterization process explores the superconducting transition, current-voltage characteristics and switching current, trigger sweep to extract information about the shape of the pulses, linearity checks to confirm the single photon detection capability and photon count rates. The detection of 780 nm and 1550 nm photons is also compared, to study how the photon energy affects the detection process in our bilayer.

2 Theory and modeling

The objective of this thesis is to exploit the proximity effect to tune the properties of bilayer detectors. Experimentally, this is achieved by depositing very thin films, with thickness comparable to the coherence length, in direct contact. Detector performance is strongly influenced by microscopic material properties, including the superconducting gap, quasiparticle density of states, diffusion coefficient, and critical current. We therefore require a model to determine how proximity-induced modifications of these quantities affect the detection process.
We model the bilayer structures with the Usadel equations, which describe diffusive superconductors in the quasiclassical dirty limit, that is valid when the electron mean free path is much shorter than the superconducting coherence length. The Usadel solver takes as input the material properties and the thicknesses of the two layers, applies appropriate boundary conditions at the interface and at the film surfaces, and computes self-consistently the superconducting properties of the bilayer.

The quantities obtained from the Usadel modeling include the critical temperature of the bilayer, the depairing current, the quasiparticle density of states, and the anomalous spectral pairing function. Since the total film thickness is comparable to or smaller than the superconducting coherence length of the two materials, we expect these properties to vary only weakly across the stack. The bilayer can therefore be treated approximately as a single effective hybrid material, whose properties are used as input to a separate BCS kinetic-equation model to simulate the sensitivity of these detectors to photons.

2.1 Usadel equations

The Usadel equations are formulated starting from quasiclassical Green functions. These provide a compact microscopic description of superconductivity, as they describe both the normal quasiparticle spectrum and the anomalous electron-hole correlations associated with Cooper pairing [55].

In a normal metal, low-energy excitations near the Fermi level are mostly electron-like or hole-like states. In a superconductor, the condensate mixes electron and hole degrees of freedom. The elementary excitations are called Bogoliubov quasiparticles [56], coherent superpositions of electron-like and hole-like components. This coupling requirement opens an energy gap in the single-particle excitation spectrum.

In Nambu-space notation, electron and hole amplitudes are grouped together, and the Green's function can be represented as a matrix

$$\hat{g} = \begin{pmatrix} g & f \\ \tilde{f} & -g \end{pmatrix} \tag{2.1}$$

The diagonal component g is the normal Green's function, which describes the propagation of quasiparticle excitations. It is directly related to the quasiparticle density of states. The off-diagonal component f is the anomalous Green function, which describes superconducting pair correlations.
The superconducting order parameter is instead

$$\Delta(\mathbf{r}) = |\Delta(\mathbf{r})|e^{i\phi(\mathbf{r})} \tag{2.2}$$

The modulus represents the local strength of the superconducting condensate, while ϕ is the superconducting phase. The anomalous Green's function and the order parameter are closely related by self-consistency relations. Physically, this represents how the superconducting pair potential is generated by the pairing correlations of the electrons, and those correlations are themselves determined by the superconducting pair potential.

The Usadel equations are a dirty limit form of the quasiclassical Eilenberger equations [57]. Although the Eilenberger equations are appropriate for clean superconductors and retain information about the quasiparticle momentum direction on the Fermi surface, in dirty films the electronic mean free path is much shorter than the superconducting coherence length ($\ell \ll \xi$). In this dirty limit, impurity scattering rapidly randomizes the quasiparticle momentum direction, and the Green functions become isotropic over the Fermi surface. Under these conditions, the Eilenberger equations reduce to the Usadel equations and the motion of the particles becomes diffusive, rather than ballistic.

The self-consistent superconducting state is often computed on the imaginary-frequency axis (Matsubara axis) for ease of calculation. The fermionic Matsubara frequencies are

$$\omega_n = \frac{\pi k_B T}{\hbar}(2n+1), \qquad n = 0, 1, 2, \ldots \tag{2.3}$$

and the Green functions are evaluated at $i\omega_n$.
We consider a conventional spin-singlet superconductor and neglect the spin-dependent effects. Specifically, we assume that exchange and Zeeman fields, spin-flip scattering induced by magnetic impurities, and spin-active interfacial scattering are negligible [58][59]. Under these assumptions, the quasiclassical Green's functions are spin-degenerate and can be described by the scalar normal and anomalous Green's functions G and F. The Usadel equation can then be written as

$$\hbar D \nabla \cdot (G\nabla F - F\nabla G) + 2\Delta G - 2\hbar\omega_n F = 0 \tag{2.4}$$

In this equation, $G(\boldsymbol{r}, i\omega_n)$ is the normal Green's function, $F(\boldsymbol{r}, i\omega_n)$ is the anomalous Green's function, D is the diffusion coefficient, and $\Delta(\boldsymbol{r})$ is the superconducting order parameter.
The Green's functions must satisfy the normalization condition

$$G^2 + FF^* = 1 \tag{2.5}$$

which expresses the conservation of quasiclassical spectral weight between normal and anomalous components.
The diffusion equation must also be solved together with the self-consistency equation for the order parameter:

$$\Delta \ln\left(\frac{T}{T_{c0}}\right) + 2\pi k_B T \sum_{\omega_n > 0} \left(\frac{\Delta}{\hbar\omega_n} - F\right) = 0 \tag{2.6}$$

This equation shows that the order parameter Δ is generated by the anomalous Green function F summed over all positive Matsubara frequencies. The sum in turn depends on the order parameter through $\Delta/\hbar\omega_n$.
The Usadel equation is then solved using a trigonometric parametrization, under which the components become

$$G(z, i\omega_n) = \cos\theta(z, i\omega_n) \tag{2.7}$$

$$F(z, i\omega_n) = e^{i\chi(z, i\omega_n)} \sin\theta(z, i\omega_n) \tag{2.8}$$

This allows the normalization condition to be automatically satisfied.

In our modeling, the bilayer is treated as a one-dimensional structure, along the film thickness direction z. The current is set to flow in plane with the interface, as in our actual nanowires.
We can define the gauge-invariant superfluid momentum as

$$q = \nabla\phi - \frac{2\pi}{\Phi_0}\mathbf{A} \tag{2.9}$$

where ϕ is the phase of the order parameter (2.2), $\Phi_0 = h/2e$ is the superconducting flux quantum and $\mathbf{A}$ is the vector potential. In our case, we do not consider an applied magnetic vector potential, so q is just the superconducting phase gradient.

For a uniform current flowing in the plane of the bilayer, we assume that the magnitude of the pairing angle varies only across the bilayer thickness ($\theta = \theta(z)$), whereas the superconducting phase ϕ has a constant in-plane gradient q. The Usadel equation then becomes

$$\hbar D \frac{\partial^2\theta}{\partial z^2} - \left(2\hbar\omega_n + \hbar D q^2 \cos\theta\right)\sin\theta + 2|\Delta|\cos\theta = 0 \tag{2.10}$$

where the term proportional to q^2 describes the current-induced pair breaking. A finite phase gradient corresponds to a finite condensate momentum, and therefore increases the kinetic energy of the superconducting condensate. As q increases, the order parameter,

spectral gap and superfluid density are suppressed. The maximum of the supercurrent defines the bilayer's intrinsic homogeneous depairing current.

2.1.1 Material parameters

We first need to model our bilayer, defining the thickness of each layer d_i and their material properties, such as the electron density n, resistivity ρ, and critical temperature T_c. From these quantities, the solver computes other quantities needed for the Usadel calculation. The conductivity is simply

$$\sigma = \frac{1}{\rho} \tag{2.11}$$

Assuming a free-electron-like metal, we can then apply the Drude model [60] to compute the Fermi wavevector from the electron density as

$$k_F = (3\pi^2 n)^{1/3} \tag{2.12}$$

and the Fermi velocity is

$$v_F = \frac{\hbar k_F}{m_e} \tag{2.13}$$

If the film thickness becomes comparable to microscopic electronic length scales, the electron density n can differ from the bulk reference value due to strain and surface or interface effects. For the film thicknesses considered here, such deviations are not expected *a priori*. However, while experimentally verifying the electronic density of states would require more elaborate setups, we can get electronic transport measurements from our sample that allow us to extract the diffusion coefficient D and the resistivity ρ. When the diffusivity and the resistivity are known, the effective electron density of our sample can be inferred using the Drude model. The relation between the scattering time τ, electron mass m_e, electron density n, electron charge e and resistivity ρ is

$$\tau = \frac{m_e}{ne^2\rho} \tag{2.14}$$

The diffusion coefficient in three dimensions is

$$D = \frac{1}{3} v_F^2 \tau \tag{2.15}$$

Finally, plugging 2.12 into 2.13, and the result into 2.15, we can obtain the diffusion coefficient as a function of the electron density. Since we can extract D from measurements, solving for n we get

$$n = \left[\frac{\hbar^2 (3\pi^2)^{2/3}}{3e^2 \rho m_e D} \right]^3 \tag{2.16}$$

This relation should be interpreted as a free-electron estimate, to assign an electron density to our materials consistent with our experimental results. This is useful because the boundary conditions at the interface directly depend on the Fermi velocities of the two

materials, which are in turn function of n.

2.1.2 Boundary conditions

The next step in the Usadel equations is to impose the boundary conditions. Our system consists of two superconducting layers, whose external surfaces are in contact with isolating surroundings, while the internal interface is transparent. At outer boundaries, vacuum boundary conditions are applied, meaning that no spectral current flows out of the film [61]. In the trigonometric parametrization we are employing, this results in a homogeneous Neumann condition at the top and bottom surfaces

$$\frac{\partial \theta}{\partial z} = 0 \tag{2.17}$$

At the interface between the two superconducting layers, quasiclassical boundary conditions are applied, to enforce conservation of spectral current. The quasiparticles can be transmitted or reflected, with a probability that depends on the angle of incidence, the Fermi velocity mismatch of the two materials and a possible interfacial scattering potential [62].
The additional interface barrier can be modeled as a delta-function potential [63, 64]

$$U(z) = U_0 \delta(z) \tag{2.18}$$

Because the bilayers in this work were deposited *in situ*, without breaking vacuum, the interface is expected to be clean, and so the explicit interface barrier is taken to be zero ($U_0 = 0$). However, this does not mean that the interface is perfectly transparent, as reflection can still occur due to Fermi-velocity mismatch between the two materials.
The angle-dependent transparency used as boundary condition is

$$\mathcal{T}(\varphi_1, \varphi_2) = \frac{v_{F1} v_{F2} \cos\varphi_1 \cos\varphi_2}{(U_0/\hbar)^2 + \left(v_{F1}\cos\varphi_1 + v_{F2}\cos\varphi_2\right)^2/4} \tag{2.19}$$

where φ_1 and φ_2 are the angles of incidence on the two sides of the interface. Conservation of linear momentum on the direction parallel to the interface requires

$$v_{F1} \sin\varphi_1 = v_{F2} \sin\varphi_2 \tag{2.20}$$

The solver then performs an angular average over the allowed incidence angles to account for the fact that quasiparticles incident at different angles face different transparencies. The resulting boundary condition hence determines how efficiently anomalous superconducting correlations can pass between the two materials of the bilayer.

In the low-transparency limit, this kind of interface can be reduced to an effective interface resistance×area product $A\,R_b$, following Kupriyanov-Lukichev boundary conditions [65], particular case of the more general Tanaka-Nazarov boundary conditions [66][67].

This value is determined from the material properties and the assumed value of U_0.

2.1.3 Switching current

Once all the necessary parameters are set, we need to compute $\theta(z, i\omega_n)$ and $\Delta(z)$ by solving the Usadel equation and the self-consistency equation. This is done on the imaginary axis because the Green's functions are smooth and the self-consistency equation is well-behaved. Avoiding the technicalities of the computations, the main point is that the solver provides a self-consistent microscopic calculation of the bilayer superconducting state, using the layer parameters and the interface model.

The supercurrent density can then be computed as a function of the superfluid momentum q. For in-plane current flow, the current density related to the trigonometric-parametrized anomalous Green's function is [61]

$$j(z) = 4\pi e k_B T N_0 D q \sum_{\omega_n > 0} \sin^2 \theta(z, i\omega_n) \tag{2.21}$$

The numerical results obtained are then plotted as the normalized current density j/j_0 as a function of the normalized superfluid momentum $q\,\xi_0$. The normalization is carried out referencing to the higher-T_c material, in our case NbN.

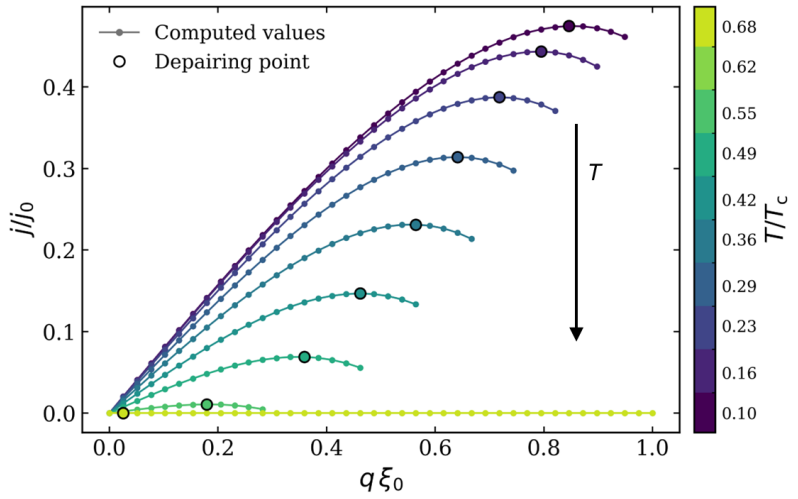


Figure 2.1: Current density dependence on the superfluid momentum, at different temperatures, simulated for a 5 nm bilayer composed of 2 nm of NbN and 3 nm of MoSi. The current density is normalized to the depairing current density of NbN, and the temperature is normalized to the critical temperature of NbN.

At small q, the supercurrent density increases approximately linearly with the superfluid momentum ($j \propto q$). In this regime, the superconducting condensate is only weakly perturbed by the current and its superfluid density is approximately independent of q. As q is increased, the kinetic energy associated with the condensate flow induces pair breaking and suppresses the order parameter. As a consequence, the superfluid density decreases and the current no longer increases linearly [68]. The maximum of the $j(q)$ curve thus defines the homogeneous depairing current density of the ideally spatially uniform

superconducting state[69]. If we were to try and increase the current, it would actually weaken the state even more, meaning the current itself could not be sustained.
This computation is repeated at different temperatures. At lower temperatures, the superconducting order parameter and superfluid density are larger because fewer thermally excited quasiparticles are present, resulting in the capability to sustain a larger supercurrent before reaching the depairing limit. As the temperature approaches the critical temperature of the bilayer, the order parameter and superfluid density decrease and, with them, the maximum sustainable current, as well as the corresponding superfluid momentum.

2.1.4 Critical temperature

The effective critical temperature of our bilayer is extracted from the temperature dependence of the calculated current density. In the present work, T_c is defined as the temperature at which the calculated current density $j(q)$ vanishes for all values of the phase gradient q. This definition corresponds to the disappearance of the superconducting state.

The calculation of T_c through the self-consistency equation requires an intrinsic critical temperature T_{c0} to be specified for each constituent material. Initially, the modeling was performed using the critical temperatures experimentally measured for the nominally 5 nm NbN and MoSi films. The bilayers considered in this work have a total thickness of 5 nm, with intermediate compositions of 1+4, 2+3, 3+2 and 4+1 nm of NbN and MoSi respectively. Using the critical temperatures obtained from the 5 nm reference films as the intrinsic material parameters resulted in computed bilayer critical temperatures that were systematically higher than the experimentally measured values.
As an independent first comparison, the bilayer critical temperature was also estimated using the analytical expression discussed by Zhao et al. [70] for thin superconducting bilayers

$$T_c = \exp\left[\frac{H_S \ln(\Theta_{D,S}) + H_{S'} \ln(\Theta_{D,S'}) - 1}{H_S + H_{S'}}\right] \tag{2.22}$$

where S and S' denote the two superconducting materials (in our case, NbN and MoSi), $\Theta_{D,S}$ and $\Theta_{D,S'}$ are their Debye temperatures and H_S and $H_{S'}$ are factors introduced to account for the weighting of the two layers, depending on their material properties and on the thicknesses. The expression is derived in the thin-film or Cooper limit [71], where the layers are sufficiently thin compared to their coherence length, that the superconducting pair amplitude can be considered approximately uniform across the stack, as in our samples.

For the present bilayer system, the calculated critical temperature increases monotonically with the NbN composition. Within the compositions considered in this work, the resulting T_c values are bounded by the critical temperatures of the two pure films and vary smoothly between these limiting cases, approaching the arithmetic mean between the weighted contributions. The Usadel calculation and the analytical expression (eq. 2.22)

give comparable results when the 5 nm experimental critical temperatures are used as the intrinsic material parameters. This agreement indicates that the proximity coupling implemented in the Usadel model produces a behavior consistent with the established theory of thin superconducting bilayers.

However, both approaches systematically overestimate the experimentally measured critical temperatures of the bilayers. This discrepancy indicates that the critical temperatures of the individual ultrathin layers cannot be represented adequately by the values measured for the 5 nm reference films. The proximity effect alone does not account for the experimentally observed T_c values and the intrinsic superconducting properties of each layer must first be calibrated as a function of the thickness.

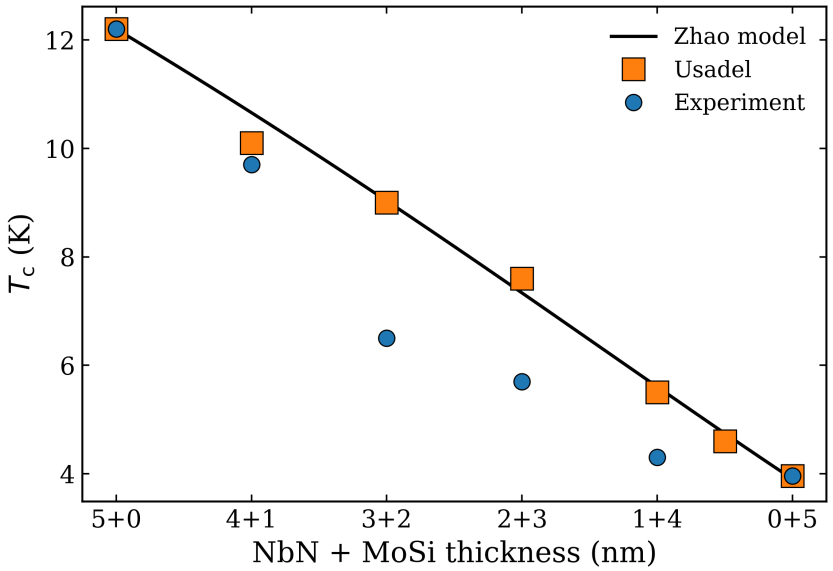


Figure 2.2: Comparison of the critical temperature of the bilayer as function of the composition, obtained from the modeling of eq.2.22, Usadel solver and experimental measurements.

When interpreting the results shown in figure 2.2, it is important to note the plot misses error bars. The critical temperature determination is a consistent measurement, meaning that the uncertainty on the vertical axis is minimal. However, the true deposited thickness for our bilayers is not accurately known (see section 5.1), and a significant tolerance in the x-axis positioning should be considered.

The suppression of T_c with decreasing film thickness is actually a well-established phenomenon in ultrathin superconducting films [72]. Several mechanisms can contribute to this dependence, including variations in structural disorder and grain structure, stoichiometry, electronic density of states, electron-phonon coupling, and electron-electron interactions [73]. In ultrathin NbN films, for instance, a systematic reduction of T_c with decreasing film thickness has been observed, with the intensity of the suppression being correlated with disorder and sheet resistance [74]. Structural changes and variations in the electronic and phononic properties can also become important when the thickness approaches the characteristic superconducting length scale [75].

To account for this intrinsic thickness dependence, the suppression of the critical

temperature was modeled separately for NbN and MoSi. For each material, experimental transition temperatures were available for three representative thicknesses: a thick bulk-like film, the 5 nm reference film and a thinner calibration film of approximately 3 nm. The following stretched-exponential form was adopted:

$$T_c(d) = T_{c0} - \Delta T_c \exp\left[-\left(\frac{d}{\ell}\right)^P\right] \tag{2.23}$$

where T_{c0} is the bulk critical temperature, ΔT_c is the maximum suppression amplitude, ℓ is a characteristic recovery thickness, P is the stretching exponent, and d is the film thickness. This form allows us to model a monotonic suppression of T_c as the film thickness decreases, asymptotically approaching the bulk value for thick films.

The bulk-like reference value used in the fits comes from bibliographic references of similar material depositions. Ideally, we would like to deposit a thick film employing our precise process, to obtain a more accurate estimation of the limit critical temperature.

The stretched-exponential dependence in eq. 2.23 is used as a phenomenological interpolation, rather than as a microscopic theory of superconductivity in ultrathin films. Its purpose is to provide a compact representation of the experimentally observed thickness dependence, with the aim of determining the intrinsic input parameters required by the Usadel calculation.

Nevertheless, the use of a strongly nonlinear dependence on thickness is physically motivated by the exponential dependence of the superconducting temperature on microscopic pairing parameters. In the weak-coupling BCS [2] approximation,

$$T_c \sim \omega_D \exp\left[-\frac{1}{N(0)V}\right] \tag{2.24}$$

where ω_D is the Debye frequency, $N(0)$ is the electronic density of states at the Fermi level, and V is the effective attractive pairing interaction [1].
In a more refined description of phonon-mediated superconductivity, the McMillan equation [76] yields

$$T_c = \frac{\Theta_D}{1.45} \exp\left[-\frac{1.04(1+\lambda)}{\lambda - \mu^*(1+0.62\lambda)}\right] \tag{2.25}$$

where Θ_D is the Debye temperature, λ is the electron-phonon coupling parameter, and μ^* is the Coulomb pseudopotential.

The equations above do not contain the film thickness explicitly. However, in ultrathin film regime, the microscopic quantities entering these expressions can themselves become thickness-dependent and thus have an impact on the resulting T_c. In particular, quantum confinement, disorder, changes in the electronic structure and phononic environment can renormalize the density of states $N(0)$ and the effective electron-phonon coupling λ [75]. Disorder-enhanced electron-electron interactions can additionally modify the effective pairing interaction and Coulomb pseudopotential [77]. Consequently, the thickness

dependence of T_c arises not from an explicit geometric term in the BCS or McMillan formulas, but through the thickness dependence of the microscopic parameters entering them.

This provides a physical motivation for the exponential-like phenomenological dependence proposed, while not implying that 2.23 is the rigorous microscopic form of $T_c(d)$. The actual dependence is expected to depend on the specific material, disorder level, stoichiometry and growth condition [78].

The exponent P in eq.2.23 provides additional flexibility to reproduce a dependence that may not be characterized by a single recovery length. The stretched-exponential is in fact characteristic of systems that relax through multiple channels, each with its own dynamics [79]. In a real ultrathin film, disorder, structural and grain nonuniformity, and thickness fluctuations can introduce spatially varying superconducting properties. The presence of multiple characteristic length scales can therefore produce an effective dependence that differs from a simple exponential law, and that can be modeled by adding the exponent P. This interpretation is particularly relevant when comparing NbN and MoSi, as the former is typically polycrystalline, whereas amorphous MoSi lacks long-range crystalline order and is characterized by isotropic averaged properties. The difference in structural morphology may contribute to the different thickness dependence observed experimentally, although the present data are not sufficient to uniquely identify the microscopic origin of the fitted exponent function.

Finally, after fitting $T_c(d)$ separately for NbN and MoSi, the resulting functions were used to assign the intrinsic critical temperatures of each layer in the Usadel solver for the thicknesses ranging from 1 nm to 4 nm. With this thickness-corrected input parameters, the critical temperatures predicted by the Usadel closely reproduce the experimental measurements. This agreement indicates that the discrepancy observed when using the 5 nm reference values originates primarily from the intrinsic thickness dependence of the constituent films. Once this dependence is accounted for, the bilayer can consistently be described by the diffusive proximity effect framework implemented by the Usadel equations.

2.1.5 Real-axis spectral properties

From the Matsubara-axis (imaginary axis) calculation, the self-consistent order parameter $\Delta(z)$ is obtained. However, spectral quantities such as the quasiparticle density of states are defined on the real-energy axis. We perform the analytic continuation from imaginary Matsubara frequencies to real energies ($\hbar\omega_n \to -iE$) and solve for the retarded Green functions. In the trigonometric parametrization, these are written as

$$G^R(z, E) = \cos\theta(z, E) \tag{2.26}$$

$$F^R(z, E) = \sin\theta(z, E) \tag{2.27}$$

These real-axis calculations are performed for selected values of temperature and

current density. In practice, the current-momentum relation $j(q)$ is first calculated, after which a specific operating point is selected. The real-axis Usadel equations are then solved at the corresponding temperature and superfluid momentum.

The normalized quasiparticle density of states, in trigonometric parametrization, is obtained directly from the retarded normal Green function

$$\frac{N(z,E)}{N_0} = \mathrm{Re}\left[\cos\theta(z,E)\right] \tag{2.28}$$

This quantity expresses the number of available single-particle states at energy E, normalized to the normal-state density of states N_0 of the highest-T_c material (NbN in our case).

We treat the density of states near the Fermi level as approximately constant on the energy scales of superconductivity, giving $N(E)/N_0 \simeq 1$. In a conventional homogeneous BCS superconductor, the quasiparticle density of states is

$$\frac{N(E)}{N_0} = \mathrm{Re}\left[\frac{E}{\sqrt{E^2-\Delta^2}}\right] \tag{2.29}$$

This expression is zero for $|E| < \Delta$,, diverges to $+\infty$ at $|E| = \Delta$, and then decreases towards the normal-state value for higher energies. Hence, in the ideal BCS picture, superconductivity suppresses the low-energy quasiparticle states and redistributes the spectral weight near the gap edge.

The ideal BCS singularity is a consequence of the assumptions of a homogeneous, equilibrium superconductor characterized by infinitely long quasiparticle lifetime. However, real materials generally deviate from these assumptions. Finite quasiparticle lifetimes, pair-breaking processes, disorder, and spatial inhomogeneities can cause a smearing in the coherence peak, as well as introducing a finite density of states below the nominal superconducting gap [80]. A commonly used phenomenological description of this broadening is provided by the Dynes density of states [81, 82]

$$\frac{N(E)}{N_0} = \mathrm{Re}\left[\frac{E+i\Gamma}{\sqrt{(E+i\Gamma)^2-\Delta^2}}\right] \tag{2.30}$$

where Γ is an empirical smearing parameter. The Dynes formulation should be regarded as a phenomenological parametrization rather than a microscopic theory of the origin of the spectral broadening. The parameter Γ allows to account for a finite quasiparticle lifetime or other broadening mechanisms without explicitly modeling their microscopic origin. In particular, different physical mechanisms can lead to a similar broadening in the spectrum and therefore cannot, in general, be uniquely identified from a Dynes fit alone.

In the present Usadel calculation, the spectral modification of the superconducting state is not imposed through the phenomenological model, but obtained directly from the microscopic Green's functions. Both proximity coupling and the presence of a finite

superfluid momentum modify the spectral functions and therefore the density of states. As the current increases towards the depairing limit, the superconducting gap is reduced and the coherence peak becomes less pronounced, reflecting the suppression of superconductivity by the current-carrying state.
This effect is particularly relevant for SNSPD operation because the detectors are typically biased close to their switching current. The superconducting state is therefore already weakened before photon absorption. The relevant density of states for photon detection is the current-carrying state.

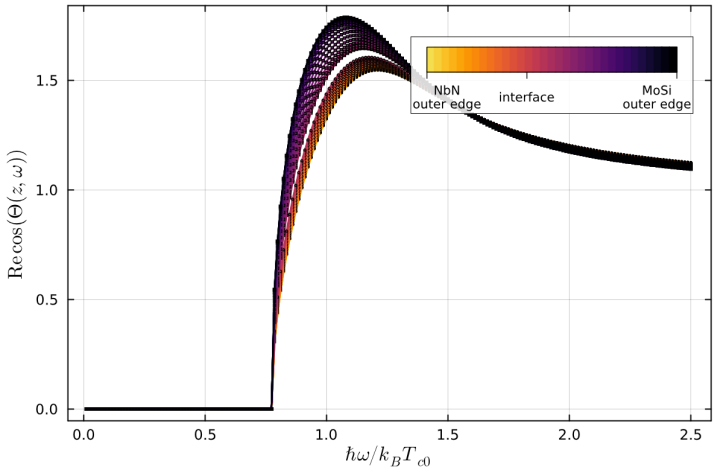


Figure 2.3: Quasiparticle density of states computed for the bilayer composed of 2 nm of NbN and 3 nm of MoSi, at a temperature of 1.3 K and a current density equal to 75% of the depairing current density of the bilayer at that temperature. The x axis shows the energy normalized to thermal energy associated to the critical temperature of NbN. The y axis is normalized to the normal-state density of states.

The imaginary part of the anomalous Green's function $F^R(z, E)$ is a measure of superconducting pair correlations. In a simple BCS superconductor, the anomalous Green's functions has the form

$$F^R(E) \sim \frac{\Delta}{\sqrt{E^2 - \Delta^2}} \tag{2.31}$$

Similarly to the density of states, this quantity is zero for energies below the superconducting gap and presents a peak at that precise position. It then decays at high energies following $\sim\Delta/E$.

This function measures how strongly quasiparticle states at energy E have coherent electron-hole mixing, which is the Green-function representation of superconducting pairing.

Let us now summarize the various quantities introduced in these sections. The density of states tells us how many quasiparticle states exist at a given energy, while the anomalous function tells us how strongly superconducting electron-hole coherence is present at each of those energies. The order parameter Δ is instead determined self-consistently from the anomalous correlations and it describes the local condensate strength and phase.

The effect of both an increase in temperature and in the superconducting current j

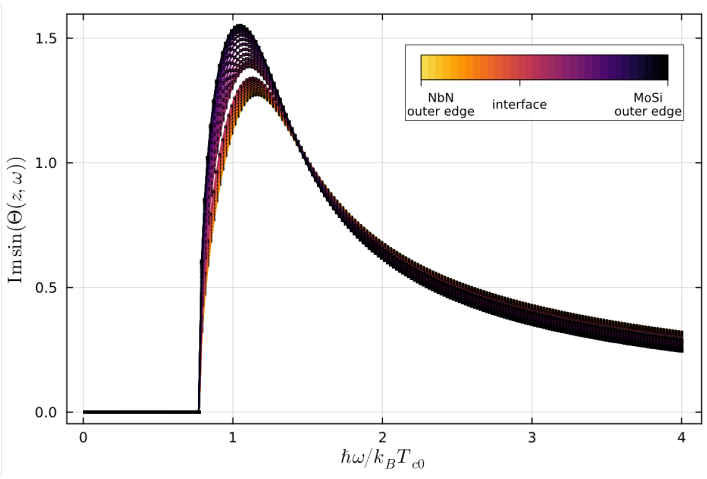


Figure 2.4: Pairing potential computed for the bilayer composed of 2 nm of NbN and 3 nm of MoSi, at a temperature of 1.3 K and a current density equal to 75% of the depairing current density of the bilayer at that temperature. The x axis shows the energy normalized to thermal energy associated to the critical temperature of NbN. The y axis is normalized to the normal-state density of states.

is to cause a smearing in the coherence peak and suppress the superconducting gap Δ. These two effects can act independently or combine, as they consist in different ways to inject energy into the system.

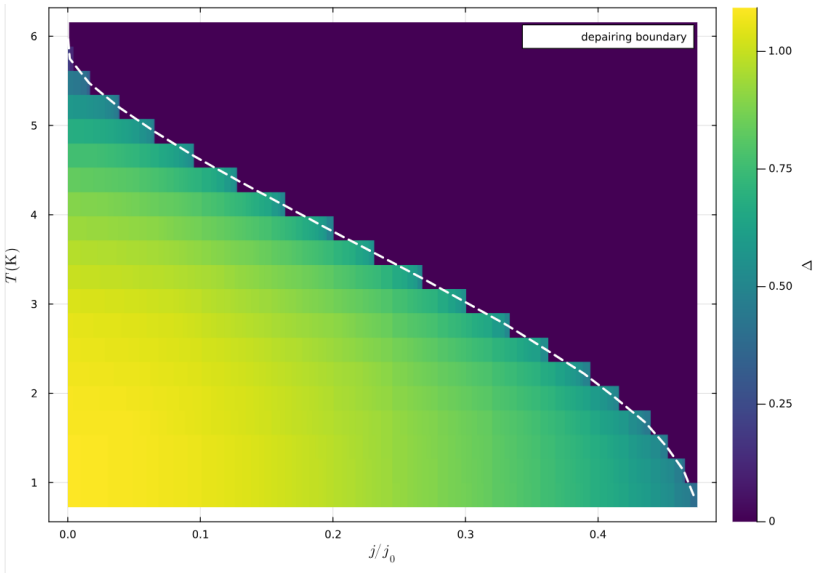


Figure 2.5: Color map showing the magnitude of the superconducting gap Δ as a function of the material temperature T and of the normalized superconducting current density j/j_0. The white boundary highlights the limits of the superconducting condensate.

2.1.6 Thickness dependence

An important point about our modeling is the possibility to observe how the properties of the bilayer change across the position z in the stack.

In our geometry, the bilayer is modeled across the thickness direction z, while the bias current flows in plane with the interface. Therefore, the superfluid momentum q is parallel to the layers and is common to the whole current-carrying bilayer. In principle,

the local current density can depend on position through the local material parameters and Green functions, so that different regions of the stack contribute differently to the total current. However, the current density we are interested in, which is in turn related to the experimental switching current, is obtained by integrating the local current density across the bilayer thickness. Thus, the plotted j/j_0 vs $q\ \xi_0$ does not present a position dependence, as it represents the current response of the bilayer as a single superconducting structure.

Different considerations can be made for the real-axis spectral quantities, such as the density of states and the pairing potential. These quantities are local functions of both energy and position (eq. 2.7, 2.8) and therefore allow us to examine how the superconducting spectrum evolves across the stack. The two materials can have different local gaps, coherence peaks and pairing correlations. For the 5 nm-thick bilayers we built, the predicted variation across the stack is very small (Fig. 2.3, 2.4) and the curves corresponding to different positions z across the stack almost overlap. This indicates that the total thickness is sufficiently small, compared to the superconducting coherence lengths, that the proximity effect averages the superconducting properties across the whole bilayer, which behaves as a single homogeneous hybrid superconductor.

By contrast, if the total thickness is increased beyond the coherence length scale of the materials, the spatial dependence becomes evident. In thicker simulated structures, such as 10 nm of NbN and 15 nm of MoSi, the density of states and pairing potential clearly evolve from the behavior of one material to that of the other, showing intermediate proximity-coupled behavior near the interface.

Therefore, the thickness dependence provides a useful consistency check for the effective-material approximation. For the experimentally relevant 5 nm bilayers, the reduced spatial variation justifies treating the stack as one hybrid superconducting film with mediated properties.

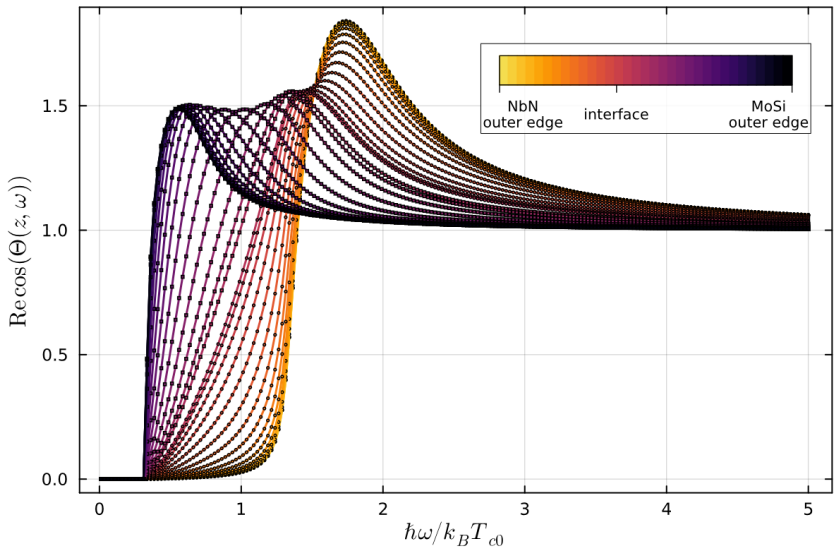


Figure 2.6: Quasiparticle density of states simulated for a bilayer composed of 10 nm of NbN and 15 nm of MoSi. The color gradient shows the spatial variation of the properties across the thickness of the stack.

2.2 Kinetic equations

Photon detection in a superconducting nanowire is an intrinsically nonequilibrium process. Before photon absorption, the superconducting condensate, the quasiparticle population, and the photons are in thermal equilibrium with the cryogenic environment. The absorption of an optical photon then transfer into a microscopic region of the nanowire an energy much larger than the superconducting gap. This energy is redistributed among electronic excitations and lattice vibrations, producing quasiparticle and photon populations that suppress superconductivity.

The equilibrium properties of a superconductor are described by Bardeen-Cooper-Schrieffer theory [2] or, when strong electron-phonon coupling must be included in the modeling, by Migdal-Eliashberg theory [83, 84]. In our treatment of spatially inhomogeneous superconductors in the dirty limit, the equilibrium spectrum can be obtained from the Usadel equations. At equilibrium, the quasiparticle and phonon populations are determined by the temperature and the order parameter is obtained from the self-consistency equation (eq. 2.6). This description is sufficient for material-specific properties such as the critical temperature, energy gap and critical current. It is not sufficient, however, to describe the evolution after a photon is absorbed. The Usadel description assumes thermal occupation of the quasiparticle and phonon states, whereas the deposited energy drives both distributions far from equilibrium [85]. The subsequent transfer of energy between quasiparticles, Cooper pairs, phonons, and the substrate determines the temporal evolution of superconductivity suppression. Kinetic equations describe how particles are distributed over energy and how they evolve in time [86]. The quasiparticle distribution $f(E,t)$ gives the occupation probability of a quasiparticle state at energy E. The phonon distribution $n(\Omega,t)$ gives the occupation probability of a phonon mode at energy Ω. The kinetic equations calculate the rates of change of these two distributions [87]. Once these are known, they can be used to calculate observables such as the nonequilibrium particle density, characteristic relaxation times and the response of the material to photons at different energies.

2.2.1 Microscopic description

At thermal equilibrium, the quasiparticle occupation is described by the Fermi-Dirac distribution

$$f_{\mathrm{eq}}(E,T) = \frac{1}{\exp(E/k_{\mathrm{B}}T)+1} \tag{2.32}$$

where the quasiparticle energy is measured relative to the chemical potential [88]. The equilibrium phonon occupation is described by the Bose-Einstein distribution [89]:

$$n_{\mathrm{eq}}(\Omega,T) = \frac{1}{\exp(\Omega/k_{\mathrm{B}}T)-1} \tag{2.33}$$

Following a perturbation, the two distributions can be written as

$$f(E,t) = f_{\mathrm{eq}}(E, T_{\mathrm{bath}}) + \delta f(E,t) \qquad n(\Omega,t) = n_{\mathrm{eq}}(\Omega, T_{\mathrm{bath}}) + \delta n(\Omega,t) \quad (2.34)$$

Where T_{bath} is the cryogenic bath temperature, δf and δn are the excess nonequilibrium populations. In general, both deviations from the equilibrium cannot be described simply by an increase in temperature, as an absorbed photon initially produces strongly nonthermal structures in the energy space. For example, two distributions may lead to the same total energy while distributing it in very different regions of the quasiparticle spectrum. A large population near the superconducting gap and a smaller population at higher energy do not suppress the superconducting state in the same way, even if their total energies are equal. Moreover, quasiparticles and phonons at different energies participate in scattering, pair breaking and recombination at different rates. The kinetic equations retain this energy dependence and therefore provide more information than a model simply based on a single electronic temperature.

The quasiparticle and phonon collision integrals can be derived from microscopic electron-phonon interaction using transition probabilities described by Fermi's golden rule [85], taking into account superconducting coherence factors. For an isotropic superconductor, neglecting explicit spatial diffusion, the quasiparticle distribution time evolution can be written schematically as

$$\frac{\partial f(E)}{\partial t} = I_{\mathrm{abs}}(E) + I_{\mathrm{em}}(E) + I_{\mathrm{rec}}(E) \quad (2.35)$$

where the three terms describe respectively phonon absorption, phonon emission, and pair breaking or recombination. Expanding these terms to obtain a full energy-resolved form [85][87], we obtain

$$\begin{aligned} \frac{\partial f(E)}{\partial t} = & -\frac{2\pi}{\hbar}\int_0^{\infty} d\Omega\, \alpha^2F(\Omega)\, \rho(E+\Omega)\, K_{\mathrm{ph-e}}(E,\Omega) \\ & -\frac{2\pi}{\hbar}\int_0^{E-|\Delta|} d\Omega\, \alpha^2F(\Omega)\, \rho(E-\Omega)\, K_{\mathrm{e-ph}}(E,\Omega) \\ & -\frac{2\pi}{\hbar}\int_{E+|\Delta|}^{\infty} d\Omega\, \alpha^2F(\Omega)\, \rho(\Omega-E)\, K_{\mathrm{R}}(E,\Omega) \end{aligned} \quad (2.36)$$

Here, $\rho(E)$ is the superconducting quasiparticle density of states normalized to the normal-state electronic density of states, and $\alpha^2F(\Omega)$ is the Eliashberg electron-phonon spectral function. In the present work, the normalized density of states is obtained from the equilibrium real-axis Usadel calculation and is supplied to the kinetic-equation solver as a numerical function. The first two terms in eq. 2.36 describe quasiparticle scattering between states whose energies differ by a phonon energy Ω. They describe transitions between the levels E and $E+\Omega$, and E and $E-\Omega$, respectively. The final term describes the conversion between phonons and pairs of quasiparticles. It describes both quasiparticle recombination with phonon emission, and phonon-induced Cooper-pair breaking. The

factors indicated with K in each of the integral are the collision kernels, which contain the occupation probabilities of the starting and final states, as well as the superconducting coherence factors associated with each process [90].

The explicit form of the kernel for scattering between the energies E and $E+\Omega$ is

$$K_{\mathrm{ph-e}}(E,\Omega) = \left(1-\frac{|\Delta|^2}{E(E+\Omega)}\right)\Big\{f(E)\left[1-f(E+\Omega)\right]n(\Omega) - f(E+\Omega)\left[1-f(E)\right]\left[n(\Omega)+1\right]\Big\} \tag{2.37}$$

The first contribution inside curly brackets describes the absorption of a phonon with energy Ω by a quasiparticle that is originally at energy E. The factor $f(E)$ represents the requirement for the initial quasiparticle state to be occupied, while $1-f(E+\Omega)$ for the final state at higher energy to be available. $n(\Omega)$ factors in the occupation of the absorbed phonon mode. The second contribution in curly brackets describes the reverse process: a quasiparticle at energy $E+\Omega$ emits a phonon with energy Ω and moves to a state with lower energy E. The factor $n(\Omega)+1$ accounts both for stimulated emission, proportional to the existing phonon occupation $n(\Omega)$, and for the spontaneous emission, which remains possible even when the phonon mode is initially unoccupied and is represented by the $+1$.

The corresponding kernel for scattering between energies E and $E-\Omega$ is

$$K_{\mathrm{e-ph}}(E,\Omega) = \left(1-\frac{|\Delta|^2}{E(E-\Omega)}\right)\Big\{f(E)\left[1-f(E-\Omega)\right]\left[n(\Omega)+1\right] - \left[1-f(E)\right]f(E-\Omega)n(\Omega)\Big\} \tag{2.38}$$

The first term in curly brackets describes the relaxation of a quasiparticle from E to $E-\Omega$, accompanied by phonon emission. The second term describes the absorption of a phonon by a quasiparticle, to move from energy $E-\Omega$ to E.

The pair-recombination and pair-breaking kernel is explicitly written as

$$K_{\mathrm{R}}(E,\Omega) = \left(1+\frac{|\Delta|^2}{E(\Omega-E)}\right)\Big\{f(E)f(\Omega-E)\left[n(\Omega)+1\right] - \left[1-f(E)\right]\left[1-f(\Omega-E)\right]n(\Omega)\Big\}. \tag{2.39}$$

The first term in curly brackets describes the recombination of two quasiparticles with energies E and $E-\Omega$ into a Cooper pair, with emission of a phonon with energy Ω. The second term describes the opposite process, in which a phonon breaks a Cooper pair and creates two energetic quasiparticles. Since both generated quasiparticles must have energies at least equal to the minimum excitation energy represented by the superconducting gap, pair breaking requires a sufficiently energetic phonon. In the ideal BCS case, this can be written as $\Omega \geq 2|\Delta|$.

The factors multiplying the occupation probabilities in the kernels are the superconducting coherence factors. The scattering kernels contain coherence factors of the

form

$$1 - \frac{|\Delta|^2}{EE'} \tag{2.40}$$

while pair-breaking and recombination kernels contain coherence factors of the form

$$1 + \frac{|\Delta|^2}{EE'} \tag{2.41}$$

These factors arise from the electron-hole correlations of Bogoliubov quasiparticles [56] and allow to distinguish quasiparticle scattering from processes that change the number of Cooper pairs.

The phonon distribution kinetic equation can instead be written as

$$\begin{aligned}\frac{\partial n(\Omega)}{\partial t} = & -\frac{8\pi}{\hbar}\frac{N(0)}{N}\int_{|\Delta|}^{\infty} dE \int_{|\Delta|}^{\infty} dE'\, \alpha^2(\Omega)\rho(E)\rho(E') \\ & \times \left[K_{\mathrm{S}}(E,E',\Omega)\delta(E+\Omega-E') + K_{\mathrm{B}}(E,E',\Omega)\delta(E+E'-\Omega)\right] \\ & - \frac{n(\Omega)-n_{\mathrm{eq}}(\Omega)}{\tau_{\mathrm{esc}}}\end{aligned} \tag{2.42}$$

In the expression above, $N(0)$ is the single-spin normal-state electronic density of states at the Fermi energy, N is the ion density, τ_{esc} is the characteristic phonon escape time through the substrate [85].

The quasiparticle-scattering kernel in the phonon equation is

$$\begin{aligned}K_{\mathrm{S}}(E,E',\Omega) = & \left(1-\frac{|\Delta|^2}{EE'}\right)\Big\{f(E)\left[1-f(E')\right]n(\Omega) \\ & - f(E')\left[1-f(E)\right]\left[n(\Omega)+1\right]\Big\}.\end{aligned} \tag{2.43}$$

and the delta function $\delta(E+\Omega-E')$ enforces energy conservation for quasiparticle scattering. The first term of the kernel describes absorption of a phonon by a quasiparticle at energy E, resulting in a quasiparticle at energy $E' = E+\Omega$. The second term describes the inverse phonon-emission process.

The pair-breaking kernel is

$$\begin{aligned}K_{\mathrm{B}}(E,E',\Omega) = \frac{1}{2}\left(1+\frac{|\Delta|^2}{EE'}\right)\Big\{ & \left[1-f(E)\right]\left[1-f(E')\right]n(\Omega) \\ & - f(E)f(E')\left[n(\Omega)+1\right]\Big\}\end{aligned} \tag{2.44}$$

The first term in curly brackets describes phonon-induced pair breaking, while the second describes quasiparticle recombination and phonon emission. The factor $1/2$ is required to avoid double counting the two quasiparticle states when integrating independently over E and E'. The delta function $\delta(E+E'-\Omega)$ in Eq.2.42 requires the phonon energy to exactly equal the sum of the two quasiparticle energies.

The final fraction in the phononic kinetic equation represents the coupling to the thermal

bath through phonon exchange between the superconducting film and the substrate. If the excess phonon distribution is positive ($n(\Omega) > n_{\mathrm{eq}}(\Omega)$), excess phonons leave the superconducting film at the characteristic timescale described by τ_{esc} [91]. In reality, the phonon transmission probability depends on the phonon energy, polarization, propagation direction and acoustic mismatch between the film and the substrate. The use of one energy-independent value of τ_{esc} approximates these microscopic details with an effective average escape time.

2.2.2 Electron-phonon spectral functions

The material dependence of the collision rates is introduced through the phonon density of states $F(\Omega)$, the averaged electron-phonon coupling $\alpha^2(\Omega)$, and the Eliashberg spectral function [92][93]

$$\alpha^2 F(\Omega) = \alpha^2(\Omega) F(\Omega) \tag{2.45}$$

The phonon density of states $F(\Omega)$ specifies the number of available lattice modes in a given energy interval, while the factor $\alpha^2(\Omega)$ describes the average strength with which phonons with energy Ω couple to the electronic system. Their product therefore determines the energy-dependent probability density for electron-phonon scattering.

The dimensionless electron-phonon coupling parameter is

$$\lambda_{\mathrm{ep}} = 2 \int_0^\infty \frac{\alpha^2 F(\Omega)}{\Omega} \, d\Omega \tag{2.46}$$

It is possible to obtain material-specific $F(\Omega)$ and $\alpha^2 F(\Omega)$ from experimental spectroscopy or from density-functional perturbation theory. Real phonon spectra generally exhibit multiple acoustic and optical branches and linear dispersions. The precise form of the spectral function can therefore influence both the quasiparticle generation rate and the relaxation dynamics. In the present work, the phonon density of states and electron-phonon spectral function are instead represented by a Debye model.

2.2.3 Debye approximation

The Debye model treats the lattice as a three-dimensional isotropic elastic continuum. The acoustic phonon branches are approximated by a linear dispersion relation up to a sudden cutoff, and no phonon modes are assumed to exist above this cutoff. The cutoff energy is the Debye energy

$$E_{\mathrm{D}} = k_{\mathrm{B}} \Theta_{\mathrm{D}} = \hbar \omega_{\mathrm{D}} \tag{2.47}$$

where Θ_{D} is the Debye temperature and ω_{D} is the Debye angular frequency.

For a phonon density of states normalized per formula unit containing n_{at} atoms, the

Debye phonon density of states is

$$F_{\mathrm{D}}(\Omega) = \begin{cases} \dfrac{9n_{\mathrm{at}}\Omega^2}{E_{\mathrm{D}}^3}, & 0 \le \Omega \le E_{\mathrm{D}} \\ 0, & \Omega > E_{\mathrm{D}}. \end{cases} \tag{2.48}$$

The factor $9n_{\mathrm{at}}/E_{\mathrm{D}}^3$ is fixed by requiring the total number of phonon modes per formula unit to be $3n_{\mathrm{at}}$:

$$\int_0^{E_{\mathrm{D}}} F_{\mathrm{D}}(\Omega)\, d\Omega = 3n_{\mathrm{at}} \tag{2.49}$$

The normalization is chosen so that it reproduces the selected electron–phonon coupling parameter λ_{ep}:

$$2\int_0^{E_{\mathrm{D}}} \frac{\alpha^2 F_{\mathrm{D}}(\Omega)}{\Omega}\, d\Omega = 2\lambda_{\mathrm{ep}} \int_0^{E_{\mathrm{D}}} \frac{\Omega}{E_{\mathrm{D}}^2}\, d\Omega = \lambda_{\mathrm{ep}} \tag{2.50}$$

Combining the expressions of the Debye model for $F(\Omega)$ $\alpha^2 F(\Omega)$ leads to

$$\alpha_{\mathrm{D}}^2(\Omega) = \frac{\alpha^2 F_{\mathrm{D}}(\Omega)}{F_{\mathrm{D}}(\Omega)} = \frac{\lambda_{\mathrm{ep}} E_{\mathrm{D}}}{9n_{\mathrm{at}}}, \quad 0 < \Omega \le E_{\mathrm{D}} \tag{2.51}$$

Thus, the Debye model assumes an energy-independent average electron-phonon coupling over the allowed phonon spectrum. Both $F(\Omega)$ and $\alpha^2 F(\Omega)$ vary quadratically with energy, while their ratio is constant.

The adoption of the Debye model substantially reduces the amount of material-specific information required by the calculation, but it comes with some limitations. It neglects optical phonons, the distinction between longitudinal and transverse modes, non linear acoustic dispersion and any energy-dependence of the electron-phonon coupling element. It also introduces an abrupt spectral cutoff. Consequently, the Debye spectrum should be interpreted as an effective representation of the available phonon modes and their coupling to the electronic system, rather than a complete quantitative description of the phonon spectrum of the investigated bilayers.

2.2.4 BCS interaction and critical temperature

The Debye temperature Θ_{D} fixes also the cutoff energy entering the BCS gap equation. However, that parameter by itself does not guarantee that the model reproduces the experimentally measured critical temperature T_{c}. The weak-coupling BCS interaction is therefore calibrated after fixing the Debye temperature, so that the superconducting gap vanishes at the measured value of T_{c}.

We can indicate as ξ_{BCS} the normal-state single-particle energy measured relative to the Fermi level. The corresponding BCS quasiparticle energy is then

$$E_{\xi_{\mathrm{BCS}}} = \sqrt{\xi_{\mathrm{BCS}}^2 + |\Delta|^2} \tag{2.52}$$

The self-consistency equation is

$$1 = \lambda_{\mathrm{BCS}} \int_0^{E_{\mathrm{D}}} \frac{1 - 2f(E_\xi, T)}{E_\xi}\, d\xi \tag{2.53}$$

And the distribution (2.32) evaluated at thermal equilibrium yields

$$1 - 2f_{\mathrm{eq}}(E_\xi, T) = \tanh\left(\frac{E_\xi}{2k_{\mathrm{B}}T}\right) \tag{2.54}$$

At the critical temperature, the order parameter approaches zero and thus $E_\xi \to \xi$. The condition to enforce the closing at the gap at the measured critical temperature becomes therefore

$$1 = \lambda_{\mathrm{BCS}} \int_0^{E_{\mathrm{D}}} \frac{\tanh(\xi/2k_{\mathrm{B}}T_{\mathrm{c}})}{\xi}\, d\xi \tag{2.55}$$

Inverting the relation above it is possible to obtain λ_{BCS}. Considering the limit of the integrand as the energy ξ_{BCS} approaches zero, and in the weak-coupling limit for which $E_{\mathrm{D}} \gg k_{\mathrm{B}}T_{\mathrm{c}}$, we finally obtain

$$\lambda_{\mathrm{BCS}} \simeq \left[\ln\left(\frac{1.134\,\Theta_{\mathrm{D}}}{T_{\mathrm{c}}}\right)\right]^{-1} \tag{2.56}$$

In the calculation, however, the finite-cutoff integral is evaluated numerically rather than relying on this asymptotic approximation. This procedure ensures that the gap calculated with the weak-coupling self-consistency equation vanishes at the experimentally determined T_{c}, allowing to model more closely the properties of our bilayers.

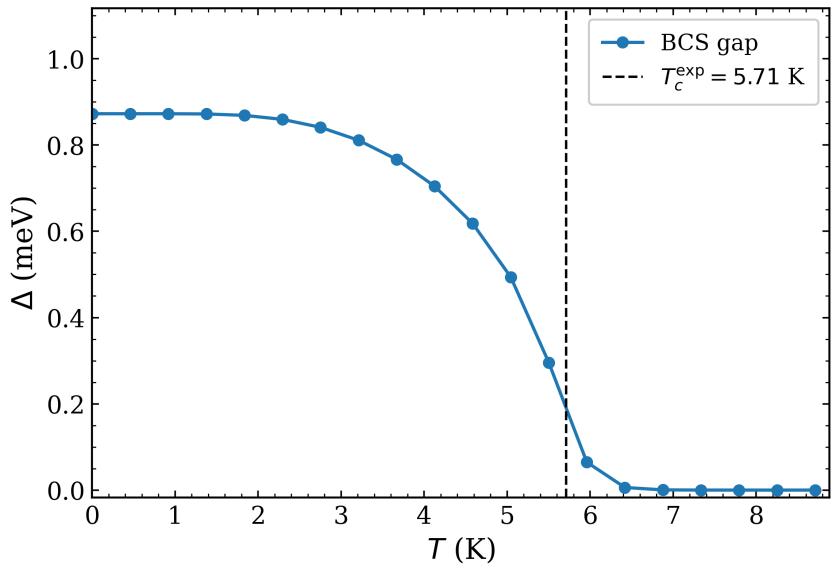


Figure 2.7: BCS modeling of the temperature dependence of the superconducting gap, computed for the 2 nm NbN + 3 nm MoSi sample.

2.2.5 Photon absorption and perturbation time evolution

When a photon is absorbed by the superconducting film, it creates a local perturbation that suppresses the superconducting state. An optical photon at a wavelength λ_{ph} carries an energy $E_{\mathrm{ph}} = \frac{hc}{\lambda_{\mathrm{ph}}}$. For visible and near-infrared photons, this energy is usually much larger than the superconducting gap and the characteristic acoustic phonon energy scale. Following the absorption, a high-energy electronic excitation is formed. Electron-electron scattering then leads to secondary excitations, and finally the energy is transferred to the lattice through phonon emission [94, 95]. The lifetime of the initial high-energy excitation is short compared to the timescale over which the superconducting order parameter changes [96]

$$\tau_{\Delta} = \frac{\hbar}{|\Delta|} \tag{2.57}$$

A convenient approximation is to begin the kinetic-equation calculation after the initial perturbation has generated the local nonequilibrium phonon population. This is known as phonon-bubble initial condition [94, 96]. At the initial time, the quasiparticle distribution is supposed to remain in equilibrium

$$f(E, 0) = f_{\mathrm{eq}}(E, T_{\mathrm{bath}}) \tag{2.58}$$

while the phonon distribution is discontinuously initialized as

$$n(\Omega, 0) = n_{\mathrm{eq}}(\Omega, T_{\mathrm{bath}}) + \beta\, \alpha^2(\Omega) \tag{2.59}$$

where the factor β is computed such that the excess energy in the phonon system equals the deposited photon energy. Considering the energy to be deposited in a volume V_{init}, this condition can be expressed as

$$V_{\mathrm{init}} \int_0^{\infty} d\Omega\, \Omega\, N F(\Omega)\, [n(\Omega, 0) - n_{\mathrm{eq}}(\Omega)] = E_{\mathrm{ph}} \tag{2.60}$$

where E_{ph} is the photon energy that is deposited in the superconducting film. The normalization coefficient β is thus

$$\beta = \frac{E_{\mathrm{ph}}}{V_{\mathrm{init}} N \int_0^{\infty} d\Omega\, \Omega \alpha^2 F(\Omega)} \tag{2.61}$$

Substituting the Debye spectral function $\alpha^2 F_{\mathrm{D}}(\Omega)$ (Eq.2.48-2.51 and considering the implied cutoff at E_{D}, the phonon-bubble normalization under the Debye model becomes

$$\beta = \frac{4 E_{\mathrm{ph}}}{V_{\mathrm{init}} N \lambda_{\mathrm{ep}} E_{\mathrm{D}}^2} \tag{2.62}$$

In the chosen Debye model, $\alpha^2(\Omega)$ is constant below the cutoff, meaning that the excess phonon occupation $\delta n(\Omega, 0)$ is constant over the allowed phonon energy range. However,

this does not mean that the initial excess energy is distributed uniformly. In fact, the energy stored in an interval $d\Omega$ is proportional to $\Omega F(\Omega)\delta n(\Omega, 0)$, which scales as Ω^3. Hence, the high-energy section of the Debye phonon spectrum carries most of the initial excess energy. The initial perturbation volume is often chosen as

$$V_{\text{init}} = \pi \xi^2 d \tag{2.63}$$

where d is the film thickness and $\xi = \sqrt{\frac{\hbar D}{|\Delta|}}$ is the superconducting dirty-limit coherence length[90, 97]. A material with lower diffusion coefficient therefore will have a smaller excitation volume for the same deposited energy, leading to a larger quasiparticle population and stronger local suppression of superconductivity.

Once the phonon population has been initialized, the kinetic equations describe how these vibrations scatter quasiparticles and break Cooper pairs. The generated quasiparticles emit and reabsorb phonons, redistribute their energy and eventually recombine. The phonons emitted during quasiparticle relaxation and recombination can in turn break additional Cooper pairs, before escaping into the substrate.

The nonequilibrium quasiparticle distribution affects the superconducting order parameter through the self-consistency equation [1], which can be written in a general spectral representation as

$$|\Delta(t)| = \lambda_{\text{ep}} \int_{|\Delta|}^{\infty} dE\, R(E, \Delta)\, [1 - 2f(E, t)] \tag{2.64}$$

where $R(E, \Delta)$ is the anomalous spectral function, that can be obtained from the Usadel equation. The factor $1 - 2f(E, t)$ expresses the reduction of superconducting pairing caused by quasiparticle occupation. If the occupation $f(E, t)$ increases, the contribution of the corresponding energy interval to the self-consistency integral is reduced, and the superconducting order parameter is suppressed.

The quasiparticle-induced suppression can alternatively be measured by the parameter

$$\varepsilon(t) = 2 \int_{|\Delta|}^{\infty} dE\, \frac{R(E, \Delta)}{|\Delta|} \delta f(E, t) \tag{2.65}$$

At equilibrium, $\delta f(E, t) = 0$, and therefore $\varepsilon = 0$. For weak perturbations, $\varepsilon(t)$ provides a linearized measure of the suppression caused by the excess quasiparticle population [90].

In the numerical implementation used in this work, the transient gap is calculated at each time step using the BCS self-consistency equation 2.53. The nonequilibrium distribution obtained from the kinetic equations is therefore inserted directly into the gap equation.

The quasiparticle density of states $\rho(E)$ entering the kinetic collision integrals is obtained from the real-axis Usadel calculation, simulating the operating conditions of our devices at a temperature of 1.3 K and a bias current $I_{\text{b}} \sim 75\%\ I_{\text{dep}}$. This allows the current-broadened spectrum of the proximitized structure to be included in the modeling of scattering, pair breaking, and recombination.

The combination of an Usadel-computed quasiparticle density of states in the kinetic equations and a BCS equation for the transient gap constitutes a hybrid approximation. The equilibrium superconducting spectrum includes the proximity effect and the current-induced pair breaking modeled by the Usadel equation. At the same time, the transient self-consistency condition is represented by an effective isotropic BCS model. A fully self-consistent nonequilibrium treatment would require updating the Usadel spectral functions together with the distribution at each time step, but such a computation would be substantially more demanding.

Summarizing the operating procedure: the initial quasiparticle and phonon distributions are first set to their equilibrium values at the bath temperature. The phonon distribution is then replaced by the phonon-bubble distribution. At each time step, the collision integrals are evaluated for the current distributions and the latter are updated accordingly. After that, the nonequilibrium BCS self-consistency equation is solved again to obtain the superconducting gap at the next time step. The calculation therefore follows the sequence

$$f(t_i),\, n(t_i),\, \Delta(t_i) \longrightarrow \frac{\partial f}{\partial t},\, \frac{\partial n}{\partial t} \longrightarrow f(t_{i+1}),\, n(t_{i+1}) \longrightarrow \Delta(t_{i+1}) \tag{2.66}$$

The time evolution determined how the initially deposited phonon energy is converted into quasiparticle excitations and how the superconducting order parameter is suppressed.

2.2.6 Extraction of the characteristic time constant

The kinetic equation modeling returns us the time-dependent gap $|\Delta(t)|$, from which we can determine how much and how fast the superconducting state is suppressed. To obtain a measure of the characteristic time of the dynamics, the time-dependent gap is fitted with a single-exponential function

$$\Delta_{\mathrm{fit}}(t) = a \exp\left(-\frac{t}{b}\right) + c \tag{2.67}$$

For the initial energy down-conversion stage considered in the simulation, the superconducting gap decreases from its initial equilibrium value towards a suppressed value. In this case, a is positive and related to the magnitude of the gap suppression, c represents the extrapolated suppressed asymptotic gap, and $b = \tau_{\mathrm{DC}}$ (down-conversion characteristic time) describes how quickly the gap approaches that value.

The resulting time constant is an effective time associated with the quasiparticle generation and energy redistribution dynamics, and reflects the conversion of the initial phonon perturbation into quasiparticles, leading to the corresponding suppression of the superconducting gap. The kinetic equation response is not analytically required to be exactly single-exponential. Several processes can occur simultaneously, including phonon absorption, quasiparticle scattering and recombination, and phonon escape [85]. The fitted value τ_{DC}, however, provides a simple and immediate way to compare the response dynamics of the different bilayers.

The parameter τ_{DC} is distinct from the electrical response time of an SNSPD. The kinetic equation time describes the microscopic evolution of the quasiparticle-phonon system and the superconducting gap. However, the electrical response time depends also on the device shape and current distribution, its kinetic inductance, Joule heating and electrothermal feedback.

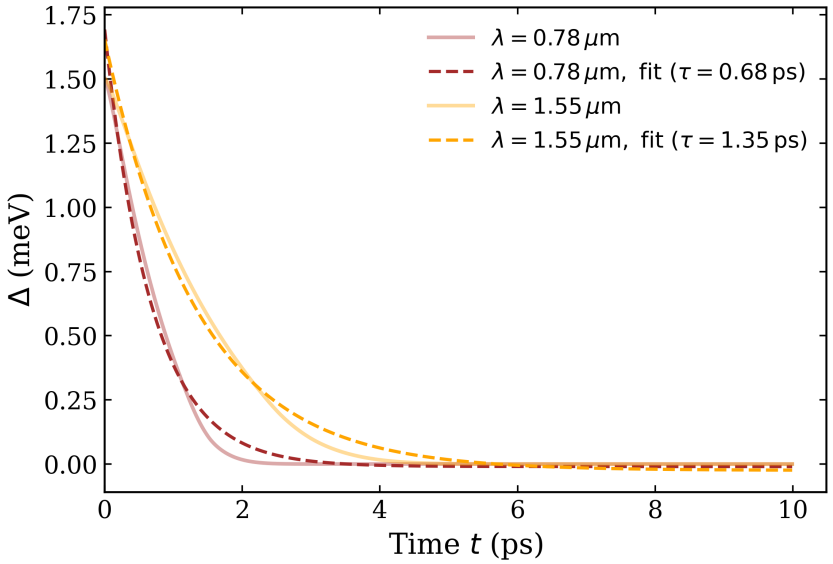


Figure 2.8: Calculated and fitted time evolution of the superconducting gap Δ of the 4 nm NbN + 1 nm MoSi sample, for the 780 nm and 1550 nm wavelengths.

2.2.7 Energy-equivalent effective temperature

The quasiparticle and phonon distributions generated by photon absorption are generally nonthermal, particularly during the early stages of the relaxation cascade. This means that the spectrum occupation has a different shape than the one that would result from simply increasing the temperature in the equilibrium distributions (eq. 2.32,2.33). Nevertheless, it is useful to define an effective equilibrium temperature by requiring that an equilibrium quasiparticle (or phonon) distribution contains the same energy as the calculated nonequilibrium distribution. As the excited systems have not reached internal thermal equilibrium, this effective temperature is only a scalar representation of the energy stored in the nonthermal distribution.

The energy stored in the nonequilibrium quasiparticle population, in a volume V, is

$$E_{\mathrm{qp}} = V \int_0^\infty dE\ N(E)\ f(E)\ E \tag{2.68}$$

where $f(E)$ is the non-equilibrium distribution computed by the kinetic equation. The quasiparticle density of states $N(E)$ can be rewritten as

$$N(E) = 4N(0)\rho(E) \tag{2.69}$$

where $N(0)$ is the single-spin normal-state electronic density of states at the Fermi level, $\rho(E)$ is the normalized quasiparticle density of states obtained from the real-axis Usadel calculation, and the factor 4 accounts for the spin and electron-hole branches of the quasiparticle spectrum.
The equilibrium quasiparticle energy at an unknown temperature T_{eff} is

$$E_{\text{qp}}^{\text{eq}}(T_{\text{eff}}) = 4N(0)\ V \int_0^\infty dE\ \rho(E)\ f_{\text{eq}}(E, T_{\text{eff}})\ E \tag{2.70}$$

following the same definition for the quasiparticle density of states, and with

$$f_{\text{eq}}(E, T_{\text{eff}}) = \frac{1}{\exp(E/k_{\text{B}}T_{\text{eff}}) + 1} \tag{2.71}$$

The energy-equivalent effective temperature is then defined by the condition

$$E_{\text{qp}} = E_{\text{qp}}^{\text{eq}}(T_{\text{eff}}) \tag{2.72}$$

Substituting the expressions 2.68 and 2.70 into 2.72, we can get the final relation

$$\int_0^\infty dE\ \rho(E)\ E\ [f_{\text{eq}}(E, T_{\text{eff}}) - f(E)] = 0 \tag{2.73}$$

which is a one-dimensional nonlinear equation for T_{eff}. The corresponding effective temperature increase can be defined as

$$\chi = T_{\text{eff}}(t) - T_{\text{bath}} \tag{2.74}$$

The effective temperature can be calculated at every time step, producing the complete function $T_{\text{eff}}(t)$. Alternatively, one can simply evaluate T_{eff} at a specified point in the evolution, such as the time of maximum quasiparticle energy or the time of minimum superconducting gap.

This treatment uses the same density of states $\rho(E)$ for the nonequilibrium and equilibrium energy integrals, thus relying on the fixed spectrum supplied to the kinetic model. If, following the photon absorption, the gap and density of states change substantially, a self-consistent construction would allow $\rho(E)$ to vary with the suppression dynamics and account for the change in condensate energy.

An analogous treatment can be done for the effective temperature relative to the phonon population T_{ph}. The energy stored in the phonon system can be written as

$$E_{\text{ph}} = V \int_0^\infty d\Omega\ N\ n(\Omega)\ \Omega \tag{2.75}$$

where Ω is the phonon energy, N is the ion density, and $n(\Omega)$ is the phonon distribution computed by the kinetic equations. The respective equilibrium distribution to be modeled at the effective phonon temperature T_{ph} is the Bose-Einstein distribution (Eq. 2.33).

2.2.8 Approximations and applications

While the energy-resolved kinetic framework provides a microscopic description of the photon-induced response, its predictions rest on a number of simplifying assumptions, which are worth stating explicitly.

First, the standard formulation assumes an isotropic conventional superconductor and the functions $f(E,t)$ and $n(\Omega,t)$ depend only on energy and time. The presence of multiple bands or of a momentum-dependent electron-phonon coupling would require additional considerations. Moreover, the equations are solved locally without explicit spatial diffusion. The evolution of the superconducting state is described within an assumed excitation volume, but the hotspot expansion across a device is not calculated. The diffusion coefficient enters only through the coherence length to set the initial volume, but the subsequent diffusion of quasiparticles is not included in the model. The phonon escape to the substrate is represented by a single averaged time τ_{esc}, although the true escape probability can depends on phonon energy and direction and can have a larger variance [91].

The phonon spectrum is represented by a Debye model, which neglects the detailed phonon structure and the energy dependence of the electron-phonon coupling coefficient. The Debye model is therefore expected to capture general trends, rather than detailed quantitative features.

The weak-coupling formulation neglects the frequency dependence of the superconducting order parameter, which greatly reduces the computational cost [98, 99]. In particular, the equilibrium density of states obtained from the Usadel equations is supplied as a fixed input to the collision integrals, and the transient gap is then recomputed at each time step from the isotropic BCS self-consistency equation, using the instantaneous quasiparticle distribution. The pairing interaction entering this self-consistency equation is calibrated independently, so as to reproduce the experimentally measured T_{c}. The resulting scheme is therefore a hybrid one, in which the proximitized spectrum and the nonequilibrium dynamics are treated at different levels, and the density of states is not updated as the gap evolves. A fully self-consistent treatment would instead require the density of states, the quasiparticle and phonon distributions and the order parameter to be updated simultaneously.

Finally, the kinetic equations only describe the deterministic average response. Probabilistic events such as Fano fluctuations [100, 17], spatial material inhomogeneity, optical absorption probability, must be added to correctly predict the full internal detection efficiency, timing jitter and dark count rates.

For the present work, the kinetic equations can be applied to the effective superconducting material produced by the proximity effect in a bilayer. The equilibrium Usadel calculation provides the required superconducting spectral information, including the current- and temperature-dependent density of states, the effective gap, the relation between superfluid momentum and bias current and the pairing potential. These quantities replace the ideal bulk BCS spectrum in the kinetic model, together with experimental-

derived quantities such as the critical temperature and the diffusion coefficient. The resulting calculation predicts how the proximitized bilayer responds microscopically to photon absorption and repeating it for different compositions of the stack allows us to further explore the dynamics of the proximity effect in tuning the detector properties. The Usadel model determines the superconducting spectrum available before absorption, and the kinetic equations determine how that spectrum is populated and suppressed after energy is deposited.

Photon-induced quasiparticles locally suppress the superconducting order parameter and, in a current-biased nanowire, cause the current to be redistributed around the suppressed region. This perturbation can reduce the energy barrier for vortex crossing or similar phase-slip events that produce dissipation and can start the development of a normal domain across the nanowire. To connect this microscopic response to an SNSPD detection event, the calculated suppression can then be introduced into a spatial model and use Time-Dependent Ginzburg-Landau (TDGL) model to determine whether the perturbation lowers sufficiently the energy barrier to produce a resistive transition [101][90]. A complete description of the voltage pulse would also require an electrothermal model and an external circuit model, to take into account Joule heating, heat diffusion, kinetic inductance and load impedance. The kinetic equation calculation should therefore be viewed as the microscopic starting point of the detector response.

3 Material choice and design

As discussed in the introduction, the choice of superconducting material strongly affects the performance of an SNSPD through parameters such as the critical temperature, superconducting gap, switching current, kinetic inductance, and photon sensitivity. Material selection must therefore consider the trade-offs between these properties, while also accounting for the compatibility, reproducibility and fabrication requirements of the multilayer process. In the present work, the choice of NbN and MoSi was guided by both their complementary superconducting properties and the feasibility of fabricating the two materials within a common process flow [18].

3.1 NbN and MoSi properties

Niobium nitride (NbN) and molybdenum silicide (MoSi) are established as mature SNSPD materials, whose single-photon detection operation has widely been demonstrated [19, 102]. The two materials occupy different regions in the SNSPD parameter space and therefore provide a promising combination for bilayer engineering.

NbN is characterized by a relatively high critical temperature, large superconducting gap, high critical current, and fast electrical response [74]. These properties make NbN attractive for operation at relatively high temperatures, relaxing the constraints on the cooling system requirements [103]. The large switching currents also provide higher signal amplitude and lower timing jitter. However, its larger superconducting gap and condensation energy can make it difficult to reach saturated internal detection, especially at longer telecommunication wavelengths such as 1550 nm. From a fabrication perspective, NbN ultrathin films can be polycrystalline and spatially nonuniform, so greater care is required in the growth of these layers [104].

MoSi, in contrast, has a lower superconducting gap, making it easier for low-energy photons to perturb the superconducting state and enabling high internal detection efficiency even at longer wavelengths [105]. This advantage comes at the cost of lower critical temperature and, consequently, lower operating temperature. MoSi is an amorphous superconducting material and its deposition can generally yield uniform ultrathin layers [106].

Reliable and similar fabrication processes exist for these two materials. In particular, it is possible to deposit thin films with good uniformity, and both of them can be etched

with a fluorine-based plasma etching chemistry (see sec. 4.3). This means we can use one single lithographic process to pattern the entire stack, removing alignment issues and greatly simplifying the process.

3.2 Layout design

The performance of a superconducting detector is influenced not only by the constituent material, but also by the geometric parameters such as the thickness, width, and length of the nanowire. For this thesis, the thickness of all the samples was fixed to 5 nm, while the other dimensions were varied systematically.

Two classes of devices were fabricated on each sample: straight nanowires and meandered nanowires. Straight nanowires provide a relatively simple geometry, allowing to characterize the intrinsic superconducting and electrical properties of the bilayer, while minimizing geometric effects. Meandered nanowires, by contrast, provide a larger active area within a compact footprint, and they are more representative of practical SNSPD geometries, as this allows efficient optical coupling to a fiber [18]. However, their increased length and more complex geometry make them more prone to spatial nonuniformities and constrictions, making it more difficult to isolate the material properties from the fabrication-dependent effects [107].

The switching current of a nanowire is determined by its weakest section, meaning that a single constriction in a long nanowire can heavily affect the maximum bias current of the whole device. A useful parameter for quantifying this effect is the constriction factor, defined as

$$C = \frac{I_{\mathrm{sw}}}{I_{\mathrm{dep}}} \tag{3.1}$$

where I_{sw} is the experimentally measured switching current and I_{dep} is the theoretical depairing current of an ideal homogeneous nanowire. A value of $C < 1$ indicates that the switching current of our device is limited by imperfections such as constrictions, edge roughness, or similar sources of local current crowding.

In the context of this thesis, both geometries are useful as the goal is not only to demonstrate material properties of the NbN/MoSi bilayers, but also to understand how these physical parameters translate into SNSPD performances.

For each device type, several dimensions were fabricated. The length of the nanowires (straight or meandered) was varied from 1 µm to 1.34 mm, while the width ranged from 75 nm to 400 nm. Narrower wires generally provide higher sensitivity to photons, as a given energy deposited into the device is more likely to perturb that section enough to make it revert to the resistive state [108]. At the same time, they require a more delicate fabrication process and are more prone to constrictions and structural defects. Larger nanowires, on the other hand, take advantage of a more reliable fabrication, but it is harder for them to reach high internal detection efficiency. Longer nanowires provide a larger active area for photon absorption, but are more prone to constrictions and defects.

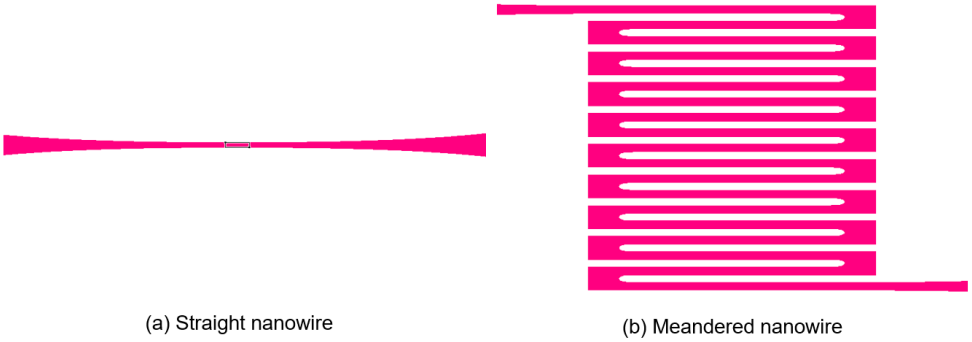


Figure 3.1: The two shapes of nanowires fabricated. (a) Straight nanowire, with a thin section of the desired width in the center and larger connectors at the sides. (b) Meandered nanowire with numerous connected sections at the nominal width, leading to a large and compact active area.

Table 3.1 reports the 16 devices, with their type (ME for meanders, NW for simple nanowires), their width and their length (for simple nanowires) or active area (for meanders) respectively. The organization inside of the table reflects the spatial distribution in the final layout design, stored in the .gds file later used in the exposure for the lithographic step. The devices are fabricated on a standard 1 cm × 1 cm sapphire (Al_2O_3) substrate.

Table 3.1: Devices shapes, dimensions and arrangement

ME, 75nm, 5×5μm	ME, 100nm, 5×5μm	ME, 100nm, 15×15μm	ME, 150nm, 10×10μm
ME, 150nm, 20×20μm	ME, 200nm, 10×10μm	ME, 200nm, 20×20μm	ME, 400nm, 15×15μm
NW, 100nm, 1μm	NW, 100nm, 10μm	NW, 100nm, 100μm	NW, 150nm, 10μm
NW, 200nm, 1μm	NW, 200nm, 10μm	NW, 200nm, 100μm	NW, 400nm, 100μm

The pads are designed as $500 \times 500\mu m^2$ squares, to facilitate the connection to the macroscopic electronic measurement setup.

The .gds file was generated parametrically using qnngds [109], a layout-design toolbox built on top of phidl [110] with custom shapes and functions, developed within the QNN group [111].

3.2.1 Positive resist

Resists are particular polymer solutions that can modify their physical properties when exposed to some kind of radiation (either light or electrons). According to the way they react to the exposure, they can be classified as positive- or negative-tone resist. More details can be found in section 4.2. For our fabrication process we used ZEP520, a positive resist, meaning that only the exposed regions will be removed and etched through. Starting from the device designs shown in figure 3.1, we must invert the area to expose an outline of the shape we want to preserve.

To ensure resolution of the devices, the width of this outline was set to be the same as the dimension of the feature it encloses, or slightly higher. The use of positive resist also required inverting the layout for the bonding pads. A 100 µm-wide outline is therefore

defined around each pad to facilitate locating the devices on the sample and wirebonding them to the PCB (sec. 4.5).

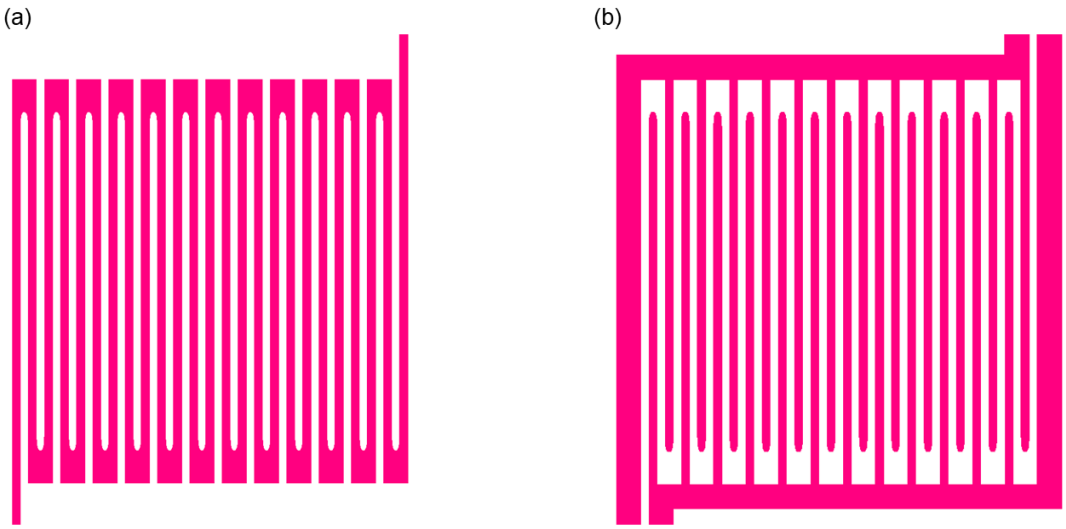


Figure 3.2: Layout of a meandered nanowire for the two possible polarities of the resist. (a) Layout for negative resist: the nanowire would be protected and the surrounding region would be etched. (b) Layout for positive resist: only the highlighted outline is etched, the nanowire and the surrounding film survive.

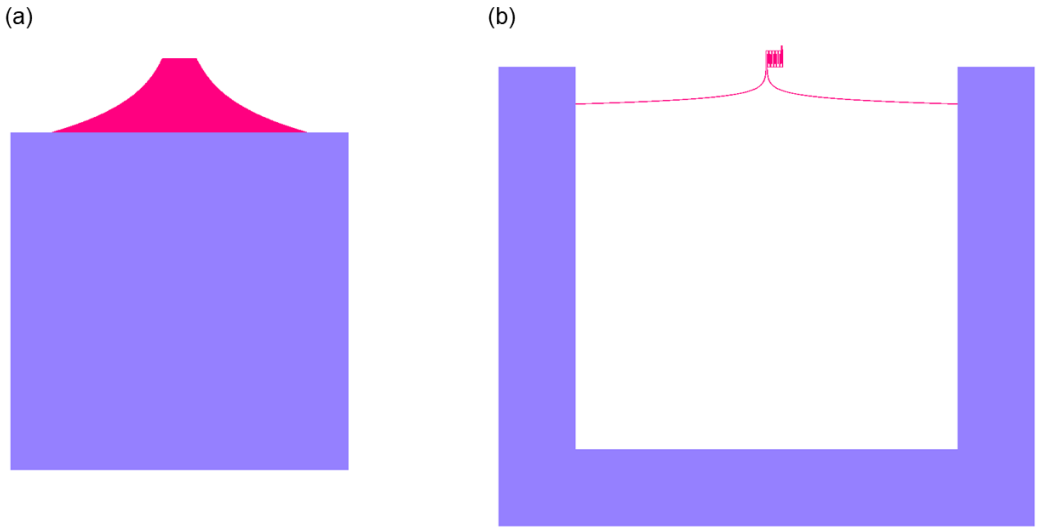


Figure 3.3: Layout of the bonding pads for the two possible polarities of the resist. (a) Layout for negative resist: the pad is the purple square, that would be protected from etching by the negative resist. The magenta structure is part of the taper that connects the large pad to the nanowire. (b) Layout for positive resist: the pad is the white square enclosed by the purple U and the magenta taper outline. This region is protected, while the drawn outlines are etched.

3.2.2 Tapers

To connect the nm-size devices to the bonding pads, as well as the booster meanders (see sec. 3.2.3), intermediate structures called tapers were employed. These shapes allow us to vary the width of the wire in a gradual manner. If the current path was to change abruptly, either due to sharp corners or sudden changes in wire width, current streamlines would be forced to bend or compress, causing the local current density to increase above the average current density in the rest of the structure [112]. This phenomenon is called current crowding and is particularly detrimental for superconducting detectors because it could limit the bias current the device could sustain, causing it to switch prematurely.

The taper hyperbolic shape, as well as the shape of the turns in the meanders, is derived to be the optimal geometry to prevent current crowding.

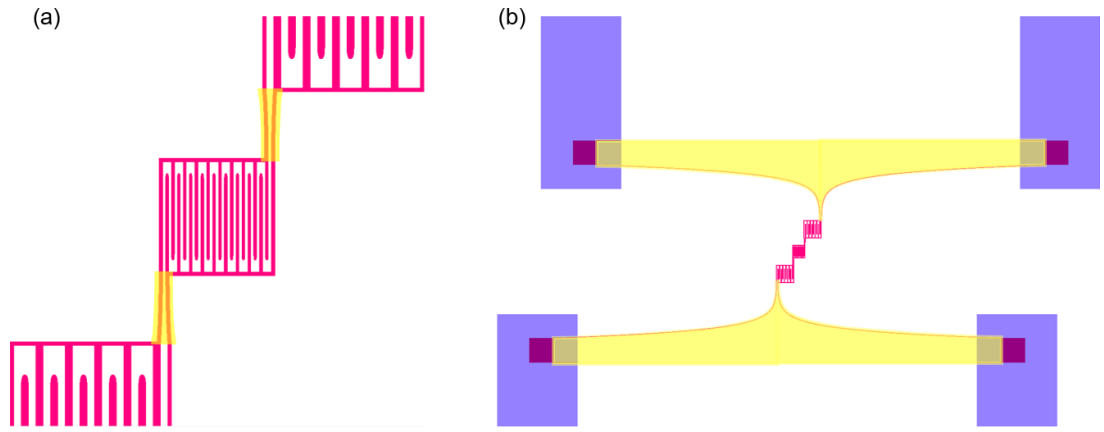


Figure 3.4: Close-up of the .gds, highlighting the tapers between the device and the booster meanders (a), and between the booster meanders and the pads (b).

3.2.3 Booster meanders

Following a resistive transition, the bias current flowing through the nanowire is diverted into the readout electronics. When the detectors relaxes back to the superconducting state, I_b returns to the detector branch with a time constant that depends on its kinetic inductance L_k [113]. We want its value to be large enough that the device has sufficient time to reach a stable configuration. If the current returns too rapidly while the superconducting state is still recovering, the nanowire can undergo a second transition and latch into the resistive state [114, 115].

The nanowires can be seen as thin rectangles of length l and width w, that are consequently composed of a number of squares l/w. The kinetic inductance, which contributes to determining the detector reset time, increases with the total number of squares in the nanowire [116]. Since the dimensions of the active detector structures were fixed by the experimental design, additional kinetic inductance was introduced, where necessary, using wide auxiliary meanders placed between the detector and the bonding pads. These auxiliary meanders were designed with a width of 1 µm, substantially larger than that of the active nanowires, to reduce their sensitivity to photons and therefore increase the kinetic inductance without significantly extending the photon-sensitive area. The 1 µm width was chosen as a conservative fabrication dimension, sufficiently large to ensure robust patterning, while avoiding unnecessarily large features that would increase the required lithography exposure time.

To achieve dynamics of the order of 10 GHz, we designed our SNSPDs to be composed of at least 10^3 squares, assuming a kinetic inductance of 5 pH/square. This design choice ensures we approach the limit of the detection rate allowed by our experimental setup, while also operating at a sufficiently slow rate to prevent latching. Some of our meanders, due to the reduced width and the large active area, already crossed this limit and did not need to have their kinetic inductance increased. We only added booster meanders to the devices whose square count was too low.

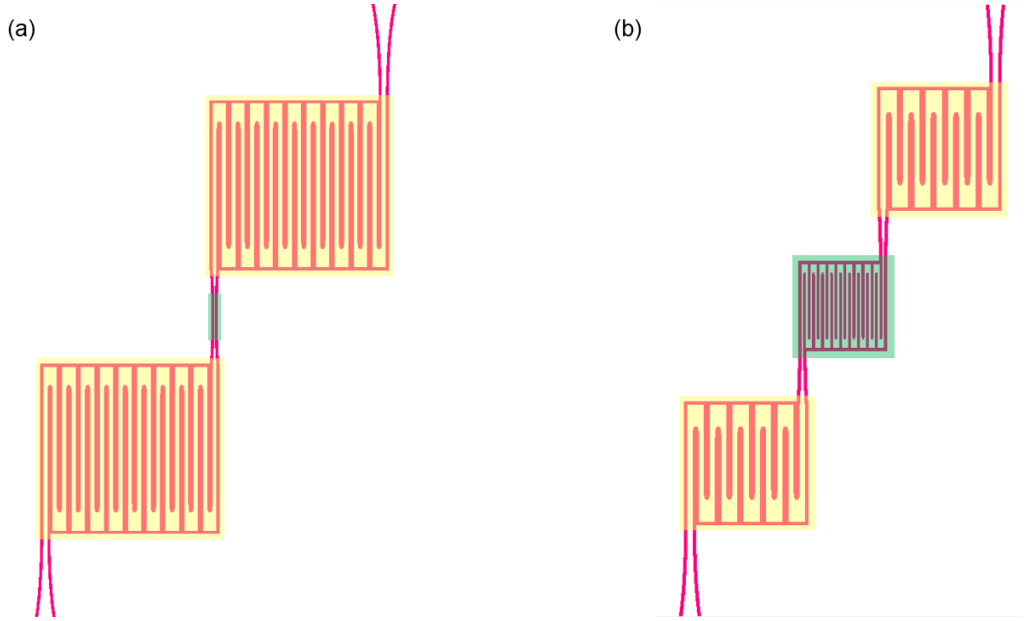


Figure 3.5: Close-up of devices (highlighted in green) with added booster meanders (highlighted in yellow), for a straight nanowire (a) and meander nanowire (b)

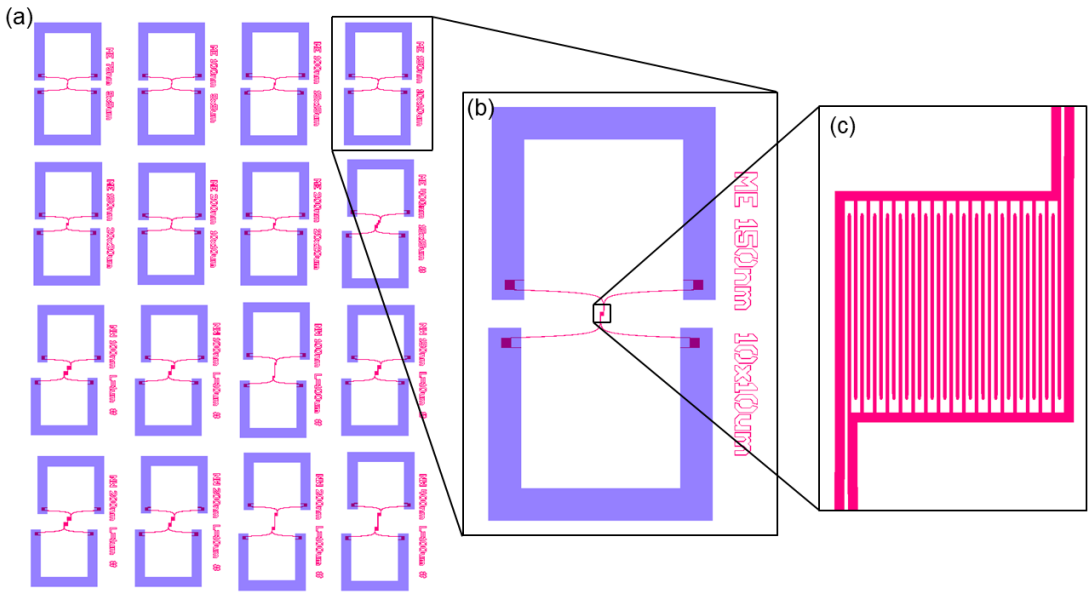


Figure 3.6: Overview of the complete chip layout. The white background is the superconducting film that will remain onto the sample. The magenta structures are the outlines of the nanowires. The purple U-shapes are the outline of the pads, on a dedicated layer that will be exposed with a higher beam current. (a) Image of the whole .gds file with the various devices. (b) Zoom-in on one selected device, including the active area and the larger pads. (c) Detail of the active area of that meandered nanowire.

4 Device fabrication

In the following sections, we explain in detail the complete process for detector fabrication. Starting from a sapphire substrate, the thin superconducting films are deposited by sputtering. Electron-beam lithography is used to pattern the nanowire shapes on the bilayer, that is then etched to reveal the nanowires. Finally, the chip is attached using an adhesive to a printed circuit board (PCB) and the devices are wire-bonded to sub miniature push-on (SMP) connectors to be tested in the cryostat.

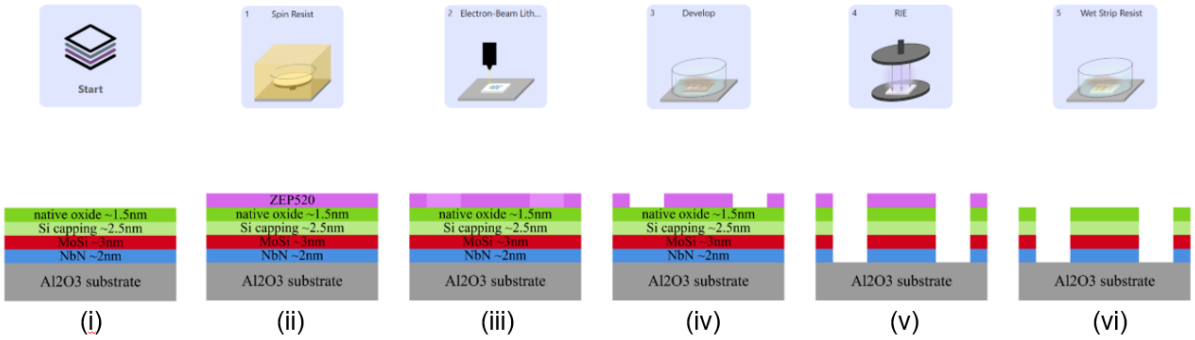


Figure 4.1: Overview of the complete fabrication workflow. (i) We start from the substrate on which the superconducting films and the silicon capping layer have been deposited. (ii) Resist is spun and baked on top of the sample. (iii) Electron-beam lithography transfers the pattern into the resist. (iv) The development step allows to selectively create openings in the resist, corresponding to the design. (v) Reactive ion etching allows to replicate the pattern in the stack by removing the underlying layers. (vi) A final strip process removes the unexposed resist from the top of the sample.

4.1 Thin film sputtering

Sputtering is a physical vapor deposition (PVD) technique that allows for the deposition of thin films by ejecting the desired material from a solid target and depositing it onto a substrate. The process takes place in a vacuum chamber that is first pumped under vacuum to reduce contamination from residual gases and particles. Then a gas, typically argon, is introduced into the chamber and ionized by a high voltage to form a plasma. The positively charged Ar ions are accelerated towards the cathode (negatively biased) and strike the target, transferring momentum to the atoms and ejecting them from the surface. These sputtered atoms then travel through the controlled chamber and condense on the sample, forming a thin film [117]. A particular type of deposition technique is magnetron

sputtering, in which magnets behind the target help to confine electrons closer to the target surface, increasing the plasma density and improving the deposition efficiency.

The final film properties depend on process parameters such as sputtering power, pressure, gas flow, substrate rotation, target, and deposition times.
The stacks in this work were deposited using the sputtering system AJA ATC Orion 8 [118]. The presence of multiple targets allows us to deposit different layers on top of each other without breaking vacuum, improving the interface quality. This is particular important to be able to efficiently exploit the proximity effect that arises between the two superconducting layers.

MoSi films were deposited by sputtering in argon plasma. In this process, argon acts as an inert gas whose role is to sustain the plasma and sputter material from the target. The alloy was obtained by sputtering at the same time on the two targets (molybdenum and silicon solid targets). The stoichiometry is dependent on the relative sputtering rates of the two targets, that are functions of the materials themselves and the applied powers. The relative composition is expected to be $Mo_{0.83}Si_{0.17}$ [119].

NbN films were deposited by reactive sputtering from a Nb target, heating the substrate to 800 °C. For this process, two gases are introduced into the chamber: Ar is used, as normally, to generate the plasma and sputter Nb atoms from the solid target; nitrogen (N_2) is introduced as reactive gas, to combine with the sputtered Nb atoms and form niobium nitride that deposits on the surface of the substrate.[1]

The elevated deposition temperature is important to promote epitaxial growth of the layer. By providing such energy, the atoms arriving at the surface possess increased mobility, allowing them to diffuse and rearrange across the surface and occupy energetically favorable lattice sites. The result is a more ordered and structured polycrystalline film, which results in higher critical temperature and switching current.

This same reason is also behind the choice of sapphire (Al_2O_3) as substrate, instead of the typical silicon (Si) or silicon oxide (SiO_2). The former is a crystalline substrate, while native, thermally grown or deposited SiO_2 is amorphous. Epitaxy requires the deposited layer to align with the crystal structure of the underlying substrate, and that is why sapphire is a good growth template for nitrides.

It is also worth mentioning, however, that sapphire has a low acoustic mismatch to NbN, facilitating the escape of phonons from the superconducting film into the substrate. Phonon trapping, on the contrary, refers to the confinement of these phonons within the superconducting layer. This phenomenon is desirable as it can cause an augmented generation of quasiparticles and, consequently, suppression of the superconducting state. If the phonons are confined in the active layer it is thus more likely that the photon perturbation leads to a detection event. This translates in a higher detection efficiency.

Because of the more delicate requirements for high-quality growth, in the bilayer structures produced in this work, NbN is always grown first, in contact with the crystalline

[1]This is still considered a physical deposition process, because the Nb source is a solid sputtering target, and not a gas-phase precursor

substrate. Amorphous MoSi is then deposited on top. The stack is finally covered with a thin (~3 nm Si capping layer, to protect the superconducting materials from oxidizing and degrading when exposed to the atmosphere.

To precisely isolate the effect of the materials composition, all the devices were built on a 5-nm thick bilayer. Different samples were deposited with various NbN and MoSi composition, following a 1-nm variation: [0nm NbN + 5nm MoSi], [1nm NbN + 4nm MoSi], [2nm NbN + 3nm MoSi], [3nm NbN + 2nm MoSi], [4nm NbN + 1nm MoSi] and [5nm NbN + 0nm MoSi]. All of these are also covered with the Si capping layer.

4.2 Electron-beam lithography

Electron-beam lithography (EBL) is a direct-write nanofabrication technique used to define patterns with nanoscale resolution. Unlike optical lithography, which uses photomasks to transfer the pattern using light, EBL uses a focused beam of electrons that is scanned across the sample surface according to a computer-generated layout. Electrons can be accelerated to high energies, achieving a smaller wavelength than light typically used in photolithographic processes and thus improving spatial resolution of the patterned features. The sample is first coated with an electron-sensitive resist, whose chemical properties are locally modified by electron exposure. The resulting resist pattern can then be used as a mask for subsequent fabrication steps, namely etching in our case.

During exposure, several parameters have to be optimized, such as beam current, step size and dose.
The beam current determines how many electrons reach the sample per unit of time. Lower currents are generally used when patterning finer features, as they provide a smaller and more stable beam spot, improving resolution. Higher currents are used for larger features where resolution and layout fidelity is less critical, allowing to save exposure time.
Step size determines the spacing between adjacent beam positions during patterning. Smaller step size improves resolution, but requires a longer write time.
The dose determines the total electron charge delivered in a given area, often expressed as $\mu C/cm^2$. This value must be chosen so that the resist is exposed correctly, to allow the desired reaction to happen, without overexposure or underexposure.

Proper focus and stigmation are also important for maintaining the required resolution. Focusing ensures that the beam has its smallest spot size at the resist surface. Stigmation is the correction of astigmatism in the electron beam, which could otherwise result in an asymmetric beam spot and directional distortions of the written features.

In this work, exposures were performed using both an F125 [120] and HS50 [121] EBL systems. For fine features on the F125, a beam current of 1 nA, a step size of 2 nm and a dose of $560\mu C/cm^2$ were used. For larger pads, the current was increased to 20 nA and the step size to 10 nm while keeping the dose constant. On the HS50, the required dose to correctly expose our resist was lower, at $275\mu C/cm^2$. Fine features were patterned using a

2 nA current. The large pads used a 20 nA current.
The difference in dose reflects differences in exposure configuration, beam conditions and tool calibration, so each machine requires its own optimized process. The F125 requires manual adjustment of focus and stigmation prior to exposure, by imaging a suitable feature on the sample to obtain a sharp image without distortion. On the HS50, this is performed autonomously by the tool, which evaluates image resolution and beam symmetry and applies the required corrections. This improves reproducibility and reduces user-dependent variations.

4.2.1 Resist spinning

For our fabrication process we used ZEP520, a positive-tone electron-beam resist commonly employed for nanofabrication. When exposed to the electron beam, the polymer chains of the active compound contained in the resist are broken, becoming more soluble in the developer. During this process, the exposed areas are removed, leaving behind a patterned resist mask that we can use for etching our devices (or, better, etching their outline).

ZEP520 is characterized by a high sensitivity (with respect to the standard alternative of PMMA), meaning that it requires a low dose for exposure, while maintaining a good resolution. It also has notable resistance to dry etching, which is particularly useful in our process, as the unexposed resist will serve as an etch mask.

Before any other operation, the samples where the bilayer was grown are brought into the cleanroom environment and cleaned with acetone, followed by a rinse in isopropyl alcohol (IPA) and dried with nitrogen (N_2).
50 µL of ZEP520 are dispensed on the sample using a precision pipette, followed by a spinning at 5000 rpm for a duration of 60 s. This leads to a resist thickness of around 200 nm [122]. This thickness allows us to maintain good resolution for fine features, with a limited aspect ratio, while having enough resist thickness to protect the unexposed areas during the etching step.
After spin coating, the resist is baked at 180 °C for 120 s, to evaporate the solvent and stabilize the film before the exposure.

4.2.2 Proximity effect correction

When electrons hit the sample, they undergo scattering events that modify their trajectory, leading to an effective exposure that is different from the one designed for. Proximity Effect Correction (PEC) accounts for these deviations, to compensate for the scattering and recover the intended layout.

When traveling toward the sample, electrons first encounter the resist, and undergo scattering events. Most of the particles are scattered at low angles inside the resist (forward scattering), producing a local broadening of the exposed region. Other electrons penetrate deeper into the stack, scatter from the underlying layers or the substrate and return up

towards the layers at a larger distance from the entrance point. This second phenomenon is known as backscattering. As a result, the effective dose received by any point is determined not only by the electrons that intentionally hit it directly, but also by electrons scattered from nearby regions. Dense patterns, where many neighboring features are exposed, can thus receive higher effective dose with respect to isolated elements. This effect can lead to linewidth variation, rounded corners and merging of adjacent features.

PEC accounts for these effects and modifies the local exposure dose according to a scattering model, that is computed from the geometry and density of the pattern. The lithography software models the electron scattering using the material stack (including the substrate, the active layers and the resist) together with the beam accelerating voltage. Based on this, the pattern is divided into regions and to each an adjusted dose is assigned, so that, after scattering, the total absorbed energy in the resist is uniform across the whole layer and the pattern is correctly transferred.

For the F125 lithographic system, the beam was operated at 125 kV, corresponding to an electron energy of 125 keV. For the HS50, the accelerating voltage and electron energy are respectively 50 kV and 50 keV. These are important parameters in the modeling as they heavily change the interaction of electrons with the material stack: higher-energy electrons tend to undergo less forward scattering in the resist, but penetrate deeper into the material and produce longer-range backscattering; lower-energy electrons' scattering happens mostly in the resist layer and therefore require a different PEC model.

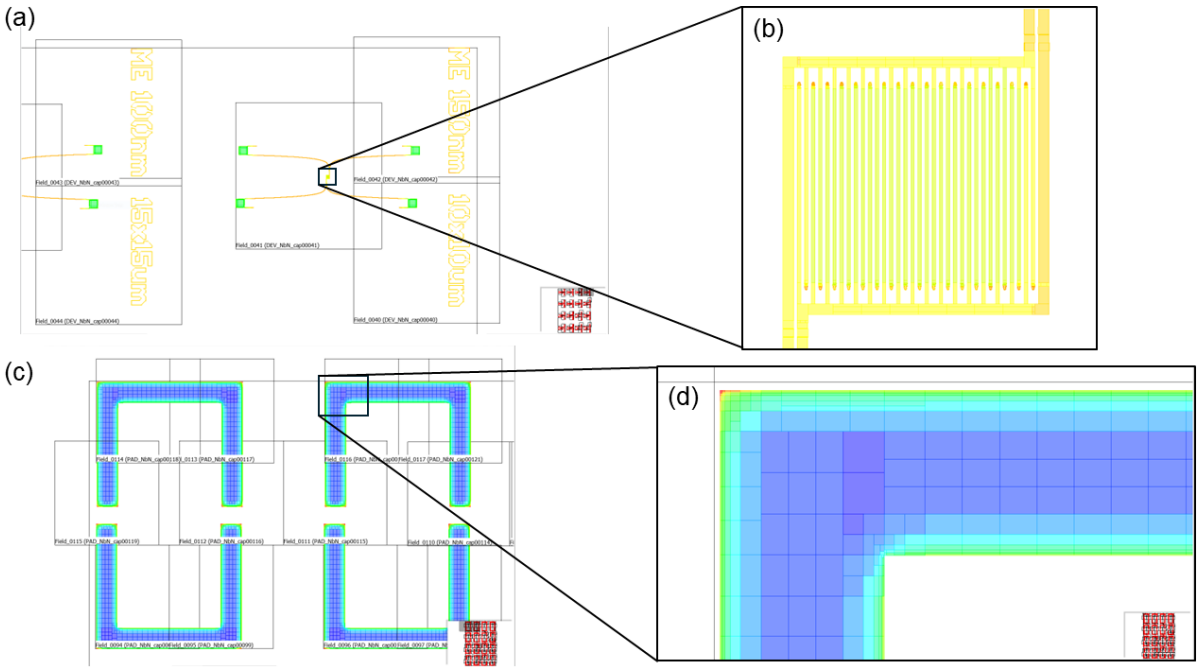


Figure 4.2: Effective dose assigned to different regions of the pattern, resulting from Proximity Effect Correction. (a) Overview of a meander nanowire and the inner tapers. (b) Detail of a meander nanowire. (c) Overview of the large pads. (d) Detail of the corner of a pad.

It is therefore paramount to correctly model the beam settings, resist thickness and material stack. Since NbN and MoSi have comparable atomic numbers and densities, a single PEC file was used for all the bilayer compositions, and this proved adequate as long

as both materials were present: stacks with 1 nm of MoSi on 4 nm of NbN and stacks of 5 nm of MoSi on sapphire gave virtually indistinguishable exposures. The same PEC file could not, however, be recycled for the pure 5 nm NbN sample, for which the absence of MoSi altered the scattering enough to produce underexposed regions (fig. 4.3), even through the ~2 nm Si capping layer. A dedicated PEC file was therefore computed for this stack.

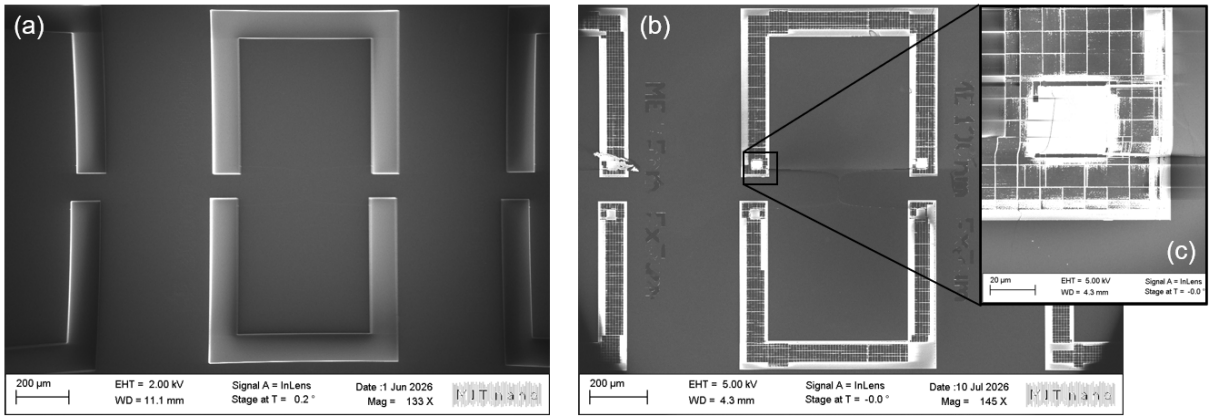


Figure 4.3: SEM images of the bonding pads. (a) Intended pad outline result, with a nice uniform etch to disconnect the device pad from the rest of the superconducting film. (b) Underexposed pad of the 5 nm NbN sample, caused by an inaccurate PEC. (c) Detail of the underexposed pad.

4.2.3 Development

After exposure, the pattern written in the ZEP520 resist must be transferred into a physical mask through development. ZEP520 is a positive-tone resist, meaning that the regions exposed to the electron beam become more soluble in the developer. During development, the exposed areas are selectively dissolved, while the unexposed part of the layer remains on the sample. This leads to openings in the resist layer corresponding to the exposed pattern, which can be used to locally etch the underlying layers, while the rest of the stack is protected by the resist that was not dissolved.

The developer we used for the ZEP resist is Xylene. The process consists of taking it from the storage fridge and pouring it in an agitator/cooler set at 0 °C. Once it reaches the target temperature, the sample is immersed in the developer bath for 90 s. The controlled temperature is a key factor in the reaction and helps the reproducibility of the process. The agitation assists in keeping the developer composition and properties uniform around the sample, and improves the removal of dissolved resist from the surface.

After development, the sample was rinsed with IPA for 30 s. This step allows us to stop the development process by washing away the xylene from the sample surface, as well as removing dissolved resist residues. Overdevelopment could enlarge the exposed openings, while underdevelopment could fail to completely remove the expose resist and prevent clean pattern transfer. The development time, procedure and temperature were kept consistent across all chips to ensure full reproducibility.

4.3 Etching

After creating the openings in the resist layer in correspondence of the designed layout, reactive ion etching (RIE) is used to transfer the pattern to the materials, removing the stack following the desired shape.
RIE is a dry etching technique that combines physical ion bombardment with chemical etching. The chip is placed in a vacuum chamber where process gases are introduced and a plasma is sparked. The plasma contains ions, electrons and reactive neutral species. The reactive species chemically react with the exposed regions of the stack, while the ions are accelerated towards the sample by an electric field. This mechanical bombardment makes the etch more directional than a purely chemical wet etch, allowing the pattern to be transferred with better anisotropy.

In this work, the etching was performed using a PlasmaTherm 210RL RIE system[123], exploiting fluorine-based chemistry. In particular, carbon tetrafluoride (CF_4) was employed as etching gas, as it is effective for removing the whole stack, composed of, from bottom to top: niobium nitride (NbN), molybdenum silicide (MoSi), silicon (Si) and its native oxide (SiO_2).
When the plasma is active, CF_4 dissociates and produces reactive species that contain fluorine. These species react with the exposed materials to form fluorinated compounds that are then removed from the surface. For instance, the layers that contain silicon can form volatile SiF_4, allowing the Si cap and the oxide to be removed. NbN and MoSi can form metal fluorides, which are then removed thanks to the ion bombardment from the plasma. The etch is stopped at the sapphire substrate, because Al_2O_3 is mechanically harder and much more resistant to the fluorine chemistry. This makes sapphire a good etch-stop layer for our stack.

Before etching the chip, the chamber had to be conditioned, to remove residual chemicals from previous processes and avoid contamination. It was performed using a SF_6/O_2 plasma for a total time of 10 min. This step is particularly important when switching from a chlorine-based process to a fluorine-based one, as chlorine sticks to the walls and is difficult to remove. Its presence could interfere with the intended reactive etching, or deposit on the sample and contaminate it. Moreover, it could alter the plasma composition and therefore the etch rate.

An important control parameter in this process is the etch timing. Depending on the etch rate, this period should be set to guarantee a small overetch, ensuring that the exposed regions are completely cleared across the whole sample, even in case of slight spatial variations in plasma concentration and resist thickness. However, too long of an etch time could erode the etch mask, causing a broadening of the features, as well as unnecessarily expose the substrate to the reactive plasma. More comments can be found in sec. 4.3.1. For all the samples in this work, the etching process consisted in 1 min etch time, CF_4 flow of 20 sccm, chamber pressure in the range of 15 to 25 mTorr and RF power

between 20 and 30 W.

4.3.1 Overetching and resist burning

Particular difficulties were encountered during the fabrication of the sample constituted of 5 nm of NbN, the only one that lacked any MoSi on top. Looking at the scanning electron microscope (SEM) images, some darker strips could be seen on top of our devices, detaching from the underlying layers and redepositing on different areas. Moreover, the tapers looked like they were only partially etched (fig. 4.4 (d))

Our first hypothesis was that the epitaxial NbN layer was delaminating, meaning that the top layers would come off the rest of the film, move around, and adhere on some other regions. This would have been the most problematic reality, as in the case of devices such as fig. 4.4(b) and (c) this would have meant shorting the nanowire to the surrounding superconducting ground plane. However, a resistance measurement with a simple handheld multimeter between one bonding pad and the surrounding layer seemed to refute this idea.

An additional possibility was that the adhesion of the Si capping layer on the NbN film was worse than on the MoSi, and that the dark strip we saw were actually the Si detaching from the substrate. To verify this option, we repeated the fabrication on a sample consisting in just 5 nm of NbN, without the capping layer. The results of the fabrication were exactly the same, so we had to rule out this possibility too.

Our final hypothesis is that the dark layers we see are actually leftover resist, that was not correctly removed by the NMP bath. This would be consistent with the persistence of this effect on all the different samples fabricated, independently of the PEC used and of the presence or absence of the capping layer.
Our RIE step used 1 min of etching time. This was probably much more than sufficient, for an overall thickness of the stack of around 7 nm. As a consequence, this long exposure of the unexposed protective resist to the energetic plasma may have cause it to get burnt, making it harder to remove from the sample in the NMP bath. This explanation seems compatible with the observation that, where the dark layer was delaminated, we could still see (even if faint) the desired shape of our nanowires (fig 4.4 (c)). Moreover, we tested these devices in the cryostat and they seemed to perform as expected, suggesting that the dark delaminated strips were not structural components of our detectors.
Future steps for this work would include testing a shorter etch time and verify this theory, making the fabrication process more predictable and reliable.

4.4 Stripping

After etching the desired path in the superconducting materials, we can remove the resist from the top of the sample, as it has already served its purpose as a protective mask and must be cleared before further characterization.

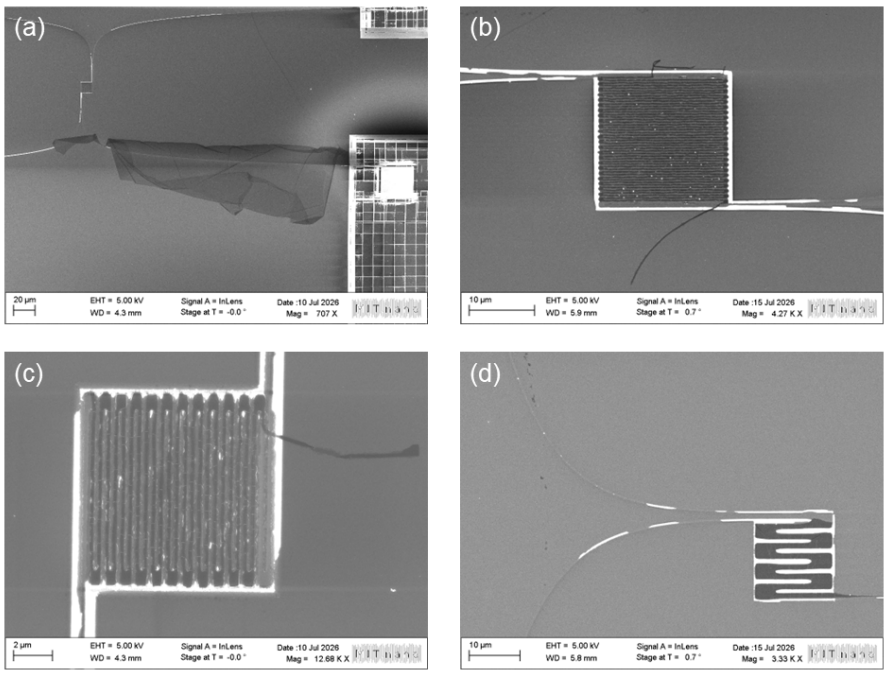


Figure 4.4: SEM images of the 5 nm of NbN sample. (a) Panoramic of the device, with a detached and folded layer of what we believe to be burnt resist. (b) Detail of the 200 nm, 20×20 µm meander nanowire, with some irregular tapers and the burnt resist detaching from the devices (c) Detail of the 150 nm, 10×10 µm meander nanowire. The resist detached from the material, but it's still possible to see the etched shape below. (d) Detail of the tapers and the booster meander. It's possible to see the irregularities in the tapers and the leftover resist on the meander.

The chips were submerged in N-methyl-2-pyrrolidone (NMP) at room temperature, with no agitation. Since the resist can become harder to remove after being exposed to the energetic plasma in the RIE step, relatively long soaking times were used to ensure complete removal. In this process, the chip was typically left in NMP for approximately 5 h, although longer stripping times up to 14 h overnight were also used.
This flexibility was possible because the exact stripping time was not highly sensitive for this process. A shorter time may have been sufficient to completely remove the resist, but leaving the sample in NMP for longer did not create problems for our material stack. NbN, MoSi, sapphire and the Si capping layer are not particularly attacked by room-temperature NMP. No agitation was used to avoid unnecessary mechanical stress on the nanostructures and the risk of delamination of the thin films. After stripping, the samples were cleaned with IPA and dried with N_2.

4.5 Wirebonding to a PCB

Once the fabrication of the devices was completed, the chip was removed from the cleanroom and mounted onto a printed circuit board (PCB) in order to connect the microscopic devices to the macroscopic measurement electronics. The PCB was specifically designed to be compatible with our cryostat setup and to route the detector signals to radiofrequency (RF) cables via Sub-Miniature Push-on (SMP) connectors. The patterned devices on the

sample, due to their nature, are too small to be contacted directly by external cables. Wirebonding provides the electrical bridge between the devices pads and the larger PCB pads connected to the cryostat wiring.

The PCB was first prepared soldering the SMP connectors onto it. To do so, the solder paste Loctite GC 10 SAC305T3 [124] was spread on the PCB footprints. The SMP connectors were then placed on top and the assembled PCB was put on a hotplate at the temperature of 250 °C until the paste assumed a shiny metallic look (indicatively 4 min). The continuity between the pads and the connectors, as well as the absence of shorts between the signal routes and ground, was checked with a handheld multimeter.
The chip was then glued onto the PCB using GE varnish [125], a resin adhesive that provides electrical insulation and good thermal conductivity, even at cryogenic temperatures. Once the chip was fixed, the electrical connections between the sample pads and the PCB pads were made using wirebonding.

Wirebonding is a microfabrication packaging technique that allows to create electrical connections between small device contact pads and external circuitry. In this work, wedge wirebonding was performed, using a West Bond 7476D system. The machine uses a manually actuated lever to precisely press a wedge tip onto the bonding pad. When the pressure is detected, ultrasonic vibration is applied, which breaks through oxides and contaminants and allows metal-to-metal contact between the wire and the pad, without needing to melt the wire. The same process is then repeated on the second pad to complete the connection. After this second bond, the wire is cut, leaving a freestanding metallic connection between the device and the PCB pad.
The wires employed are made of aluminum, contain 1% silicon, and have 25 µm diameter. Aluminum is the usual choice for wedge wirebonding because it bonds well using ultrasonic energy and does not require high temperatures, which may harm the sample.
The wedge tool used was a DeWeyl Manufacturing TCSOE-1/16-750-45-GW-1630-M wedge.

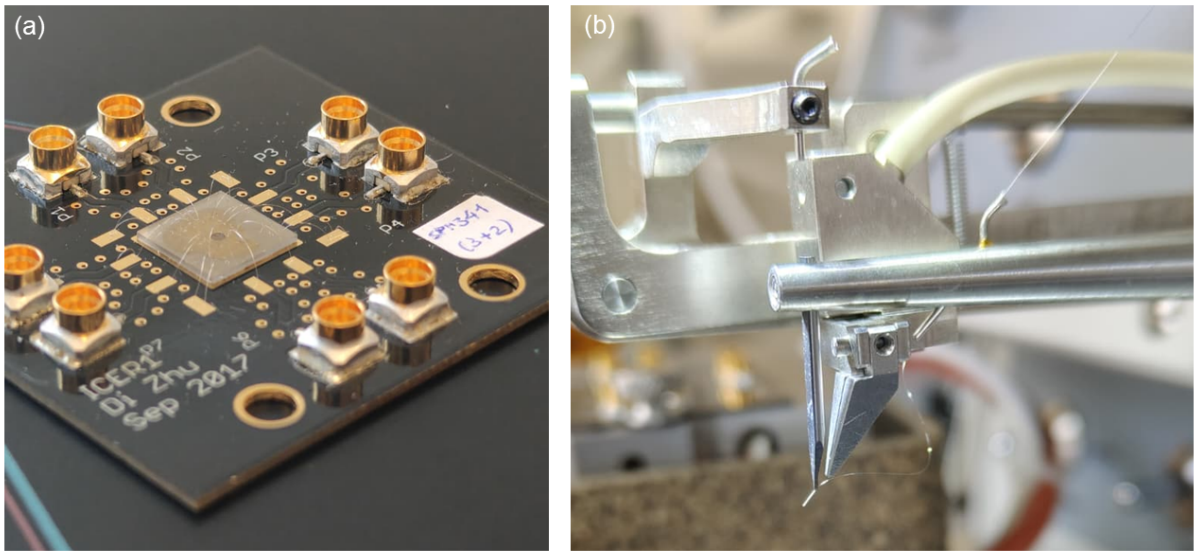


Figure 4.5: (a) Picture of the sample, attached to the PCB surface and wirebonded to its pads. (b) The wedge of the wirebonder tool, used to connect the wire to the sample. The Al wire is visible.

5 Device characterization

The samples were first characterized in terms of their material properties, measuring the thickness of the deposited films and the resulting critical temperature. A TEM analysis was conducted on the sample constituted of 1 nm of NbN and 4 nm of MoSi to check the actual thicknesses obtained and the quality of the layers and their interfaces.
After completing all the fabrication steps, the devices were structurally characterized using a Scanning Electron Microscope, before the wirebonding step.
Finally, the electronic properties were tested in a cryostat: namely, we measured the static I-V curve and the detection phenomena through trigger sweep, linearity check and photon count rate.

5.1 Thickness measurement

The first parameter characterized in the deposited structures was the film thickness in order to verify the actual dimensions and assess the reproducibility of the deposition process. Accurate thickness determination is especially important for the present study because the superconducting properties of ultrathin films can depend significantly on thickness, and the primary variable investigated in this work is the relative thickness contribution of NbN and MoSi.
The first characterization method considered was ellipsometry, an optical technique that extracts the film thickness from the polarization change experienced by light reflected from the sample. Electrical resistance measurements were also investigated as an indirect mean of estimating the layer thickness. Finally, a Transmission Electron Microscope (TEM) analysis was conducted on one representative sample to obtain a direct measurement of the individual layer thickness.

5.1.1 Ellipsometry

Ellipsometry was first considered as a non-destructive optical method to estimate the thickness of the deposited films. The analysis was conducted with a Film Sense FS-1 Multi-Wavelength ellipsometer [126]. This technique is based on the measurement of how the polarization of light changes after reflection from a sample. In a typical measurement, a beam of polarized light is shined onto the sample at a known angle of incidence. This incident light has two independent components: the p-polarized radiation is characterized

by an electric field that oscillates parallel to the plane of incidence; the s-polarized one has its electric field oscillating perpendicular to this plane.
When the light interacts with the sample, the two components are modified and reflected differently. Each one of them undergoes a modification both in amplitude and in phase, depending on the optical properties of the sample. This change is usually summarized in a complex reflection coefficient, r_p and r_s respectively. The ellipsometer does not measure these components independently, but rather their ratio

$$\frac{r_p}{r_s} = \tan(\Psi)\exp(i\Delta) \tag{5.1}$$

where Ψ describes the relative change in amplitude between the two components and Δ their phase shift. These quantities can be then compared to a model of the stack to fit the thicknesses of the different materials that could cause that precise response.
However, to obtain reliable measurements of the thicknesses for our films, we need the optical constants of each material to be known accurately and the film thicknesses to be large enough to produce a measurable optical response.
For our multilayered structure the analysis is more complicated than for a simple film. In fact, the light is not only reflected from the top surface, but partial reflections happen at each interface in the optical path, that passes through air, native silicon oxide, silicon capping layer, molybdenum silicide, niobium nitride and finally the sapphire substrate. These reflected waves can interfere with each other, depending on the thickness of each layer, its complex refractive index, and the angle of propagation inside the material.
The reliability of the measurements was strongly limited by many factors. The first is that the tool could only use one fixed angle of incidence for the emitted light, at 65°. Variable-angle ellipsometry is a more powerful technique because measuring the same sample at different angles provides additional independent information that can add constraints on the fit of the parameters to make them more accurate. With only one angle, several different combinations of thicknesses and optical constants can sometimes closely reproduce the same Ψ and Δ, especially when the films are very thin and the intensity of the signal coming from the sample is low. A second important limit was imposed by the sapphire substrate. This material is transparent over a large section of the wavelength range used in the ellipsometer, meaning that the incident light can partially pass through the substrate and be reflected by the back side of the sample. These unwanted reflections can then reach the detector and interfere with the useful signal coming from the material stack.
The difficulty in the measurement is even greater for very thin films, such as our layers that go as thin as 1 nm (expected), while the measurement is executed with light in the visible range. In this regime, the optical signature of each layer becomes very weak, and very small uncertainties in the optical parameters of the material, surface roughness, interface quality or substrate contribution can produce a large effect in the fitted thicknesses. Moreover, with such thin layers the optical parameters can easily deviate from the reference ones

obtained from bulk analysis, thus making the analysis model less accurate.

For all of these reasons, ellipsometry was useful as an initial quick and non-destructive characterization method, but it failed to give quantitative reliable measurements for our samples.

5.1.2 Resistance

Electrical resistance measurements were considered as an indirect method for obtaining information about the deposited thickness of the layers. For a homogeneous conductive film with resistivity ρ and thickness t, the sheet resistance is expressed as

$$R_s = \frac{\rho}{t} \tag{5.2}$$

The thickness could, in principle, be estimated if the resistivity of the two films were independently known.

The sheet resistance can be obtained from a four-point resistance measurement, after applying an appropriate geometrical correction factor. This correction is needed to account for the distance between the measurement pins (that provide the electrical current and measure the voltage) and to the sample edge, which constrict the current lines. In practice, however, this method is only quantitatively useful to precisely estimate the thickness when the resistivity of the deposited film is independently and precisely known.

For the NbN/MoSi bilayers, we can assume the two layers to electrically conduct in parallel. Consequently, their sheet conductances add, leading to

$$\frac{1}{R_{s,\ tot}} = \frac{t_1}{\rho_1} + \frac{t_2}{\rho_2} \tag{5.3}$$

where t_i and ρ_i are the thickness and resistivity of layer i, respectively. If the resistivity of both layers were known and one of the thicknesses could be independently determined, the other thickness could bin principle be estimated from this relation.

This approach was not used as a quantitative thickness metrology method in the present work. The room-temperature resistivity of an ultrathin sputtered film can differ substantially from the corresponding bulk value, because its electrical properties depend on disorder, stoichiometry, and deposition conditions [127]. Consequently, using resistivities from the literature to invert 5.8 would introduce an additional uncertainty that is difficult to quantify for the investigated films. Furthermore, reliable four-point measurements were difficult to obtain on the deposited samples, due to unstable electrical contact at the probe, producing fluctuations in the measured resistance.

Although the 4-point probe measurement were not suitable for quantitative extraction of the film thickness, the multimeter-measured resistance after wirebonding can qualitatively give us some guidance towards the expected thicknesses. Following the wirebonding, the electrical contact was more stable, allowing us to compare the resistance of identical devices

(nanowires with the same shape, length and width) across the different samples, by directly contacting the SMP connector of the PCB. Since the devices had the same structure, differences in the measured resistance had to be reasonably attributed to variations in the thicknesses of the constituent layers.

Looking back at eq.5.2, thinner layers yield higher electrical resistance. At the same time, following eq.5.8, we consider the parallel of the two resistances. As a very rough first approximation, we can then look selectively at the thicker layer in each of our samples, as it will have the lowest resistance and thus dominate the parallel. This means we expect lower resistance for the devices that are built on 5 nm of the same material, and higher resistance for those composed by bilayers with similar thicknesses. Additionally, MoSi generally has higher resistivity than NbN. While obtaining a single precise value would be complex, as it can depend on stoichiometry, crystal structure, impurities and many other factors, a reasonable estimation can be extracted from literature: around $300\,\mu\Omega \cdot \text{cm}$ for MoSi and $230\,\mu\Omega \cdot \text{cm}$ for NbN [105, 128].
Comparing the room-temperature resistance of identical devices across the thickness compositions, we can order them as the following (highest to lowest resistance):

1. 2 nm NbN + 3 nm MoSi
2. 3 nm NbN + 2 nm MoSi
3. 1 nm NbN + 4 nm MoSi
4. 4 nm NbN + 1 nm MoSi
5. 5 nm NbN + 0 nm MoSi
6. 0 nm NbN + 5 nm MoSi

This ordering aligns with our prediction: bilayers composed by thin layers (2 and 3 nm) have the highest resistance, with the thinner NbN leading to higher bilayer resistances (as it is not compensated by the slightly thicker MoSi, that still has comparable resistance due to its higher resistivity). The samples made of just one thicker layer show the lowest resistance, as expected. However, one element of the ordering stands out: according to our predictions, as well as the other elements of the list, we would have expected the device built on 5 nm of MoSi to have a higher resistance than the one built on 5 nm of NbN. The thickness determination of this NbN reference sample is less certain, because it was deposited under different tool conditions from the other samples, and the deposition rate may have changed. A lower-than-expected thickness would increase its resistance and could account for the observed deviation from the expected ordering.

For these reasons, the resistance measurements are used only as a qualitative consistency check, and not as an independent quantitative determination of the individual layer thicknesses.

5.1.3 Transmission Electron Microscope

Transmission electron microscopy (TEM) was used to directly characterize the thickness and morphology of the deposited films, as well as the quality of the multilayer stack and its interfaces. In contrast to techniques that estimate the film thickness indirectly through a model or calibration, TEM allows the individual layers to be directly observed in cross section. Due to the complexity of the sample preparation, only one sample was analyzed. The 1 nm NbN + 4 nm MoSi sample was selected in order to verify in particular whether the nominally 1 nm NbN layer formed a continuous film rather than disconnected islands.

TEM requires a very thin cross-sectional specimen, or lamella, through which the electron beam can be transmitted. In this work, the lamella was prepared using a Ga-based focused ion beam (FIB). Before milling, the sample was coated with approximately 25 nm of Au to provide electrical conductivity and reduce charging of the insulating sapphire substrate. A 4 µm thick Pt protective layer was then deposited on the region of interest before milling. Trenches were subsequently etched on both sides of the protected region, after which the lamella was detached, transferred to a Mo TEM grid and progressively thinned using lower ion-beam currents.

The sapphire substrate presented some difficulties during the preparation due to its hardness and insulating nature. In particular, significant redeposition of sputtered material occurred during milling, limiting the depth of the trenches that could be produced. The resulting lamella was therefore relatively small and experienced some bending, which complicated focusing during TEM imaging because different regions of the cross section were not located at the same distance from the objective lens.

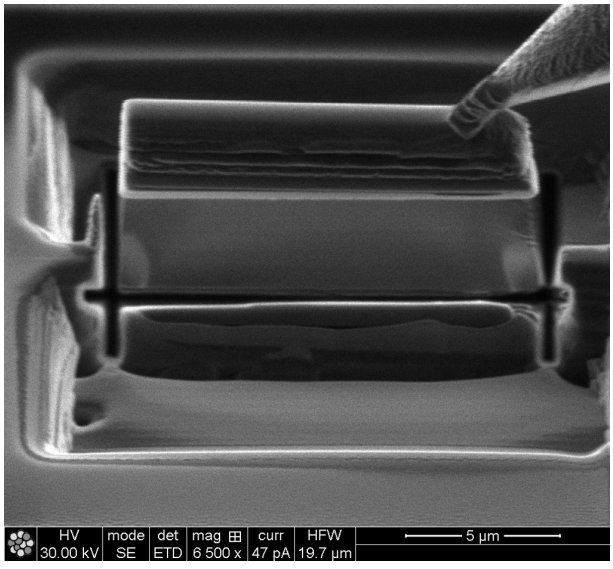


Figure 5.1: Detaching the lamella from the sample, following FIB milling

TEM contrast originates from the different interactions of the transmitted electrons with the materials in the sample. In particular, differences in composition, density, thickness and crystallinity can produce contrast between adjacent layers. Both bright-field and dark-field imaging can therefore provide information on the morphology and structural

character of the films. In this work, the calibrated scale of the TEM images was used to directly determine the thickness of the deposited layers.

Figure 5.2 shows the resulting bright-field TEM image of the cross section. From bottom to top, the crystalline sapphire substrate, the NbN layer, the MoSi layer, the Si capping layer and the Au coating can be distinguished. The NbN exhibits a non-uniform crystalline structure, consistent with its polycrystalline character, while the MoSi and Si layers show an amorphous morphology. Importantly, the NbN layer appears continuous across the imaged region, confirming that a nominal thickness of 1 nm was sufficient to form a continuous film rather than isolated islands.

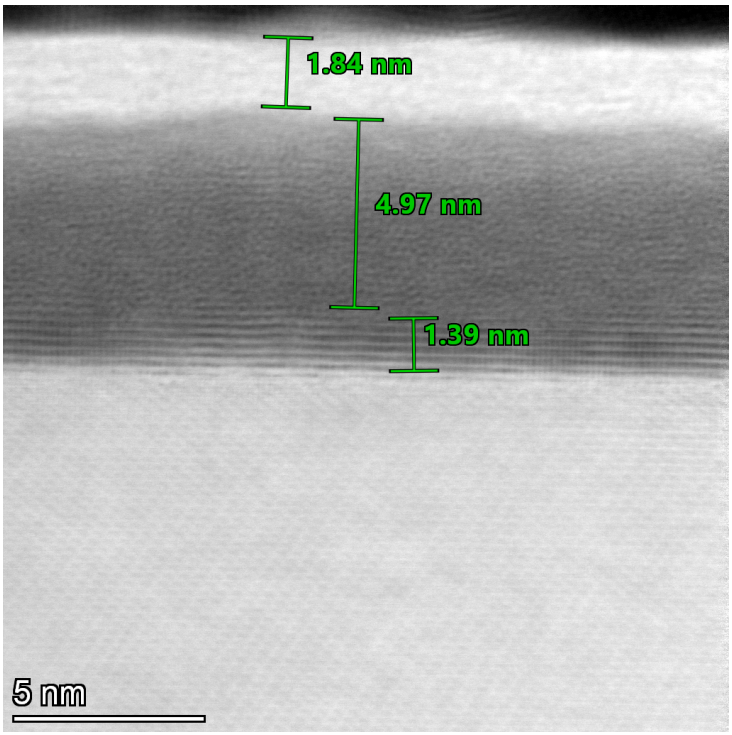


Figure 5.2: Bright-field TEM imaging of the sample. From bottom to top, it's possible to distinguish the crystalline sapphire substrate, the polycrystalline NbN (nominally 1 nm), the amorphous MoSi (nominally 4 nm), the Si capping layer and the gold on top.

The calibrated image scale also allows the actual thicknesses of the deposited layers to be estimated. The NbN layer was found to be approximately 1.3 nm thick, compared with the nominal 1 nm, while the MoSi layer was approximately 5 nm thick instead of the nominal 4 nm. The Si capping layer was approximately 2 nm thick and is not part of the active detector stack. The measurements therefore indicate that the deposition rates of both materials were slightly underestimated during fabrication. Moreover, possible bending of the lamella can cause the multilayer stack to be viewed at a finite angle. If the local layer normal is tilted by an angle θ out of the image plane, the thickness measured is

$$t_{\mathrm{TEM}} = \frac{t_{\mathrm{true}}}{\cos\theta} \tag{5.4}$$

Nevertheless, the relative thicknesses of NbN and MoSi remain close to the intended values, making the samples suitable for investigating the effect of the bilayer composition

on the detector properties.

Energy-dispersive X-ray spectroscopy (EDS) was performed together with TEM to investigate the elemental composition of the multilayer and, in particular, to assess the quality of the interfaces and the possible presence of alloying or cross-contamination between adjacent layers. When the electron beam interacts with the sample, characteristic X-rays are emitted following electronic transitions within the atoms. Measuring their energies allows the elements present in the sample to be identified, while recording the spatial origin of the X-rays enables elemental maps to be reconstructed.

For very thin layers, the finite size of the electron probe and the interaction volume can result in signals from neighboring layers being partially mixed. In addition, characteristic X-ray peaks from different elements can overlap in energy. Despite these limitations, EDS was particularly useful in this case because the expected elemental composition of the stack was known in advance.

The EDS results are shown in fig. 5.3. The elemental maps confirm the expected composition and spatial arrangement of the different layers. In particular, the Nb signal is confined to the thin NbN layer at the bottom of the active stack, while Mo and Si are associated primarily with the MoSi layer. Al is predominantly detected in the sapphire substrate, whereas Si is also present in the capping layer. The spatial distributions of the elements are well defined, with no evident broadening of the Nb, Mo or Si profiles that would indicate significant intermixing at the NbN/MoSi interface. This supports the conclusion that the two deposited materials form distinct layers rather than a strongly intermixed alloy.

Oxygen is predominantly detected in the sapphire substrate and in the Si capping layer, where its presence is likely related to oxidation following exposure to ambient conditions. However, weaker oxygen signals can also be observed throughout the active stack. These signals may partly originate from contamination or redeposition during FIB preparation, particularly given the difficulties encountered during milling of the sapphire substrate. An alternative possibility is oxygen diffusion from the substrate into the deposited layers. This interpretation is consistent with the observed increase in room-temperature resistance of devices after several days of storage, which was particularly pronounced for the 5 nm NbN sample but was also observed in samples containing predominantly MoSi.

Overall, the combined TEM and EDS analyses provide direct evidence that the deposited bilayer consists of distinct and continuous NbN and MoSi layers, with thicknesses close to the intended values and well-defined interfaces. The analysis therefore confirms that the fabrication process successfully produced the nanoscale bilayer structure required for the investigation of proximity effects in the SNSPDs.

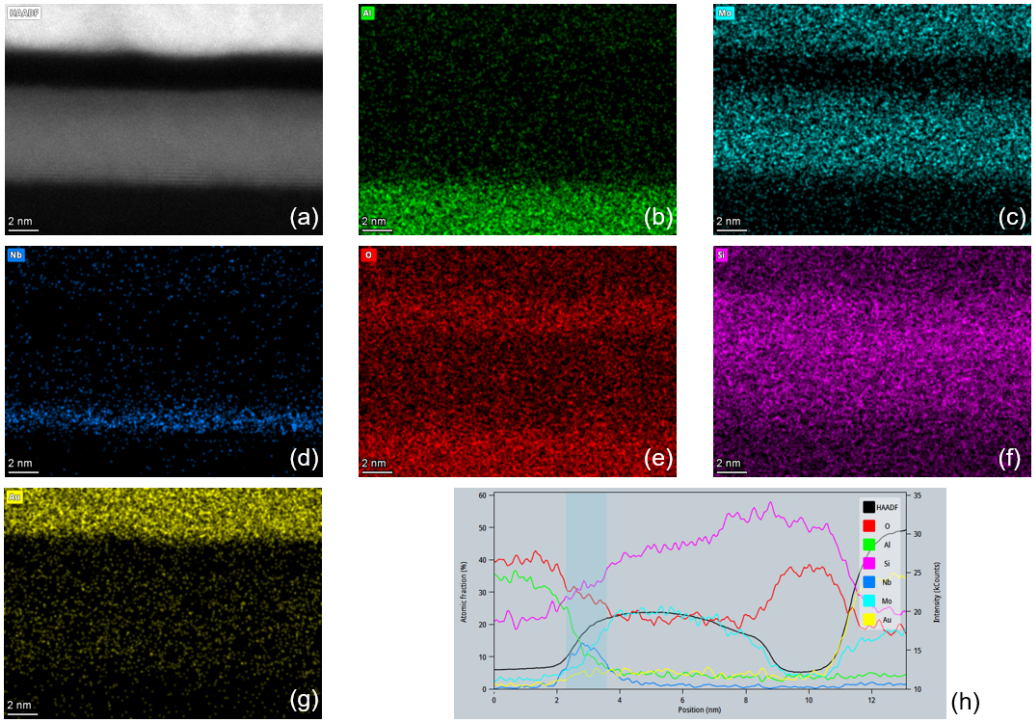


Figure 5.3: EDS analysis of the sample built on 1 nm NbN + 4 nm MoSi. Picture (a) shows a TEM image of the cross section of the sample, highlighting the structural and compositional differences. Images (b)-(g) show the spatial distribution of specific elements, reconstructed from the characteristic energies emitted by each atom during the EDS analysis. Namely, the investigated elements are aliminum (b), molybdenum (c), niobium (d), oxygen (e), silicon (f) and gold (g). Image (h) reports the average intensity of each trace across the thickness of the sample.

5.2 Critical temperature in the MPMS

The superconducting transition temperature of the deposited bilayers was characterized using the cryogenic measurement apparatus MPMS (Magnetic Property Measurement System [129]). This tool combines precise temperature control together with a superconducting magnet, allowing electrical measurements (such as the resistance of our bilayer) as function of both temperature and applied magnetic field.

For each bilayer thickness combination, the deposition was performed on two substrates at the same time. They were carefully put in similar positions on the sputtering system chuck, and rotation was enabled, so that they experienced nominally identical deposition conditions, such sputtering rates, plasma conditions, and substrate position. While one of the two samples was subsequently used to fabricate the devices, the second one was kept as reference for material characterization.

For electronic transport measurements, a small piece of the sample is mechanically fractured from the substrate and mounted on a PCB connected to the probe on the instrument. A 4-wire measurement scheme is employed (fig. 5.4) in which two electrical contacts provide the current that flows into the film, and two separate contacts measure the voltage drop. This allows a more precise resistance measurement to be obtained, bypassing the resistance that would be introduced by the probe wires in a standard 2-wire resistance measurement.

For each sample, the changes in resistance as we swept through the temperature

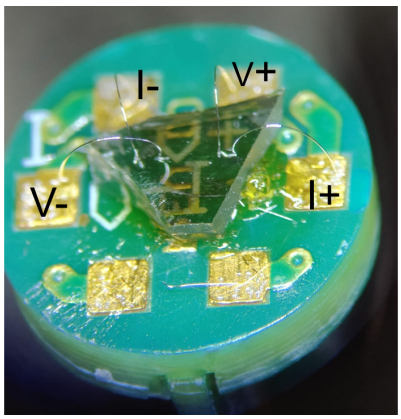


Figure 5.4: Optical microscope image of the MPMS PCB, with the 4-point resistance measurement setup.

were recorded, as at several fixed values of applied magnetic field. At high temperature, above the superconducting transition, the bilayer is in the normal state and has a finite resistance. When the temperature is lowered and the critical temperature is approached, superconducting correlations develop in the material and the sample resistance drops to zero with a somewhat sharp transition.

When a magnetic field is applied, it is expelled from the bulk of the superconductor. This phenomenon is known as the Meissner effect. The applied field suppresses superconductivity, resulting in a decrease of both the critical temperature and the critical current. By repeating the temperature-sweep resistance measurements at different applied magnetic fields, we can characterize how superconductivity is suppressed. An increasing magnetic field also often lead to a broadening of the superconducting transition.

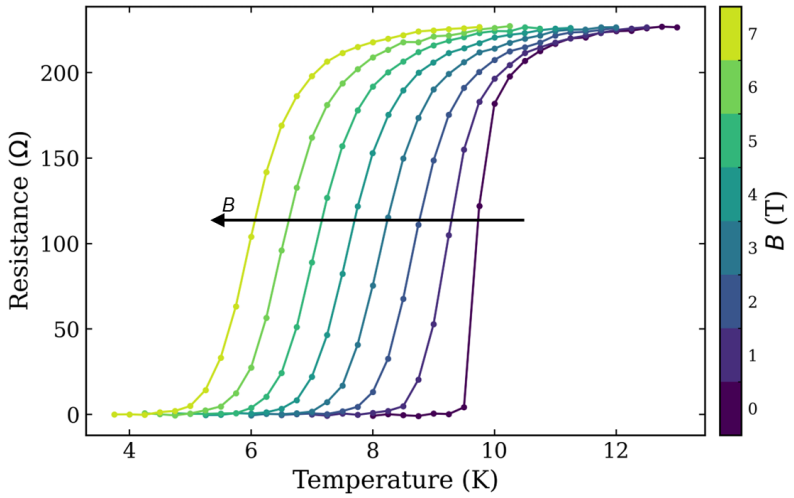


Figure 5.5: Resistance vs temperature at different applied magnetic fields for the sample of 4 nm of NbN + 1 nm of MoSi. Notice how the transitions broadens as we increase the applied magnetic field, and shifts to lower temperatures.

The critical temperature was extracted from each resistance curve at the point in which the resistance of the film reached half of its high-temperature value. This does not correspond to the room temperature resistance, but rather to the resistance measured above the superconducting transition (6 K to 14 K, indicatively). The 50% criterion is

commonly used in superconducting transport measurements, because the superconducting transition is often not infinitely sharp, and this provides a reliable and repeatable method to obtain a reference value, across different samples and different applied magnetic fields. Other possible definitions, such as the 10% or 90% resistance criteria, or a representative fixed value of $2\,\Omega$ could have been used.

Since the temperature sweeps contained a finite number of measured points, the experimental data did not usually contain a point at exactly half of the high-temperature resistance. Therefore, the critical temperature was obtained by a linear interpolation between the two measured points closest to this threshold.

5.2.1 Diffusion coefficient

Repeating the resistance measurement as function of temperature, for different applied magnetic fields, provides a set of $T_c(B)$ values for each sample. The field dependence of the superconducting transition contains information about the upper critical field and, within an appropriate regime, can be used to extract the electronic diffusion coefficient D of the bilayer.

This parameter describes how electrons move through a disordered conductor when their motion is not ballistic, but is instead dominated by elastic scattering arising from disorder, impurities, grain boundaries or interfaces. The mean-square displacement arising from this random walk is

$$< r^2 >= 2nDt \tag{5.5}$$

where t represents the time and n the number of spatial dimensions.

In a simple isotropic three-dimensional model, the diffusion coefficient D can also be related to the Fermi velocity v_F and the elastic mean free path ℓ as

$$D = \frac{v_F \ell}{3} \tag{5.6}$$

The conditions that determines whether the dirty limit of superconductivity holds is not set directly by the film thickness. Rather, the elastic mean free path must be significantly shorter than the clean-limit superconducting coherence length

$$\ell \ll \xi_0. \tag{5.7}$$

In this regime, the quasiclassical description provided by the Usadel equations can be applied. Experimental studies on ultrathin NbN [75] and MoSi [105] have reported short mean free paths characteristic of strongly disordered superconducting films, supporting the use of a diffusive description for materials such as the ones investigated in the present work.

In the dirty limit, the coherence length is governed by the diffusion coefficient rather than directly by the Fermi velocity. Up to numerical prefactors depending on the convention

used, the dependence can be expressed as

$$\xi \sim \sqrt{\frac{\hbar\ D}{k_B\ T}} \tag{5.8}$$

Hence, D determines the characteristic length scale over which superconducting correlations propagate. This makes it an important parameter for proximity-coupled bilayers, where superconducting correlations diffuse across the constituent layers.

The diffusion coefficient is also one of the key input parameters for the theoretical modeling based on the Usadel equations, as it appears explicitly in the differential equations governing the Green's functions. Therefore, extracting these measurements from the deposited bilayers is important for connecting the experimental material properties to modeling framework.

The suppression of superconductivity by a magnetic field can be described in terms of the upper critical field B_{c2}. In a type-II superconductor [1], the applied magnetic field introduces orbital pair breaking and leads to spatial variations of the superconducting order parameter. As the applied field approaches the limit represented by B_{c2}, superconductivity is suppressed throughout the sample. Close to T_c, the Ginzburg-Landau expansion for a diffusive superconductor gives a linear temperature dependence on the upper critical field [1]

$$B_{c2}(T) = \frac{4k_B}{\pi e D}(T_{c0} - T) \tag{5.9}$$

This linear dependence is expected only sufficiently close to the resistive-superconductive transition, where the Ginzburg-Landau expansion is applicable. Conversely, we can extract the critical temperature as a function of the applied field

$$T_c(B) = T_{c0} - \frac{\pi e D}{4k_B} B \tag{5.10}$$

where T_{c0} denotes the zero-field critical temperature. Consequently, a linear fit on the experimentally measured $T_c(B)$ dependence provides an estimate of the diffusion coefficient

$$D = -\frac{4k_B}{\pi e}\frac{dT_c}{dB} \tag{5.11}$$

This relation is commonly referred to as the Larkin-Ovchinnikov result for dirty superconductorsc [130] and can be derived from microscopic theory of superconductivity in the diffusive limit. The main assumptions behind this result is that the film is in the dirty limit (reasonable, considering the thicknesses involved) and that the suppression of superconductivity is dominated by orbital pair breaking caused by the applied magnetic field.

Typical literature values for the diffusion coefficients in ultrathin sputtered superconducting films are of around $5 \times 10^{-5}\mathrm{m}^2/\mathrm{s}$ for both NbN [75] and MoSi [131].

The diffusion coefficients extracted from the MPMS measurements lie in a relatively

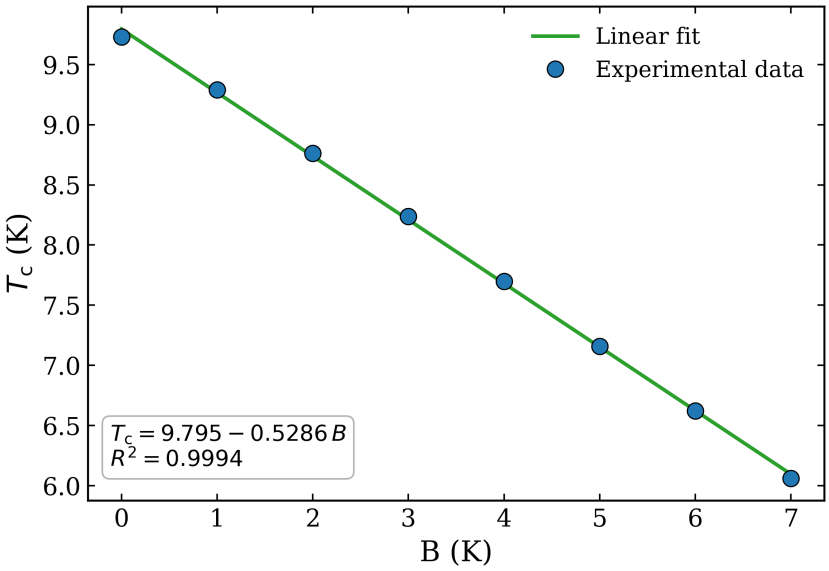


Figure 5.6: Critical temperature vs applied magnetic field for the sample of 4 nm of NbN and 1 nm of MoSi. The linear correlation is highlighted.

Table 5.1: Diffusion coefficient and critical temperature for the different bilayers, extracted from the MPMS measurements.

NbN (nm)	MoSi (nm)	D ($m^2\,s^{-1}$)	T_c(K) at $B = 0$
5	0	5.50×10^{-5}	12.23
4	1	5.80×10^{-5}	9.80
3	2	5.38×10^{-5}	6.52
2	3	5.52×10^{-5}	5.71
1	4	5.67×10^{-5}	4.52
0	5	5.21×10^{-5}	3.93

narrow range, from 5.2×10^{-5} to $5.8 \times 10^{-5}, m^2/s$. These values are consistent with those reported for ultrathin disordered NbN and MoSi films. No clear monotonic dependence of D on the composition is observed within the experimental uncertainty. This is plausible, as the diffusion coefficient depends on the elastic scattering rate and can therefore be sensitive to disorder, interfaces and grain boundaries, effects that are dominant at these scales. Since the constituent films are strongly disordered, variations in these scattering mechanisms can obscure a weak dependence on the intrinsic diffusion coefficients of NbN and MoSi.

More information can be obtained from the measured critical temperatures. We can first notice that the measured transitions for the 5 nm of NbN and MoSi happen at lower temperatures than the reference bulk layers: respectively, 12.23 K instead of 16 K [72], and 3.93 K instead of 5.5 K. Such a reduction of T_c with decreasing thickness is well established in ultrathin superconducting films.

For the bilayers, the measured trend in T_c follows the expected behavior: a greater composition percentage of the lower-T_c material results in a lower critical temperature of

the combined bilayer. This is consistent with the proximity effect, as we expect the two materials to behave not as completely independent layers, but as a hybrid effective material with intermediate properties. The appropriate reference points are the experimentally measured 5 nm NbN and MoSi films rather than their bulk critical temperatures because the intrinsic superconducting properties of the ultrathin constituent layers are already modified by their finite thickness. A more quantitative analysis of the composition dependence of T_c and its comparison with the Usadel model is presented in Chapter 6.

5.3 Scanning Electron Microscope

Scanning electron microscopy (SEM) was used to inspect the fabricated devices and evaluate the quality of the nanopatterning. SEM forms an image by scanning a focused electron beam across the sample surface and detecting electrons emitted as a result of the interaction between the beam and the sample. To study the ultrathin samples of this work, imaging was based primarily on secondary electrons, which provide high-resolution information about surface morphology and the edges of patterned structures.

The main purpose of the SEM analysis was to identify significant fabrication defects before testing the devices in the cryostat. The images were evaluated qualitatively rather than used for precise dimensional measurements. In particular, they were used to verify that the nanowires presented no discontinuities and were approximately uniform in width, and to identify scratches, particles, residues, constrictions and other patterning irregularities. Since the superconducting layers were only approximately 5 nm thick, SEM was not viable to determine their thickness.

Most images were acquired at an accelerating voltage of about 5 kV, with a mixing of the signals coming from the in-lens detector and the Everhart-Thornley (SE2) detector, with a predominant contribution of the former. The in-lens detector provided strong edge contrast and was particularly useful for examining the patterned nanowires, while the SE2 detector contributed additional topographic information about the sample surface.

Some charging was observed because of the insulating sapphire substrate and Si capping layer. When charge accumulates on the imaged region, it perturbs the trajectories of the incident and emitted electrons, producing image drift, distortion or blurring during acquisition. Nevertheless, charging was not severe enough to prevent reliable inspection of the patterned structures, partly because the conductive NbN and MoSi layers helped to dissipate the accumulated charge.

The SEM inspection provided a first assessment of the fabrication outcome and was used to screen devices before cryogenic characterization. Some devices were considered unsuitable for testing because of major defects, including scratches, dust particles, incomplete exposure or incomplete etching. Other devices exhibited less severe imperfections, such as local constrictions, edge irregularities or small variations in the apparent nanowire width. These observations aided the selection of devices for subsequent measurements and

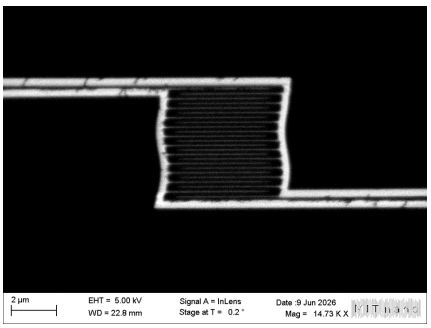


Figure 5.7: SEM image distorted by the charging effect.

provided useful context for interpreting their electrical performance.

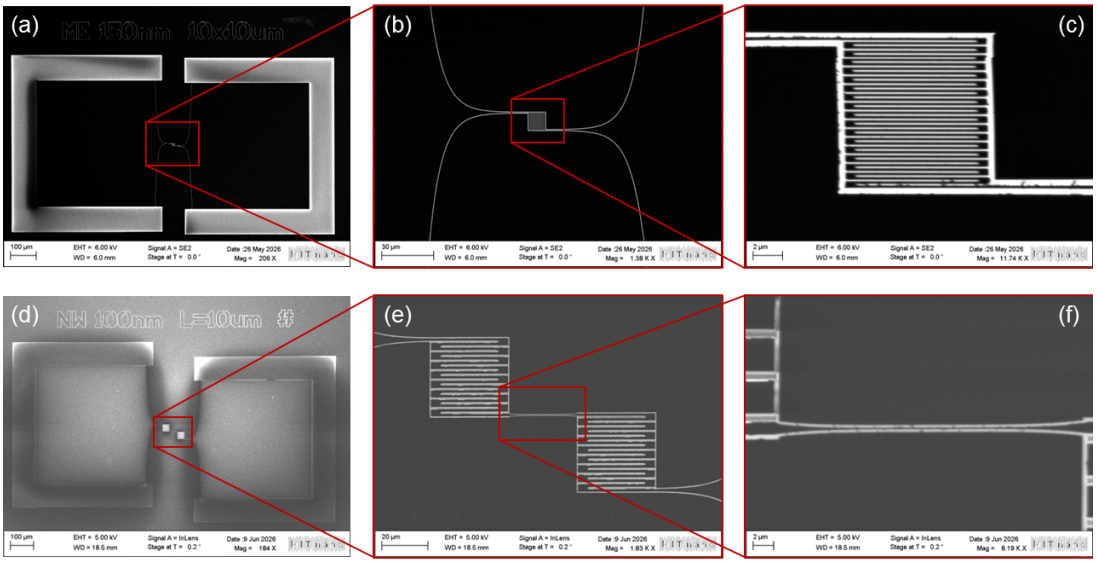


Figure 5.8: SEM images with progressive zooms of successfully fabricated devices. On the top (a)~(c), a 150 nm, 10×10 µm meandered nanowire on the 1 nm-NbN + 4 nm-MoSi sample. On the bottom (d)~(f), a 100 nm-long, 10 µm-wide nanowire on the 3 nm-NbN + 2 nm-MoSi sample.

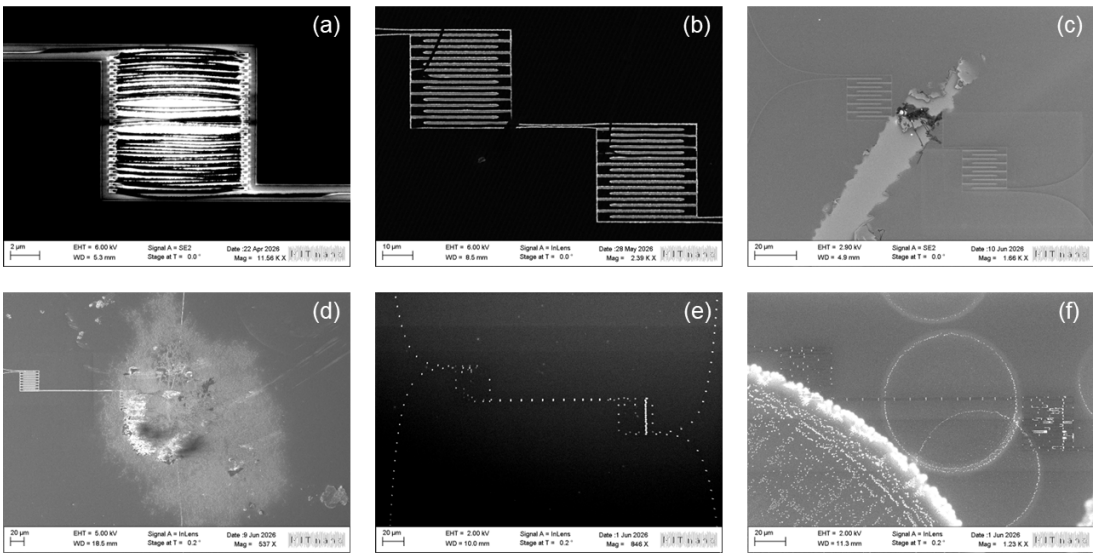


Figure 5.9: SEM images of failed devices. (a) Deformed 75 nm meandered nanowire. A likely fail in the exposure caused the linear traits to bend and the neighboring sections to merge. (b) Straight nanowire with booster meanders. Some scratches or deposited strips interrupts the continuity of our nanowire. (c) A scratch destroyed the meandered nanowire. (d) Some dust or other kind of contamination was deposited on the sample in correspondence of the tapers and booster meanders. (e) Underexposed device. Instead of a clean continuous outline, only some intermittent points were etched. (f) Underexposed device with some deposited contamination, likely coming from the development process in xylene or from the stripping in NMP.

5.4 ICE cryostat

After characterizing the intrinsic properties of the bilayer stack, we tested the fabricated nanowire single-photon detectors at cryogenic temperatures, using a closed-cycle ICE (Innovative Cryogenic Engineering) Oxford cryostat, capable of reaching temperatures as low as 1 K. The entire setup was built to provide stable temperature, low electrical noise, the desired bias current and controlled optical illumination. The experimental procedure therefore involved mounting the devices inside the cryostat, verifying electrical and optical access, cooling the system under vacuum and performing the desired static and dynamic measurements.

The refrigeration technique is based on a Gifford-McMahon type of cryostat: in this closed-cycle cryostat helium gas is compressed externally and then circulated through a cold head, allowing it to extract heat from the cold stages. A moving displacer and a regenerator are used to allow the cycling compression and expansion of the gas, to reach a temperature lower than that provided by the cryogenic liquid itself.
The sample space is enclosed by three nested thermal and radiation shields. The innermost region contains the cold stage and the devices under test. Around this central region, a solid copper cylinder, an intermediate shield covered with aluminum foil and a third metallic shield are positioned and tightly sealed, to reduce the heat injection from warmer parts of the cryostat and from the room-temperature environment.

Before cooling down, the cryostat is evacuated. Pumping the region to high vacuum helps to reduce heat transfer by gas conduction, as well preventing condensation of water vapor and other residual gases on the cold surfaces. After the vacuum is established, the cryostat is cooled down to the base temperature of 1.3 K, at which most of the characterizations were performed. The cryostat also possesses a heater that, in conjunction with a control of the needle valve to regulate the cooling power of the incoming cryogenic gas, could be used to tune the temperature up to 5 K.

After wirebonding, the PCB containing the devices was mounted in the cryostat with a thermal paste on the back surface, to ensure appropriate thermal contact. The radio-frequency lines were connected to the SMP connectors on the PCB, and the corresponding coaxial lines were routed from the cold stage to the top of the cryostat, where they could be connected to the external world. There, they could be connected to room-temperature electronics for biasing and readout of the signal. The use of RF lines was important because the SNSPDs counting events are usually fast transient signals, with typical rise times and pulse widths in the nanoseconds range.

Optical access was provided by an optical fiber inserted from the top of the cryostat and aligned to make sure that the incoming radiation was directed on the sample surface (fig. 5.11). Before entering the cryostat, the light passed through a variable optical attenuator [132]. We did not measure the absolute intensity of the optical signal at the sample position, which would have been affected not only by the source, but also by connector losses, fiber alignment and losses, transmission through the cryostat feedthrough, and the optical coupling to the active area of the device. However, controlled attenuation allowed us to relatively scale the photon flux reaching the devices.

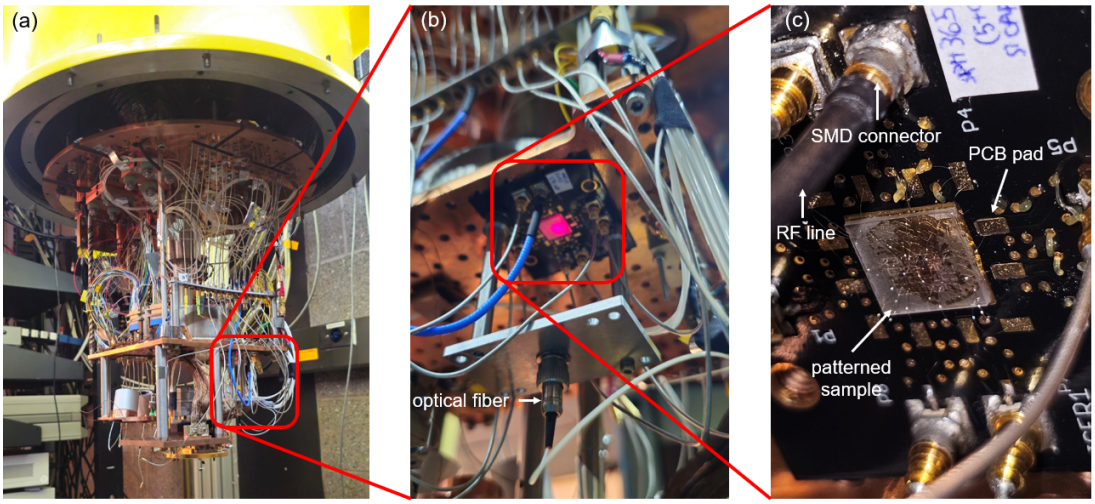


Figure 5.10: Picture of the setup in the ICE cryostat. (a) overview of the core of the cooling system. (b) mounted PCB and alignment with the optical fiber. (c) detail of the electrical connection from the device, to the PCB and the readout electronics.

The characterization was divided in two main parts, depending on the required electrical setup. First, static measurements were performed to determine the superconducting switching current and retrapping current of each device. Second, dynamic photon-counting

measurements were performed under dark and illuminated conditions. These were used to verify the detection properties of our devices.

An SNSPD operation can be summarized as follows: the superconducting nanowire is biased close to its switching current, making the superconducting state more precarious and lowering the superconducting energy gap. When a photon is absorbed, if it carries enough energy and we are close enough to the resistive transition, it can create a resistive hotspot or assist the entry of vortices. This local perturbance can then grow into a temporary resistive region that spans across the nanowire. Since the device now has nonzero resistance, the bias current is now diverted into the readout circuit (with a typical coupling impedance of 50 Ω), producing a voltage pulse. After this detection event, the nanowire can cool back down and return to the superconducting state, ready to detect another photon.

In the following, the schematics of the electrical setups for the different measurements are reported.

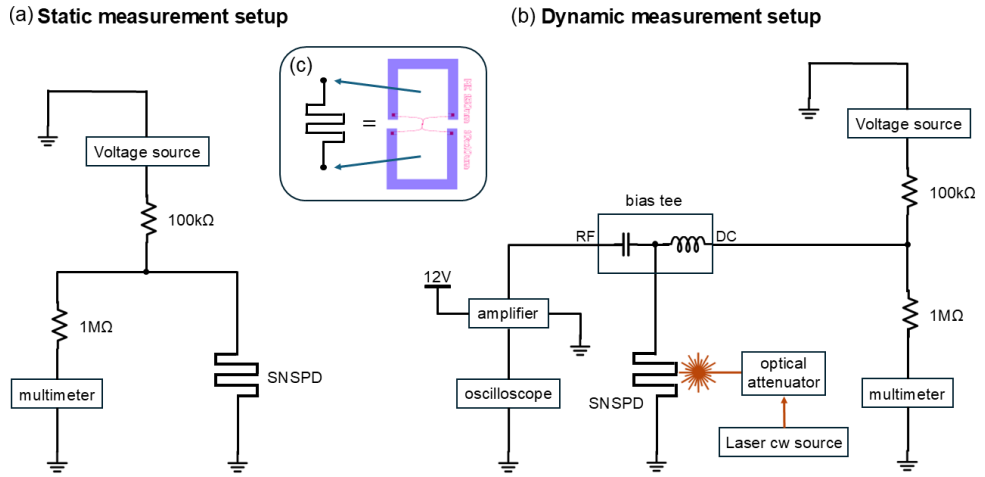


Figure 5.11: Schematic of the opto-electronic setup for the SNSPDs characterization. (a) Setup for the static switching and retrapping currents measurements. (b) Setup for characterizing the detection events. (c) Physical device correspondence of the SNSPD circuital symbol.

Let's first analyze the simpler static measurement setup. While in the superconducting state, the nanowire has null resistance. In the normal state, its resistance increases to the order of kΩ. In both cases, this value is much smaller than the ~GΩ input impedance of the multimeter [133] (to which we added a 1 MΩ resistor). This means the current forced by the independent voltage source flows almost entirely into the nanowire. Under this approximation, the same bias current I_b flows through the nanowire and the 100 kΩ bias resistor. The multimeter then measures the voltage across the nanowire, that we can indicate with V_{dev}.

When the device is in the superconducting state and has zero resistance, the only resistance seen by the voltage source is the 100 kΩ provided by the biasing resistor. Under this operating regime, we can consider the set of voltage source and biasing resistor together

as a current source, and we can impose the desired bias current I_b by setting the voltage source to a value $V_\mathrm{source} = 100 \times 10^3 \; I_\mathrm{b}$.

This is no longer true when the nanowire switches to the normal state and has finite resistance R_dev. In that case, we still control V_source and measure the device voltage V_dev. By analyzing the circuit, we obtain the relations

$$\begin{cases} I_b = \frac{V_\mathrm{source}}{R_\mathrm{dev}+100k\Omega} \\ I_b = \frac{V_\mathrm{dev}}{R_\mathrm{dev}} \end{cases} \tag{5.12}$$

where the two unknowns are I_b and R_dev. We can then solve the system and obtain the voltage across and current through our device, allowing us to build its I-V characteristic (5.4.1). Note that if the nanowire is in the superconducting state and thus has zero resistance, the two relations are equal.

The second circuit represents the operating conditions for characterizing the detection events. In this case, the nanowire only temporarily switches to the resistive state in correspondence of detection events, but is normally kept in the superconducting state. We can thus impose the desired I_b through the voltage source and the bias resistor. When the nanowire switches to the resistive state, however, the current is now diverted into the readout branch of the oscilloscope, with characteristic coupling impedance of $50\,\Omega$. The voltage measurement provided by the multimeter in this second configuration is no longer used to determine the device resistance, but the sudden increase from zero (when the nanowire is superconducting) to a finite value (when the nanowire has greater resistance and the current is diverted into the oscilloscope branch) allows to recognize switching events and latching.

The bias-tee decouples the DC and AC components of the signal. The DC component is the V_dev we previously defined, while the AC component is the signal originating from the detection event. Low-noise amplifiers before the oscilloscope increase the amplitude of the useful signal. The counter keeps trace of the number of times our signal crosses the threshold we set as the trigger level.
Different laser wavelengths were used to test the detectors. When the 1550 nm was employed, an attenuator was also used to control the intensity of the light reaching the sample. This was not possible for the 780 nm wavelength, as the variable attenuator was not compatible with this range. In that case, fixed optical attenuators were used when needed, by connecting them to the optical fiber.

5.4.1 I-V curve

The first measurement performed was the current-voltage characteristic of each nanowire. Starting from zero, the bias voltage provided by the voltage source was slowly increased while measuring the voltage across the device. At low enough bias current, the nanowire retains its superconducting state and the voltage drop is ideally zero. As we keep increasing

the current, the device eventually switches to the resistive phase, in correspondence of the switching current I_{sw}. The control of the voltage source, together with the measurement of the voltage drop across the device, allow to determine the complete IV curve of the device and calculate its resistance for each experimental point.

After a the switching current is reached and the nanowire transitions into the resistive state, bias is gradually reduced, monitoring at which value the device stabilizes back in the superconducting state. This usually happens at a value, the retrapping current I_{r}, much lower than the one that originally caused the switching. This results in a hysteretic current-voltage curve, where increasing and decreasing current sweeps follow different paths.

The reason for the difference between these two values of current lies in the Joule heating: once the devices switches and acquires a finite resistance, the I_{b} is still forced through it because of the high resistance presented by the multimeter branch. Consequently, a power $P = I_{\mathrm{b}}^2 R_{\mathrm{dev}}$ is dissipated inside of it and keeps it locally hot. As long as the bias current remains sufficiently high, even if lower than the switching current that caused the transition, the generated heat prevents the wire from cooling and relaxing to the superconducting state. To go back to the superconductive state the bias current must be reduced even further, to the value we described as the retrapping current, to compensate for the power injected by joule heating.

Note that the switching current must be considered as an intrinsically experimental value: it can easily be affected by electronic noise, that can introduce perturbations into the nanowire and cause it to switch prematurely. At the same time, biasing a device close to the threshold for a longer time results in a higher probability of a switching event, making it so that slower sweep can yield lower I_{sw}.

Most of the devices showed a clean hysteresis curve, with a vertical section along the current axis (corresponding to the superconducting state, in which the current can flow without voltage drop) and two symmetric branches in the first and third quadrant corresponding to the resistive state, before merging back into the vertical section when the bias current gets sufficiently low. Some devices, however, show multiple resistive branches, with different slopes (and, consequently, resistances). The origin of this behavior is likely to be found in constrictions present in the nanowire, that is to say sections in which the width is reduced due to fabrication defects. These smaller sections limit the current that the nanowire can carry, causing a first switching event that concerns only that small region, while the rest of the nanowire, with a wider nominal cross section, remain superconducting. As we keep increasing the current, more sections of the wire with increasing width switch from the superconducting to the resistive state, leading to a jump in the corresponding branch, characterized by higher resistance. Once all the sections have switched, the relaxation mechanism is the same as the more ideal uniform nanowires.

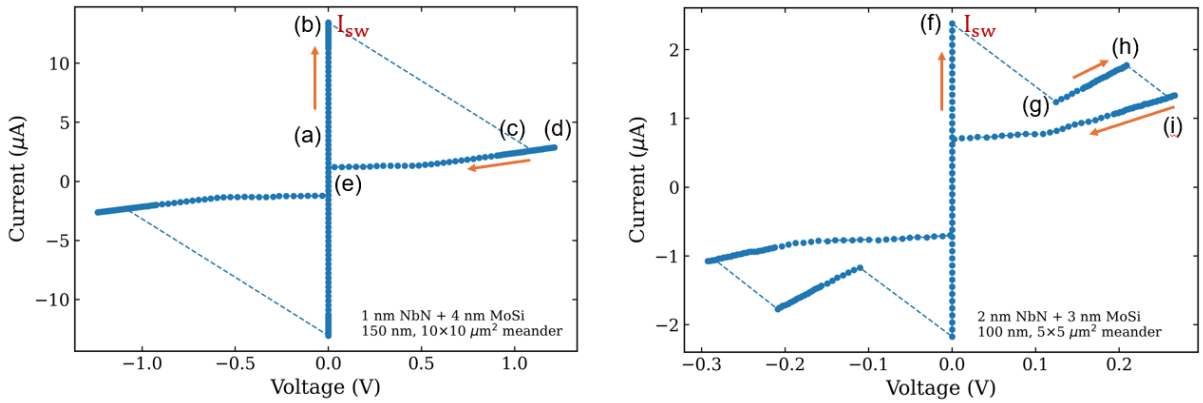


Figure 5.12: IV characteristic of a 150 nm, 10×10 µm meander nanowire (on the left) and of a 100 nm, 5×5 µm meandered nanowire (on the right), for the 1 nm NbN + 4 nm MoSi and 2 nm NbN + 3 nm MoSi samples respectively, at 1.3 K. For the former, we can observe the zero-resistance superconducting state (a), until we reach switching current (b) and jump to the resistive branch (c). The current can increase, together with the voltage, in that state (d), and when it becomes again low enough the device retraps into the superconducting state (e). The mechanism for the second device shown is the similar, but due to irregular constrictions first a narrow section of the wire switches, making it transition from the superconducting state (f) to a smaller-resistance branch (g). If the current increases enough (h) another section switches, causing the jump to a higher-resistance branch (i).

5.4.2 Dynamic measurements

After verifying the superconductivity of the devices and their ability to switch, the detectors were characterized dynamically by shining light on them and measuring voltage pulses generated by the detection events. For all dynamic measurements, counts were recorded over a fixed acquisition time. If N counts were measured during a measurement time t_{meas}, the corresponding count rate was calculated as $R = \frac{N}{t_{\text{meas}}}$.
Measurements were performed both in the dark (with no illumination coming inside the cryostat via the optical fiber) and under illumination, with a wavelength of 1550 nm or 780 nm. The dark count rate includes intrinsic detector dark counts due to perturbations, stray background photons and false counts from electrical noise, while light counts include all of these contributions, as well as the intentional photon-induced counts. Therefore, when needed, the net count rate was computed as $R_{\text{net}} = R_{\text{light}} - R_{\text{dark}}$.



Figure 5.13: Oscilloscope image of the pulse generated by a detection event. The device under test is a 150 nm, 10×10 µm^2 meandered nanowire, for the 2 nm NbN + 3 nm MoSi sample at 1.3 K. The second smaller is peak is likely caused by a reflection in the RF lines, due to non-perfect matching.

5.4.3 Trigger sweep

The first dynamic measurement to characterize our detectors was a trigger sweep. In this measurement, the bias current was fixed slightly below the switching current, and the threshold for the trigger of the counter was varied across a defined range. The measurement was repeated both with and without illumination.

The purpose of this measurement is to determine an adequate discrimination threshold that reliably separates real detector pulses from electrical noise. If the trigger level is set too low, noise fluctuations can easily cross the threshold and be counted as false detection events. If the trigger is too high, some actual SNSPD pulses may not cross the threshold, resulting in lost detection events and a lower actual count rate.

The goal is thus to identify an intermediate threshold region in which the electrical noise contribution is strongly suppressed, while most detector pulses are still counted. In this region, the illuminated count rate should be substantially higher than the dark count rate, and should remain constant for small changes in threshold. The identified threshold value is then used for the subsequent measurements.

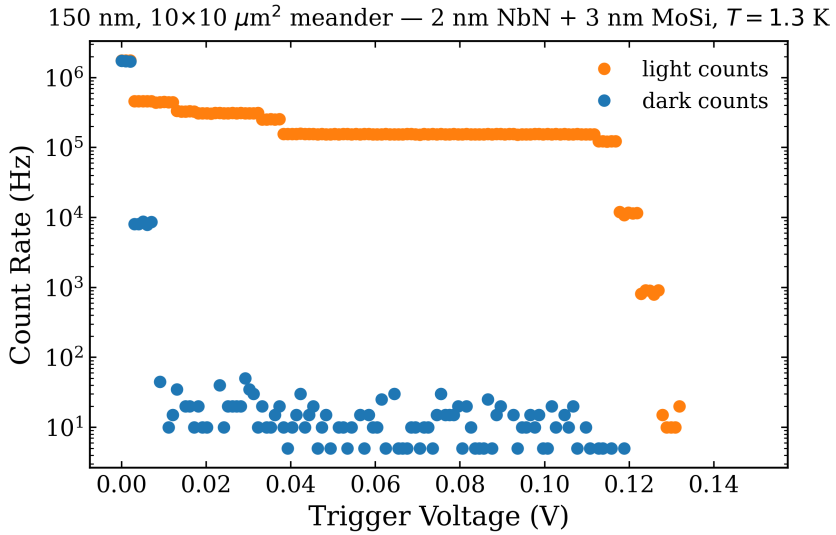


Figure 5.14: Trigger sweep performed on a 150 nm, $10 \times 10\,\mu m^2$ meander nanowire, for the 2 nm NbN + 3 nm MoSi sample at 1.3 K. Light counts represent detection events under illumination, dark counts represent unintentional switching events when the beam is blocked. The step-like behavior at high trigger levels suggests the presence of different type of pulses shape and heights, possibly caused by different microscopic detection dynamics.

The trigger sweep also provides a qualitative diagnostic of the detector response and the quality of the readout signal. A dark count rate that remains high over a broad range of thresholds may indicate excess electrical noise, unstable biasing or light leakage. Conversely, a rapid decrease in the illuminated count rate with increasing threshold may mean that the detector pulses have small or nonuniform amplitude, or that they are attenuated or distorted by the readout chain. If the illuminated and dark count rates are indistinguishable over the entire threshold range, it means the device is not photosensitive under the chosen conditions. The cause may be found in too low or unstable current bias,

insufficient illumination, poor optical coupling or a fault in the readout chain. Additional checks of the optical setup, bias conditions and electrical response can allow to diagnose the cause.

The rapid decrease in the number of detected light counts at high trigger voltages (fig. 5.14) means that the pulse amplitude, determined by the bias current and the readout branch, is lower than the selected threshold. The observed steps are likely related to the experimental acquisition time.

5.4.4 Linearity check

The fabricated nanowires are expected to operate as single-photon detectors, meaning that each absorbed photon can independently trigger a resistive switching event. To verify this, the number of detection events was measured for various intensities of the incident light, thanks to the variable attenuator. In this measurement the other parameters (the bias current and the trigger level) were kept fixed.

If the device really operates as a single-photon detector, the number of counts should be proportional to the incident photon flux, under the correct operating conditions (absence of latching, limited dark counts, proper biasing and trigger level).
Starting from the optical attenuation A expressed in the decibels, the optical power delivered to the devices, referred to the maximum non-attenuated power P_0, is

$$P(A) = P_0 \; 10^{-A/10} \tag{5.13}$$

The photon flux is proportional to this optical power, with a dependence on $10^{-A/10}$. If the SNSPD responds to the single photons, the same holds for the count rate

$$R_{net}(A) = R_0 \; 10^{-A/10} \tag{5.14}$$

Finally, taking the base-10 logarithm yields

$$\log_{10} R_{\text{net}}(A) = \log_{10} R_0 - \frac{A}{10} \tag{5.15}$$

Hence, if we plot on a log scale the measured count rate vs the attenuation applied (in dB), we expect the experimental points to lie on a straight line. This holds for an appropriate regime: at high enough optical power (low attenuation), we may cause the substrate to heat due to the energy deposited, and interfere with the detection process; at too low optical power (high attenuation), the dark counts dominate and we lose the characteristic linear trend, as the detection events are not anymore primarily triggered by photons.

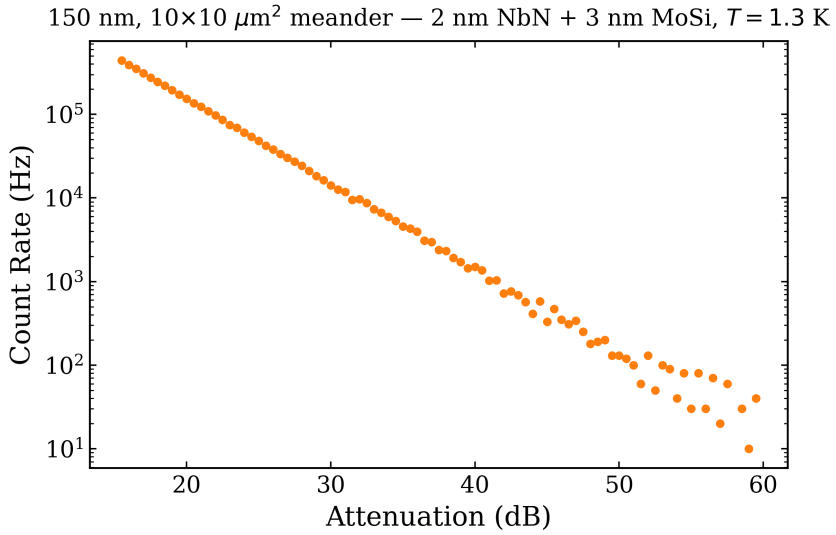


Figure 5.15: Linearity check performed on a 150 nm, 10×10 µm meandered nanowire, for the 2 nm NbN + 3 nm MoSi sample at 1.3 K. The linear slope confirms the single-photon detection events, until the optical power becomes too low and dark counts start to dominate.

5.4.5 Photon Count Rate

The final dynamic measurement was the photon count rate, as a function of the bias current. The optical intensity and the trigger threshold voltage were kept constant in each measurement. For each bias current of the sweep, the count rate was measured both under illumination and blocking the beam. The net count rate, computed as the difference between the number of light and dark counts in the unit of time, is also reported.

This measurement provides information about the bias dependence of the detection efficiency. If the bias current is low, an absorbed photon may cause a weak local perturbation that the nanowire can easily recover from without producing a full resistive transition. As a result, the probability that an absorbed photon produces a detection event is low, and the same holds for the count rate. As the bias current is increased, the nanowire is brought closer to its switching current and the superconducting state becomes weaker, so that a smaller additional perturbation is required to drive the wire resistive. The detection probability and the count rate therefore increase with the bias current.

In the ideal case, the photon count rate, under illuminated conditions, should reach a plateau before the switching current of the nanowire. This corresponds to saturation of the internal detection, meaning that every absorbed photon is converted into a measurable voltage pulse. It is important to remember, however, that while the internal efficiency is maximized, the absolute number of count rates could still be improved by means of fiber coupling or optical absorption.

Ideally, we want our dark counts to be minimum, so that we do not have false counts that can interfere with our measurements. However, in reality, the dark count rate generally increases as we approach the switching current, because we get close to the limit of stability of the superconducting state and small perturbations, such as electrical noise, blackbody radiation coupled fed through the fiber or thermal fluctuations, can cause a resistive

transition.

Measuring the photon count rate allows us to verify whether our detectors are sensitive enough to reach saturation, as well as identifying the optimal operating bias: this generally corresponds to a point at the onset of the plateau (if reached), where the light counts are maximized, but before the dark counts start raising too much.

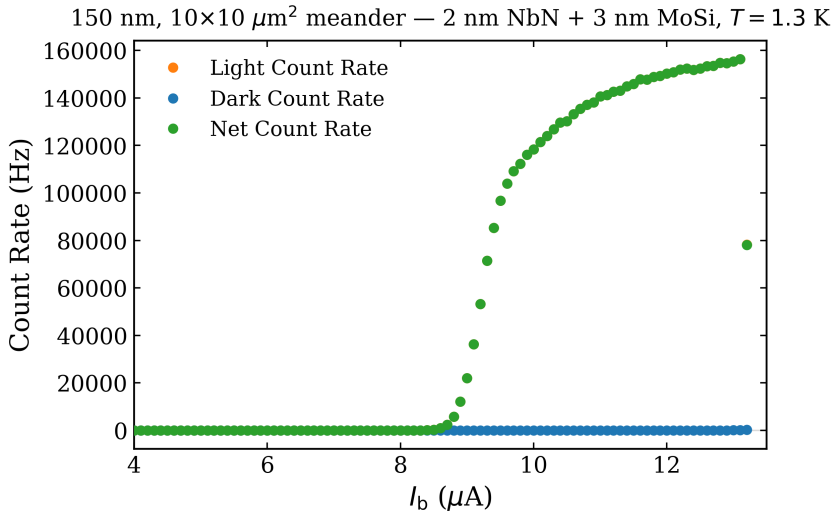


Figure 5.16: Photon count rate measurement performed on a 150 nm, 10×10 µm meandered nanowire, for the 2 nm NbN + 3 nm MoSi sample at 1.3 K. The plateau region corresponds to the saturation of the internal detection efficiency. The tested device proved operation with zero dark counts. Consequently, the light counts are not visible in the plot because completely shadowed by the net count rate.

6 Discussion

This chapter presents the theoretical and experimental results derived from the previous chapters and compares them. The main objective is to determine whether the models developed for our superconducting bilayer truthfully reproduce the trends observed in the fabricated detectors. The comparison focuses on the critical temperature of the bilayer, the switching current for each device shape and its dependence on temperature, the saturation of the internal detection efficiency and the maximum temperature at which the light counts can still be distinguished from dark count events.
In particular, the measurements were performed on several bilayer compositions and device geometries, as described in the previous chapters. Ideally, each bilayer composition would be characterized using the same complete set of device geometries and measurement conditions, such as illumination wavelength and operating temperature. In practice, however, the experimental matrix is not fully populated. A number of devices could not be correctly characterized because of fabrication defects such as discontinuities or constrictions in the nanowires. In a couple of instances, the electrical connections established with the wirebonds failed while closing and pumping the cryostat, preventing us from electrically accessing the device. In some other cases, a device was electrically functional but due to time constraints it was not possible to characterize it over the entire intended range of temperature or illumination wavelength. Moreover, we were limited in the extension of devices we could test by the number of lines available in the cryostat and by the time required by the tool to pump down under vacuum and lower the temperature, at each cooldown.
It is also worth noting that different samples were measured during different cooldowns, for which the background noise, optical alignment, wiring and stability of the cryogenic environment were not necessarily identical.

All of the above limitations are particularly important when comparing detector-level figures of merit such as the switching current and the photon count rates. These quantities depend not only on the intrinsic properties of the bilayer and its composition, but can be heavily affected by the effective geometry produced by the fabrication, the nanowire uniformity, the thermal environment and the readout electronics. As a consequence, the available data does not support a rigorous quantitative ranking of every possible combination of composition and device geometry. To establish statistically robust performance metrics, a larger number of nominally identical devices would need to be tested under the same conditions.

Nevertheless, our measurements are sufficient to reveal general trends across the composition variations. In particular, they make it possible to compare the switching current and critical temperature dependence on the NbN and MoSi thicknesses with the predictions coming from the Usadel equations, and to determine whether intermediate compositions provide a useful compromise between the properties of the two constituent materials. The purpose of this chapter is thus not to claim a fully optimized detector design, but rather to identify the physical trends supported by theoretical predictions and measured data.

6.1 Critical temperature as function of composition

The critical temperature is the most direct quantity we can measure to test the theoretical description of the NbN/MoSi bilayer. Unlike detector-level figures of merit, T_c does not depend on the transferred pattern, the optical alignment or the electronic readout chain. It is therefore a useful first test to verify whether the superconducting proximity effect in the bilayer is captured by our model.

The theoretical calculation was performed in two stages. First, the thickness dependence of the critical temperature for each material was modeled using the stretched exponential fit described in section 2.1.4. Then, the fitted $T_c(d)$ that models the thickness-dependent critical temperature suppression was plugged into the Usadel solver for the respective combinations of NbN and MoSi thicknesses. Solving the coupled equations for the two layers gives the T_c of the combined bilayer, which is not only an average of the starting points, but results from the proximity-induced coupling of the superconducting correlations across the interface.

Figure 6.1 compares the predicted critical temperature with the experimentally measured values for all the different compositions. The remarkable agreement between the theoretical prediction and the experimental values suggests that the proximity-effect model captures well the dominant physics controlling the transition temperature. In particular, once the single-material T_c was modeled with the stretched exponential fit, the derived bilayer critical temperatures align almost perfectly with our experimental values.
The only sample for which we can observe a significant discrepancy is the one constituted of 3 nm of NbN and 2 nm of MoSi. However, the cause of this unexpected result is likely in the experimental procedure, rather than in an incorrect modeling of the bilayer physics. If we isolate the experimental points, we can already see that this particular combination has a reduced T_c that does not align with the rest of the measured values. Different explanations could be proposed to justify this result: the T_c measurement was conducted on an identical dedicated sample (different from the one on which the devices were built), which may have presented some defects; structural defects could have also been introduced by us during the cleaving of the sample to prepare it for the MPMS measurement; as it was not possible to easily and reliably check the actual deposited thickness, we should also not rule out the possibility that this sample had a thickness that differed from the

nominal value. Nevertheless, the devices built with the aforementioned composition, on the twin sample deposited at the same time, seemed to work as expected.
A slight thickness variation, over a 1 nm layer, can easily become relevant difference. The fitted single-layer T_c functions and the bilayer prediction therefore both inherit uncertainty from the deposition calibration and from the characterization of the films. It would be desirable to both repeat the MPMS critical temperature measurements, and to test new samples with the same nominal thickness, to be able to assign some error bars to our measurements and test the reproducibility of our results.

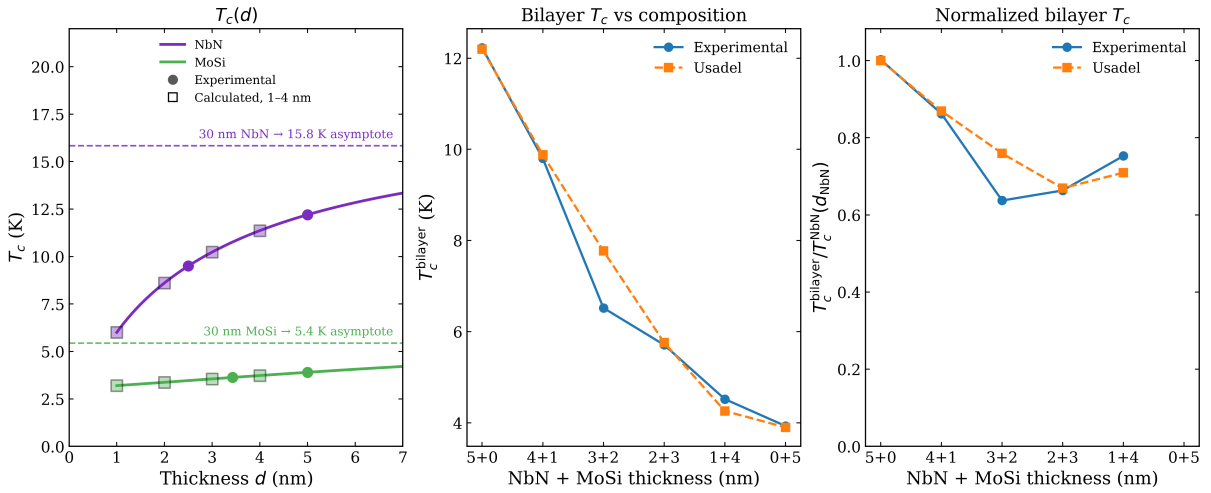


Figure 6.1: Characterization of the critical temperature as a function of the thickness of the material and composition of the bilayers. (a) Thickness dependence of the critical temperature $T_c(d)$ for pure NbN and MoSi. The stretched exponential fit represents a phenomenological modeling of the observed critical temperature suppression at low thicknesses. The solid round points represent the experimental values, while the square points are the values extracted from the fit and used as input for the material properties in the Usadel equation. (b) T_c for the different bilayers. The blue dots show the experimentally measured values, while the orange squares are the critical temperatures obtained from the Usadel solver while applying the stretched exponential fit. (c) Critical temperature normalized to that of the NbN present in that composition. The values used for normalization are extracted from the stretched exponential fit.

It is instructive to examine the bilayer critical temperature normalized to that of the NbN layer alone, evaluated at the same thickness as the one employed in the corresponding bilayer (figure 6.1c). Since the critical temperature of each single material depends on its thickness, every composition is characterized by a different pair of reference values for NbN and MoSi, and the normalization is therefore performed with respect to the NbN critical temperature specific to that bilayer. Both the theoretical predictions and the experimental data exhibit a non-monotonic trend: the normalized ratio is highest for strongly unbalanced compositions dominated by either NbN or MoSi, and reaches its minimum for balanced compositions. This behavior can be rationalized by considering the two limits separately. For NbN-dominated bilayers, the thin MoSi layer only weakly perturbs the superconducting properties of the thicker NbN film, so the bilayer critical temperature remains close to that of the reference NbN layer and the normalized ratio stays high. For MoSi-dominated bilayers, the situation is different: the NbN layer is now very thin and its own critical temperature is already strongly suppressed by the reduced

thickness, whereas the MoSi critical temperature is only mildly reduced. In this regime the MoSi does suppress the bilayer critical temperature substantially, but the normalization is performed with respect to an already low NbN value, so the resulting ratio is again comparatively high. The minimum observed for balanced compositions thus reflects the combination of a still relatively high NbN reference temperature with a sizeable suppression induced by the MoSi layer.

6.2 Switching current as function of composition

The next quantity considered is the switching current I_{sw}. Its absolute value does not by itself determine the achievable internal detection efficiency, which depends on the sensitivity of the detection mechanism to the bias current rather than on the magnitude of I_{sw}. Nevertheless, a higher switching current is desirable from a practical point of view, as it provides a wider range of accessible bias currents, allowing the operating point to be tuned more finely, and it increases the amplitude of the output voltage pulse, thus improving the signal-to-noise ratio at the readout stage. In addition, a larger I_{sw} leaves more margin with respect to fluctuations and drifts of the bias.
The numerical value of the switching current highly depends on the specific geometry of the device. In particular, wider nanowires are able to carry a larger bias current before switching to the resistive state, due to the increased cross-section. At the same time, longer nanowires increase the likelihood of constrictions generating during the fabrication, thus limiting the current that can be sustained and causing premature switching.

Figure 6.2 shows the switching current density for the different bilayer compositions coming from the Usadel equations, as well as the experimentally measured values. The latter are normalized according to the nominal thickness and width of the devices. The Usadel predictions are obtained for a temperature of 1.3 K, aligned with our characterization conditions. The experimental data set misses some combinations of device geometry and compositions, for the considerations mentioned above.
While we should be cautious about extracting quantitative measurements from these plots, it is evident that the measured experimental trend is in accordance with the results coming from the Usadel equations. In particular, the switching current increases with the NbN content and the relative change is higher the less MoSi we have in the stack.
The trend is most visible for the 150 nm-wide nanowires, which proved to have the most reliable fabrication procedure.

While the experimental results align well with the theory, all of the devices showed a greatly suppressed switching current when compared with the predictions. The ratio between the experimentally measured value and the theoretical limit represented by the depairing current expresses the constriction factor C, and describes how the fabrication nonidealities affect the devices performances. The switching current is particularly affected because it is directly controlled by the weakest segment of the full active area. This

suppression is particularly significant for the sample built on 5 nm of NbN. This is also the sample for which the fabrication was problematic (see section 4.3.1) and that was deposited after the sputtering system was brought to atmospheric pressure and had its target swapped, so we are less confident on the exactness of its thickness, compared to the previous stacks. A more complete quantitative study would involve measuring several nominally identical devices for each combination of composition and geometry, and extracting the switching current density, to average the geometry- and fabrication-dependent variations and isolate the actual composition dependence.

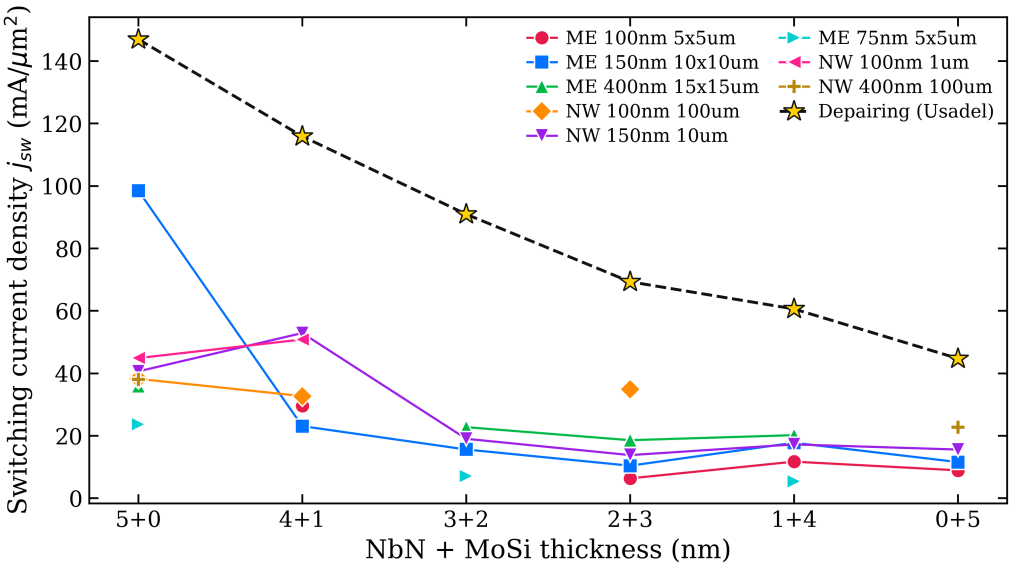


Figure 6.2: Switching current density of the fabricated devices, compared with the Usadel prediction. For each device, the switching current was measured and then normalized according to the nominal thickness and width of the cross-section. ME indicates meander nanowires, NW indicates straight nanowires.

It should be emphasized that the depairing current used here is a theoretical estimate calculated in the Usadel framework from measured material parameters and an assumed superconducting model, rather than an experimentally determined value. An experimental estimate of the depairing current could be obtained using a microwave resonator containing the nanowire as an inductive element. As the bias current approached the depairing limit, the nanowire's kinetic inductance increases, shifting the resonator frequency. Fitting this current-dependent shift allows I_{dep} to be derived experimentally [134].

Figure 6.3 shows the constriction factor for each fabricated device. This parameter is computed as the ratio between the measured switching current I_{sw} and the ideal depairing current I_{dep}. Equivalently, in the present work we computed this quantity from the current density obtained by dividing the measured switching current by the nominal cross section area, and the depairing current density from the Usadel prediction. Wider devices (400 nm and 150 nm) show larger constriction factors, as with their increased cross section they are less sensitive to small width variation coming from fabrication defects. At the same time, longer nanowires are more prone to constrictions because of their increased length. The absence of a clear trend for different compositions allows us to attribute the performance difference to the bilayer composition, rather than the particular fabrication results.

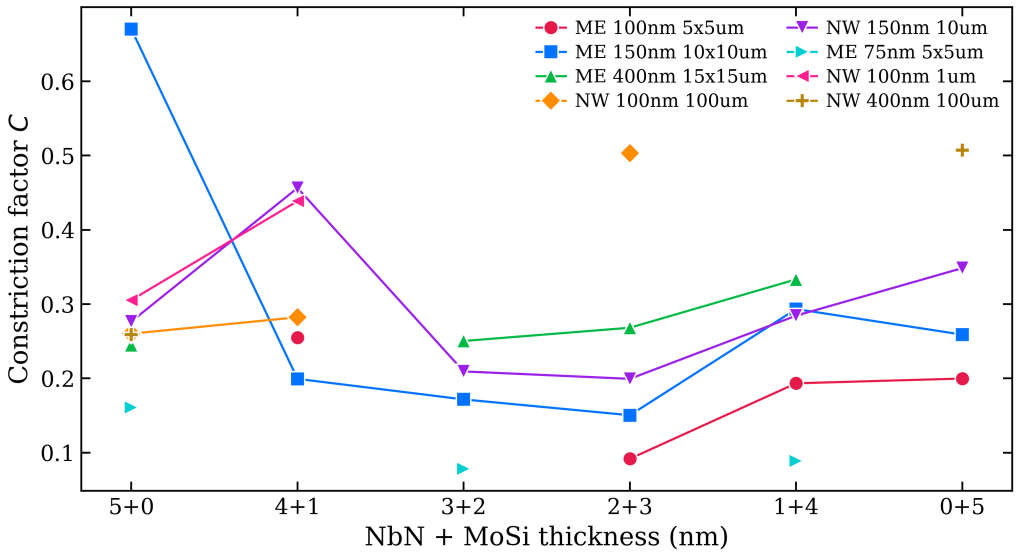


Figure 6.3: Constriction factor for the different geometries and compositions of the fabricated devices. The lack of a clear trend allows us to attribute the performance difference to the bilayer composition, rather than the particular fabrication results.

6.3 Temperature dependence of switching and retrapping currents

The temperature dependence of the current-voltage characteristics of our nanowires provides an additional comparison between the theoretical modeling and the behavior of the fabricated devices. In these measurements, the bias current was increased until the detectors (not illuminated) switched from the superconducting state to the resistive state, and then decreased until they returned to the superconducting state with zero resistance. The upwards transition defines the switching current I_{sw}, while the downward transition defined the retrapping current I_{r}.

The experimental results reveal two distinct behaviors over the measured temperature interval. The switching current decreased approximately linearly with the chamber temperature, while the retrapping current remained constant.

The reduction of I_{sw} with temperature is the expected consequence of the thermal energy supplied to the system, which progressively weakens superconductivity. As the temperature increases, both the superconducting energy gap and the condensation energy are reduced, so the nanowire can sustain a smaller bias current before the superconducting state becomes unstable and switching occurs. The approximately linear dependence observed here should be regarded as an empirical description valid over the measured temperature range: the full theoretical dependence, illustrated by the depairing boundary in figure 2.5, is not expected to be strictly linear, but it is well approximated by a linear behavior at the intermediate temperatures explored in our measurements.

The retrapping current has instead a different physical meaning. Once the device has switched, it remains in the resistive state due to Joule effect continuously injecting energy

into the nanowire. The device returns to the superconducting state only when the bias current is reduced sufficiently for the resistive region to cool and collapse back into the condensate state. The retrapping current is therefore influenced by electrothermal stability and heat removal to the substrate. The only effect of the increase in temperature is to anticipate the limit of instability.

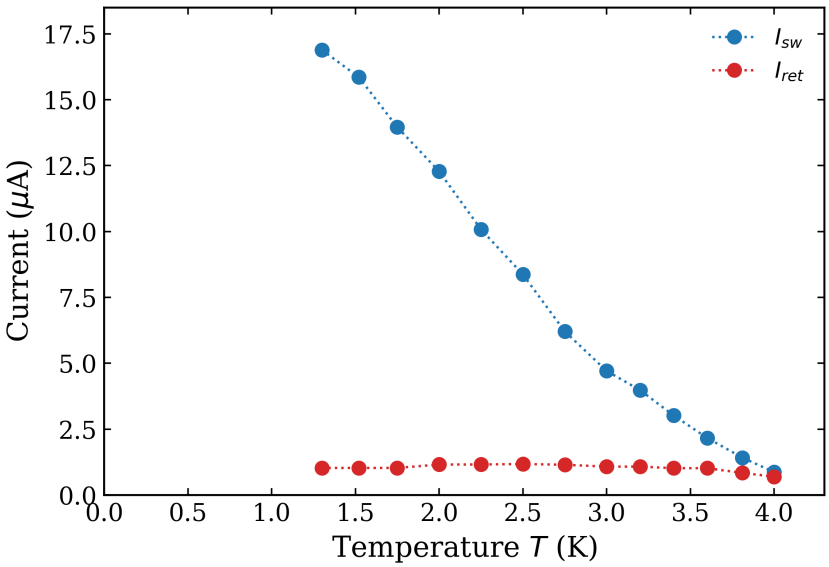


Figure 6.4: Switching and retrapping currents as function of temperature, measured for a 150 nm-wide meandered nanowire, with a 10 µm×10 µm active area, built on a 1 nm NbN + 4 nm MoSi bilayer.

6.4 Photon sensitivity in the kinetic equations

The coupled kinetic equations introduced in section 2.2 were solved for the complete set of 5 nm-thick films, ranging from homogeneous NbN to homogeneous MoSi through the usual intermediate bilayer compositions. All simulations were performed considering a bath temperature $T_{\mathrm{bath}} = 1.3\,\mathrm{K}$, to replicate the experimental conditions. Similarly, excitation wavelengths of 780 nm and 1550 nm were considered.

6.4.1 Debye phonon density of states

The phonon spectrum entering the kinetic equation was described using the Debye approximation. For the homogeneous reference films, Debye temperatures of $\Theta_{\mathrm{D}}^{\mathrm{NbN}} = 650\,\mathrm{K}$ [135] and $\Theta_{\mathrm{D}}^{\mathrm{MoSi}} = 330\,\mathrm{K}$ were used. For the intermediate bilayers, an effective Debye temperature was obtained from a thickness-weighted geometric mean of the properties of the parent materials

$$\Theta_{\mathrm{D}}^{\mathrm{eff}} = \left(\Theta_{\mathrm{D}}^{\mathrm{NbN}}\right)^{d_{\mathrm{NbN}}/d_{\mathrm{tot}}} \left(\Theta_{\mathrm{D}}^{\mathrm{MoSi}}\right)^{d_{\mathrm{MoSi}}/d_{\mathrm{tot}}} \tag{6.1}$$

where $d_{\mathrm{tot}} = d_{\mathrm{NbN}} + d_{\mathrm{MoSi}} = 5\,\mathrm{nm}$ is the total thickness of the bilayers.

Figure 6.5 compares the Debye spectra for the different composition. As the MoSi contribution increases, the effective Debye cutoff shifts to lower phonon energies.

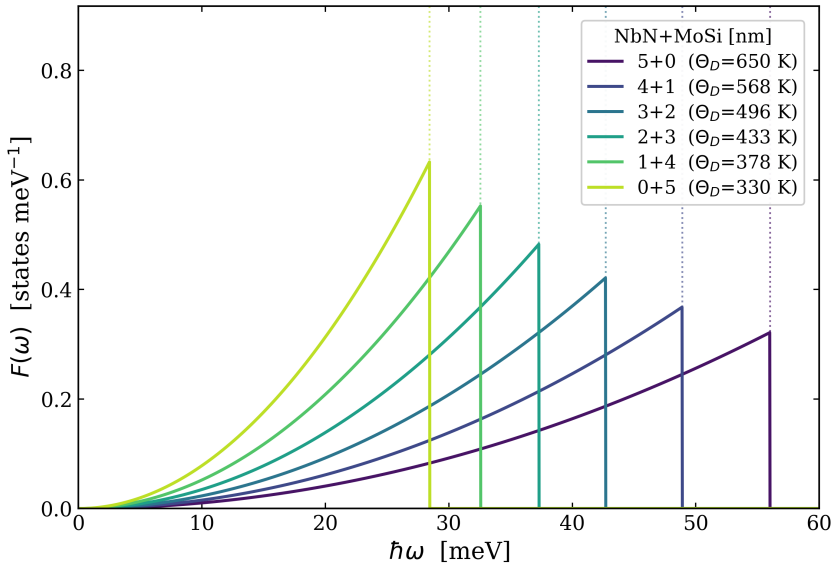


Figure 6.5: Debye phonon density of states $F(\omega)$ computed for each of the bilayers. The cutoff is imposed by the material-dependent Debye temperature Θ_{D}.

A proximitized bilayer is generally not equivalent to a homogeneous alloy, and as discussed in sec. 2.1 the properties are also not perfectly constant across the stack. Moreover, interfaces, disorder and strain may alter the actual phonon modes. However, in the absence of composition-specific measurements of the phonon density of states, the geometric interpolation applied to the Debye model allows a consistent method of connecting the two experimentally relevant endpoint materials.

6.4.2 Gap suppression

Figure 6.6 shows the calculated time evolution of the superconducting gap and the exponential fit for the characteristic time. For both excitation wavelengths (0.78 µm and 1.55 µm) and for all investigated compositions, the gap is driven to zero within the simulated time interval of 10 ps. Thus, under the assumed energy deposition conditions, both phonon energies are in principle sufficient to produce complete local suppression of superconductivity, throughout the full composition series.

The endpoint of the dynamics is therefore the same for all samples: complete gap suppression. Nevertheless, the trajectories toward this state depend on both composition and photon energy. In NbN-rich films, the gap starts from a considerably larger equilibrium value, and decreases steeply after phonon absorption. As the MoSi contribution is increased, the initial gap becomes smaller, reflecting the lower T_{c} of the proximitized bilayer. The dynamics of the suppression show a slower suppression for the MoSi-rich layers, leading to a larger τ_{DC} parameter. The increase is monotonic up to the sample containing 1 nm of NbN, after which the characteristic time seems to saturate to the one of MoSi, meaning that its gap dynamics have become predominant.

The slower suppression shown by MoSi does not contradict the greater photon sensitivity generally associated with this material. Photon sensitivity is determined by how easily the

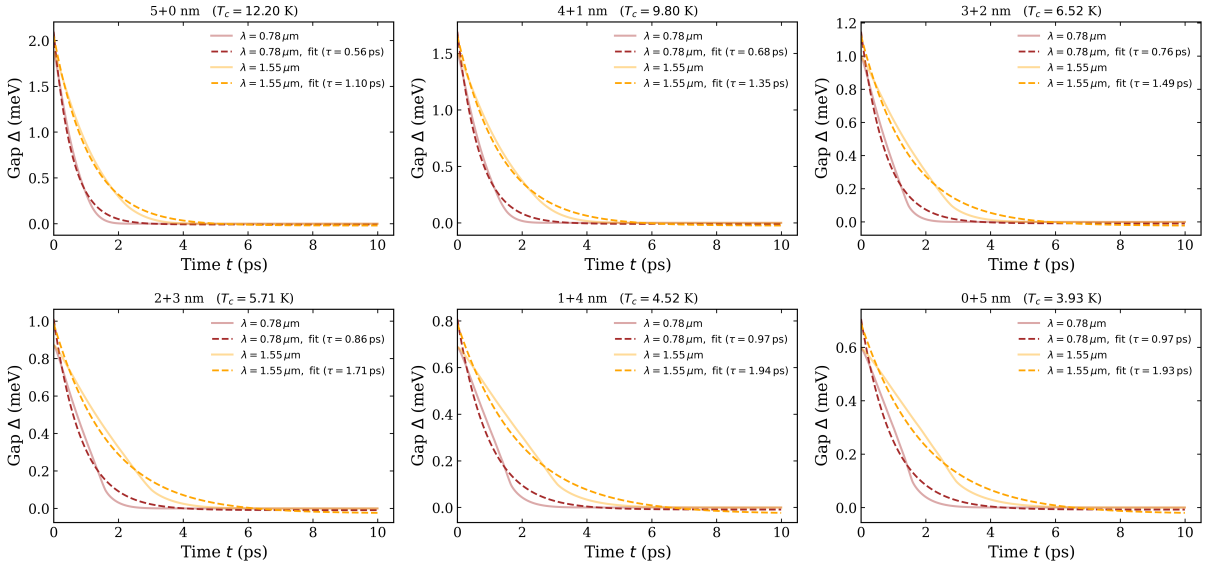


Figure 6.6: Gap suppression time evolution and exponential fit, for all the bilayers investigated. Both the 780 nm and 1550 nm wavelengths are able to completely suppress the superconducting state, in each of the simulated samples.

deposited energy exceeds the relevant superconducting energy scale, while τ_{DC} describes the temporal rate at which the gap approaches its suppressed value. A larger τ_{DC} does not necessarily imply poor sensitivity if the lower gap and lower transition temperature allow the photon perturbation to drive the system much farther above its superconducting threshold.

As expected, the dynamics always proved to be faster for the 780 nm photon, as it injects into the system an energy twice as high as the one corresponding to a 1550 nm wavelength. The ratio between the fitted time constants at 1550 nm and 780 nm is close to two for all the compositions. While this should not be interpreted as a universal proportionality, since the kinetic equations are nonlinear and include coupled electron and phonon dynamics, it shows that the fitted suppression time responds consistently to different deposited energies in the present model.

Within the assumptions of the model, the 1550 nm excitation is also found to drive the gap to zero in every simulated 5 nm film, so that the difference between the two wavelengths and between the various compositions lies in how rapidly the suppression evolves rather than in whether it is reached. This observation should however be interpreted with caution. The present calculation is a zero-dimensional model, in which the deposited energy is assumed to be uniformly distributed over the simulated volume and spatial diffusion of the quasiparticles and phonons is not taken into account. Since diffusion competes with the local growth of the perturbation, the occurrence of complete suppression in the simulation cannot be taken as a proof that a single photon of either wavelength necessarily produces a full local breakdown of superconductivity in the real devices. The results are therefore best regarded as indicating the relative trend of the suppression dynamics across compositions and photon energies, rather than as a quantitative statement on the absolute detectability of a given wavelength.

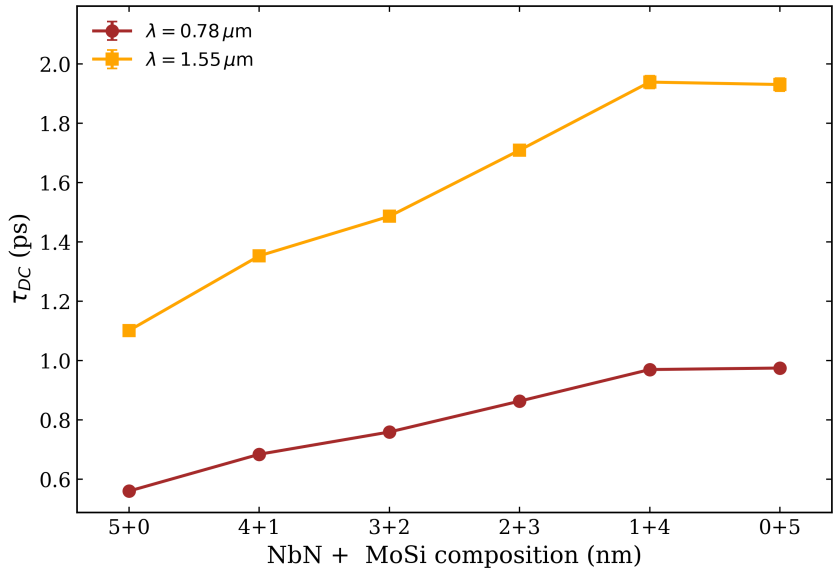


Figure 6.7: Fitted value of the downconversion time constant τ_{DC} for the two simulated wavelengths, varying the bilayer composition.

6.4.3 Effective electron and phonon temperatures

A measure of the intensity of the photon-induced perturbation is provided by the effective electron and phonon temperatures (section 2.2.7) In particular, $T_{\mathrm{eff}}/T_{\mathrm{c}}$ and $T_{\mathrm{ph}}/T_{\mathrm{c}}$ highlight how strongly each bilayer composition is perturbed with respect to its intrinsic energy scale.

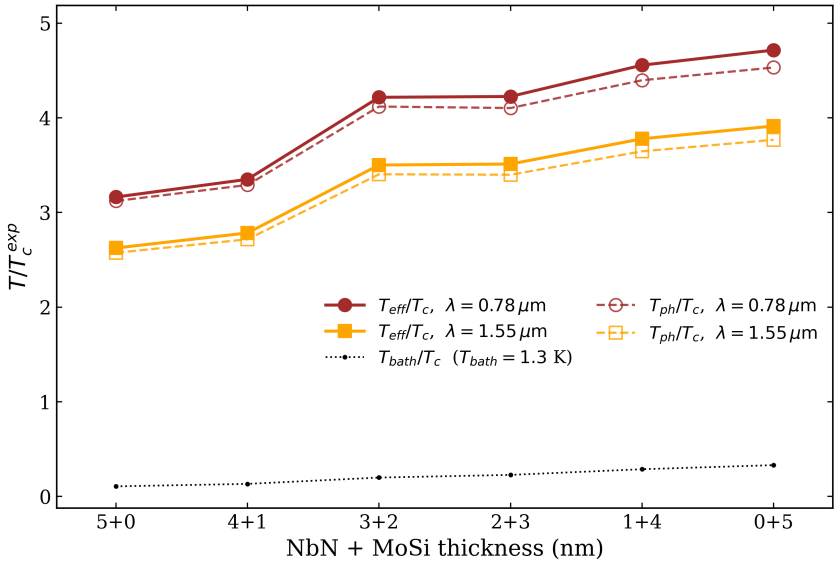


Figure 6.8: Electronic and phononic effective temperature for all the bilayers following the perturbation caused by a 780 nm and a 1550 nm photon, computed from the energy equivalence to the equilibrium distribution.

For both wavelengths, the normalized effective temperatures increase as the MoSi fraction is increased, reproducing the higher photon-sensitivity provided by this material. The electron and phonon effective temperatures are systematically higher for the 780 nm excitation, as expected from the larger photon energy. The physical meaning of this trend

is that the photon drives the MoSi-rich films farther above their own superconducting transition temperatures. Although NbN-rich samples are shown to reach a higher absolute electron and phonon temperature, their substantially higher T_c means that this temperature increase corresponds to a smaller relative perturbation.

In particular, we can notice that a pronounced change in normalized temperature occurs between the samples containing 1 nm and 2 nm of MoSi, while the farther increase for higher MoSi compositions is reduced. This result indicates that a largely MoSi-like thermal response is already established in the central part of the composition series. The central bilayers combinations therefore occupy an interesting region in which the photon response is already close to the sensitive MoSi-rich limit, while a substantial NbN fraction allows to enhance the critical temperature.

6.5 Saturation of the photon count rates

A central objective when designing SNSPDs is to achieve a high internal detection efficiency, close to unity. This means that all of the photons that are absorbed in the nanowire lead to a detection event. Experimentally, when looking at a photon count rate curve, in which we sweep the bias current and monitor the light and dark counts, this regime is indicated by the flat plateau at high bias currents. Once this region is reached, increasing the bias current causes little additional increase in the number of photons detected. Ideally, we would like our devices to have a high photon sensitivity and a large saturation plateau. This means we can detect the incoming photons with high efficiency while biasing the detector at a lower DC current, thus reducing the probability of unintentional dark count events.

The degree to which our devices saturate was quantified using the parameter σ, defined as

$$\sigma = \frac{I_{\mathrm{sw}} - I_{50\%}}{I_{50\%}} \tag{6.2}$$

where I_{sw} is the switching current at which the devices becomes resistive, and $I_{50\%}$ is the bias current at which the photon count rate equals half the maximum value reached at high bias current. A larger value of σ thus corresponds to a more pronounced or wider plateau before the switching current is reached.
However, many of our devices were not saturating at 1550 nm wavelength, meaning we could not experimentally observe the saturation plateau. To be able to extract the same figure of merit σ, we decided to fit the experimental photon count curves with an hyperbolic tangent function

$$y = (1 + \tanh[b(x - I_{50\%})])(dx + f), \qquad I_{50\%} = -\frac{c}{b} \tag{6.3}$$

The linear function multiplying the hyperbolic tangent allows us to model the residual linear slope empirically observed in some devices. A possible explanation of this

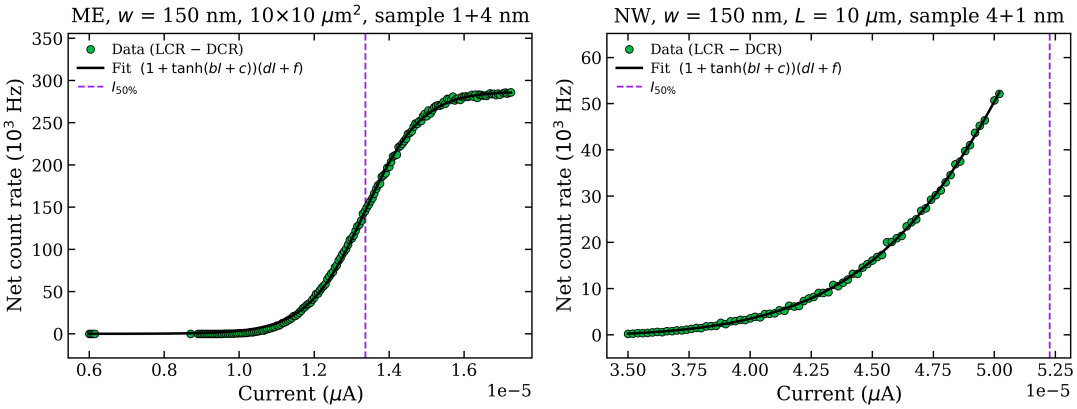


Figure 6.9: Hyperbolic tangent fits of the measured PCR curves, both for saturating and non-saturating devices. On the left, the result obtained for a 150 nm wide, $10 \times 10 \mu m^2$ meandered nanowire, on the 1 nm+4 nm sample, for which a saturation plateau is visible. On the right, the result obtained for a 150 nm wide, 10μm long straight nanowire, on the 4 nm+1 nm sample. This device did not reach internal saturation efficiency, and the experimental points are all below the fitted $I_{50\%}$ threshold.

phenomenon is a spatial nonuniformity of the detection threshold, typically arising from geometric imperfections, or possibly in the case of our bilayer from material variations. As a consequence, the plateau would represent the saturation of the most sensitive section of the nanowire. As the bias current rises, the detection probability for less sensitive regions keeps increasing [136], leading to the phenomenological model proposed. The value of I_{sw} is determined experimentally as the value of bias current that caused a resistive transition. The value of $I_{50\%}$ is instead extracted from the fitting function. From these two parameters, σ is computed for each detector. While this allows for a more complete analysis, including the devices that don't reach the saturation plateau, the results can sometimes be affected by imprecisions in the fitting function. In fig. 6.10, markers with a black outline correspond to devices that were not saturating

Figure 6.10 shows the value of the parameter σ extracted from the fit on our experimental photon count curves. The markers with a black outline represent the devices for which we could not reach the saturation plateau. This distinction is meant as an admonition that the fit on those curves suffers from a higher uncertainty. Consequently, discretion is required when interpreting the results of this plot.

From our analysis the best-performing devices, in terms of saturation of internal efficiency, are the ones built on the combination of 2 nm of NbN and 3 nm of MoSi. In principle, we would generally expect higher saturation efficiency from bilayers containing a dominant fraction of MoSi, as this material is characterized by a higher photon sensitivity. However, the count rate measurements are taken at the finite temperature of 1.3 K. This value corresponds to roughly 30% of the T_{c} of MoSi, meaning that the suppression of the superconducting state of this material starts to be non-negligible. The results seem to confirm that the combination in our bilayers of the two materials allows to retain the high sensitivity of MoSi, while combining it with the higher operating temperatures that are made possible by the higher-T_{c} NbN.

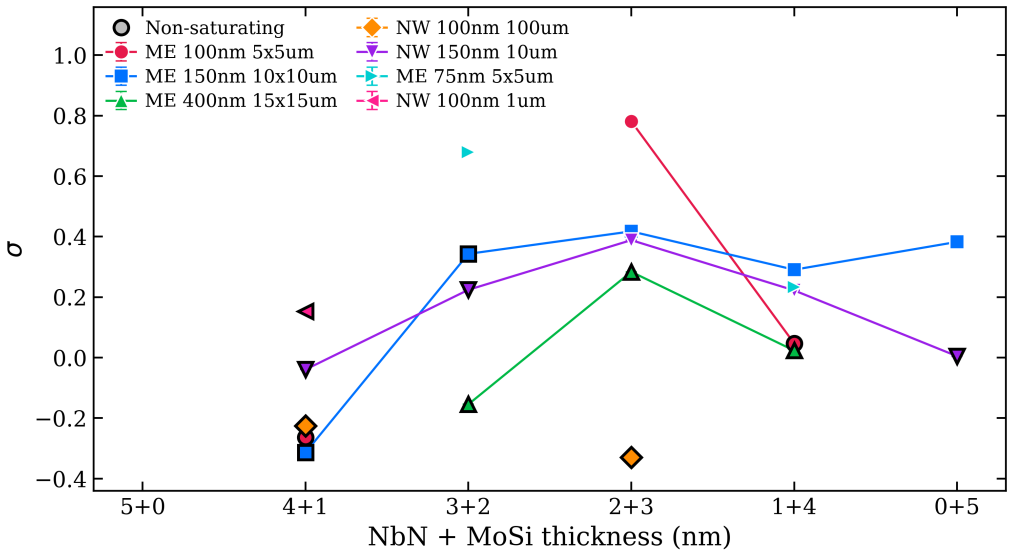


Figure 6.10: Saturation coefficient σ for the different device shapes and bilayer compositions. The values were extracted from the fits of the PCR curves obtained at a temperature of 1.3 K under 1550 nm illumination. No data are available for the 5 nm NbN sample because the devices could not produce detection events at 1550 nm under the characterization conditions. The points with a black outline indicate the devices for which we did not observe the onset of the saturation plateau, and that consequently have a larger uncertainty in the fitted parameters.

6.6 Maximum operating temperature

The final comparison regards the maximum temperature at which devices from each composition combination retained photon sensitivity. This maximum operating temperature is indicated as $T_{\mathrm{op,max}}$. For this analysis, the limit was defined as the highest temperature at which the photon count rate under illumination could still be distinguished from the dark count rate. The characterization was carried out through a coarse temperature sweep with 0.5 K steps. This temperature was then normalized by the measured critical temperature of the corresponding bilayer, in order to be able to compare how close each detector operates to its superconducting transition.

The measurements were performed on the 150 nm-wide, 10 µm × 10 µm meandered nanowire, as this device geometry proved to be the more reliable across the different sample compositions. The only exception is for the 5 nm NbN sample, on which the desired device showed poor performance even at lower temperatures. A 75 nm meandered nanowire is reported instead.

The wavelength employed at these higher temperatures was 780 nm. Photons at this wavelength carry more energy than the 1550 nm normally used at 1.3 K, allowing to improve the sensitivity of our detectors.

The general trend observed is that a higher composition of MoSi increases the photon sensitivity also at higher temperatures. However, the normalized results do not show a monotonic increase. Instead, the largest normalized operating temperature is observed for the detector built on 1 nm of NbN and 4 nm of MoSi, which shows almost complete saturation of the internal detection efficiency at about 79% of its critical temperature.

Table 6.1: Maximum operating temperature for different compositions

Composition (NbN + MoSi) nm	T_c (K)	$T_{op,max}$ (K)	$T_{op,max}/T_c$	Measurement outcome
0 + 5	3.93	2.0	0.51	Saturating PCR at 780 nm
1 + 4	4.52	3.4	0.75	Nearly saturating at 780 nm
2 + 3	5.71	4.0	0.70	Nearly saturating at 780 nm
3 + 2	6.52	3.0	0.46	Detectable but not saturating at 780 nm; saturating up to 2.5 K
4 + 1	9.8	2.5	0.26	Detectable at 780 nm, but not saturating
5 + 0	12.23	2.5	0.20	Detectable at 780 nm, but not saturating; different geometry

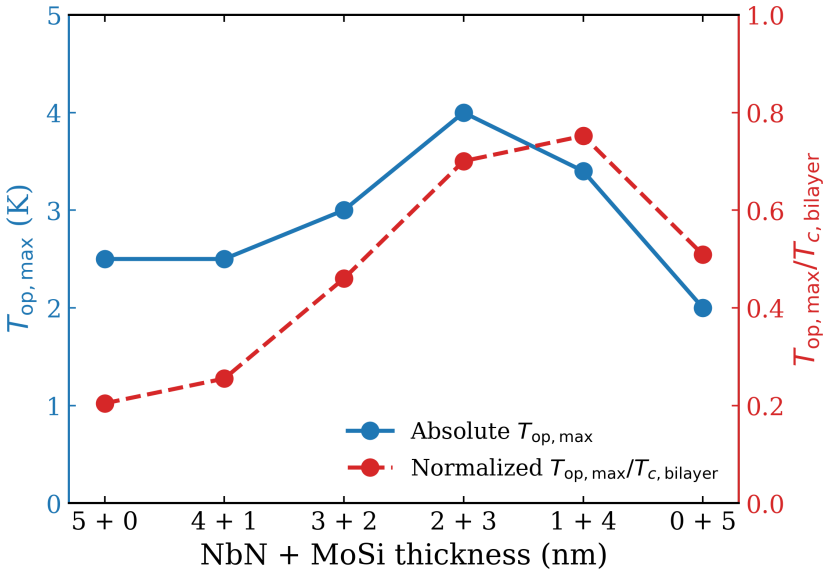


Figure 6.11: Absolute maximum operating temperature for each device composition, and the corresponding value normalized to the critical temperature of the corresponding bilayer.

Another particularly interesting composition is the 2 nm of NbN + 3 nm of MoSi, which shows good sensitivity at an higher absolute temperature of 4.0 K. This is the highest absolute operating temperature among the measured devices, and it is attractive because it is close to the limit of 4.2 K imposed by liquid helium. Being able to surpass this threshold would mean highly relaxing the constraints on the cryogenic system required to operate the detectors.

These results demonstrate that a higher superconducting critical temperature does not necessarily lead to operation at a higher temperature. Increasing the NbN content strengthens the superconductivity and raises the switching-current scale, but it can also make the superconducting state more difficult to perturb by the finite energy deposited by a photon. Conversely, an intermediate bilayer has a lower superconducting energy scale and can remain sensitive to photon-induced perturbations over a larger temperature range.

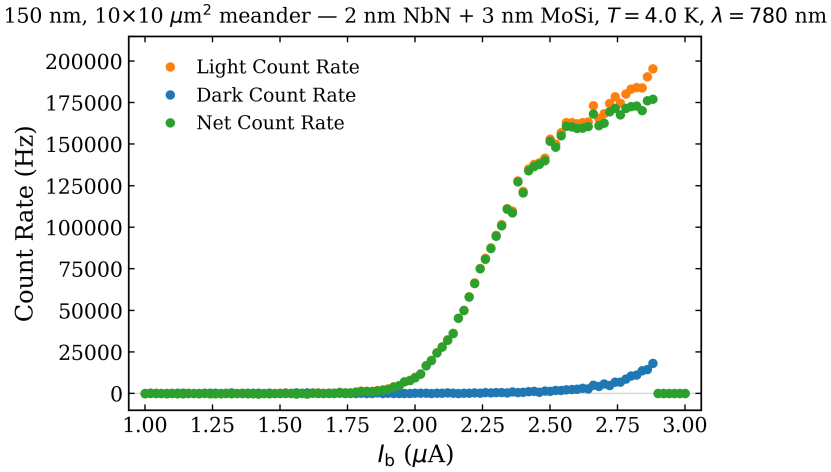


Figure 6.12: Photon count rate obtained for a 150 nm-wide meandered nanowire, on the 2 nm NbN + 3 nm MoSi sample, at a temperature of 4.0 K, illuminated with a 780 nm continuous-wave laser.

7 Conclusions and future work

In this thesis, the proximity effect in NbN/MoSi superconducting bilayers was investigated as a possible technique to engineer the properties of superconducting nanowire single-photon detectors. The founding idea was to provide an additional design parameter to be able to precisely tune the detector properties beyond the choice of a single superconducting material. By varying the relative thickness of NbN and MoSi, the superconducting and photon-detection properties of the resulting proximitized bilayer can be modified. The work combined theoretical modeling of the bilayer with its experimental fabrication and characterization, providing a practical framework to connect the composition design of the hybrid material to the effective detector properties.

The experimental results demonstrate that modifying the bilayer composition produced systematic changes in the superconducting properties of the devices. In particular, increasing the NbN contribution results in a higher critical temperature and a higher switching-current scale, while increasing the MoSi contribution enhances the photon sensitivity. These trends reflect the intrinsic properties of the two constituent materials, with the expected mediation of the proximity coupling between them. The comparison with the Usadel model, together with the heuristic stretched-exponential fit to account for the thickness dependence, showed good agreement in the prediction of the critical temperature and switching current across the investigated compositions. This supports the use of the model as a framework to verify the relevant physical trends of the superconducting equilibrium properties.

The kinetic equation analysis provided a complementary perspective on the photon sensitivity of the different compositions. The calculated response predicted the bilayer sensitivity to the employed wavelengths, showing that MoSi-rich compositions are more strongly perturbed by photon absorption, while NbN increases the superconducting energy scale and critical temperature. Interestingly, balanced compositions already exhibit a response skewed towards the MoSi sensitive regime. This identifies intermediate bilayers as a particularly interesting region of the parameter space, benefiting from the high photon sensitivity of MoSi while retaining the higher critical temperature provided by NbN.

Among the investigated combinations, the 2 nm NbN + 3 nm MoSi emerged as a particularly promising compromise. At 1.3 K, this composition showed the highest saturation margin for the internal detection efficiency. At the same time, its critical temperature of 5.71 K is substantially higher than that of the reference 5 nm MoSi reference. More importantly, the 150 nm meander nanowire built on this sample maintained photon sensitivity up

to 4.0 K under 780 nm illumination and showed nearly saturated PCR at this temperature. This was the highest absolute operating temperature observed among the investigated devices, placing the detector very close to the desirable 4.2 K threshold represented by classical liquid-helium cooling.

It is also worth mentioning that this device exhibited a constriction factor comparable to those of the other investigated devices, supporting the interpretation that its promising performance originates from the favorable bilayer composition rather than from an exceptionally favorable fabrication outcome.

An additional aspect that makes this result promising is the relatively large nanowire width used for the devices, nominally at 150 nm. The successful observation of saturation at relatively high temperature for these dimensions is encouraging because it indicates that good photon-detection behavior does not necessarily require extremely narrow nanowires. This is relevant for a fabrication perspective, as relaxing the requirement for very small feature sizes can make the geometry less restrictive and, more importantly, improve the reliability and reproducibility of the fabrication process. Although the present results are not sufficient to establish a rigorous relationship between nanowire width and saturation, the results obtained and the comparison with current state of the art suggest that it could be possible to obtain saturation of the internal detection efficiency for even higher operating temperatures, by resorting to smaller feature sizes.

These results should nevertheless not be interpreted as establishing the 2 nm NbN + 3 nm Mosi sample as an absolute optimum. The experimental dataset is limited by the number of successfully fabricated devices, differences in device geometry fabrication defects and measurement conditions. In particular, the experimental matrix was not sufficiently complete to provide a statistically rigorous comparison of every composition and geometry. The results therefore support the identification of promising regions in the composition space, rather than a definitive global optimization. The 1 nm NbN + 4 nm MoSi sample, for instance, could be operated at a higher fraction of its critical temperature than the 2 nm NbN + 3 nm MoSi. Hence, the composition maximizing the normalized operating temperature does not necessarily coincide with the one providing the best low-temperature saturation or the highest absolute operating temperature.

The main outcome of this work is therefore the development of a framework for studying and engineering proximitized superconducting bilayers for photon detection. By combining the Usadel description of the equilibrium superconducting properties with kinetic equation modeling of the photon-induced nonequilibrium response, and by comparing these predictions with the performances of the experimentally fabricated devices, a methodology has been established to investigate how the bilayer composition propagates into detector performance, highlighting the design space that leads to the most promising detectors. The results indicate that the proximity effect can provide a useful additional degree of freedom for balancing properties that are otherwise difficult to optimize simultaneously due to material-imposed tradeoffs.

7.1 Future work

Several directions would be valuable for building on the results presented in this thesis. First of all, a more systematic assessment of the reproducibility of the bilayer properties is needed. Multiple independent depositions of nominally identical NbN/MoSi bilayers should be performed to determine the reproducibility of the measured critical temperature, and to establish the degree to which the observed composition-dependent trends are affected by deposition-to-deposition variations. In parallel, a more rigorous characterization of the actual deposited thickness is paramount to ensure the correct modeling and interpretation of the bilayer properties. In the current work, difficulties were encountered in assessing the physical thickness of the deposited films, and independent measurements of the film thickness would allow the theoretical and experimental comparisons to be made on a more precise basis.

At the same time, consistent optical and electrical conditions would allow a more consistent comparison. In the current work, only the relative intensity of optical stimulation could be controlled, but not its absolute value, that could moreover be affected by different fiber dispersions and optical alignment. Similarly, electrical noise conditions, affecting properties such as the switching current, proved to be nonconstant in different times of the day and between successive cooldowns. A more consistent reproducibility of the experimental conditions could allow statistical distributions of switching currents and photon count rates to be obtained, and model the device-to-device and sample-to-sample variance.

A particularly significant improvement would be to conduct a finer temperature sweep of the photon-counting measurements, especially near the limits of detection. In the present work, the maximum operating temperature was determined using relatively coarse temperature steps. A finer sweep would allow to estimate with better precision the limits of operation, as well as distinguishing between the temperature internal detection efficiency ceases to saturate, and the temperature at which photon-induced counts can no longer be reliably distinguished from the dark-count background. Distinguishing these two regimes would provide a more complete description of the temperature-dependent detector performance, in particular through the saturation parameter σ, and would avoid treating photon sensitivity and saturated detection as a single criterion.

Finally, once the most promising region of the composition space has been identified, the nanowire geometry could be systematically optimized to further improvement of detector performance. Varying the width on a larger interval, while keeping the bilayer composition fixed, would help determine how fabrication constraints affect the detector performance further improve the already promising detection results.

More broadly, the present work should be viewed as a starting point rather than a final optimization of proximitized SNSPDs. The combination of theoretical modeling and experimental characterization developed here establishes a solid framework within

which the relevant physical questions can now be investigated more systematically. A more extensive and controlled investigation could move beyond identifying favorable compositions and towards finalizing the optimization of achievable operating temperature, saturation behavior and photon sensitivity of superconducting bilayer detectors.

References

[1] Michael Tinkham. *Introduction to superconductivity*. Courier Corporation, 2004.

[2] John Bardeen, Leon N Cooper, and J Robert Schrieffer. "Theory of superconductivity". In: *Physical Review* 108.5 (1957), pp. 1175–1204.

[3] Vitaly L Ginzburg and Lev D Landau. "On the theory of superconductivity". In: *Zh. Eksp. Teor. Fiz.* 20 (1950), pp. 1064–1082.

[4] Hiroki Takesue et al. "Quantum key distribution over a 40-dB channel loss using superconducting single-photon detectors". In: *Nature Photonics* 1.6 (2007), pp. 343–348.

[5] Boris Korzh et al. "Provably secure and practical quantum key distribution over 307km of optical fibre". In: *Nature Photonics* 9.3 (Feb. 2015), pp. 163–168.

[6] Hiroyuki Shibata, Toshimori Honjo, and Kaoru Shimizu. "Quantum key distribution over a 72 dB channel loss using ultralow dark count superconducting single-photon detectors". In: *Optics Letters* 39.17 (Aug. 2014), p. 5078.

[7] Stephen Crain et al. "High-Speed Low-Crosstalk Detection of a $^{171}Yb^{+}$ Qubit using Superconducting Nanowire Single Photon Detectors". In: (2019).

[8] S.L. Todaro et al. "State Readout of a Trapped Ion Qubit Using a Trap-Integrated Superconducting Photon Detector". In: *Physical Review Letters* 126.1 (Jan. 2021).

[9] Lixing You et al. "Superconducting nanowire single photon detection system for space applications". In: *Optics Express* 26.3 (Jan. 2018), p. 2965.

[10] Emma E. Wollman et al. "SNSPD-based detector system for NASA's Deep Space Optical Communications project". In: *Optics Express* 32.27 (Dec. 2024), p. 48185.

[11] Ziyuan Shi et al. "Performance Analysis of PPM-SNSPD System for Deep Space Optical Communications". In: *IEEE Transactions on Communications* 73.8 (2025), pp. 6221–6235.

[12] Jun Gao et al. "From Pixels to Camera: Scaling Superconducting Nanowire Single-Photon Detectors for Imaging at the Quantum-Limit". In: (2025).

[13] Emi Cora Valmai Hughes, Avinash Upadhya, and Kishan Dholakia. "Superconducting nanowire single-photon detectors for enhanced biomedical imaging". In: *Journal of Biomedical Optics* 31.11 (Mar. 2026).

[14] N. Ozana, A. I. Zavriyev, D. Mazumder, et al. "Superconducting nanowire single-photon sensing of cerebral blood flow". In: *Neurophotonics* 8.3 (2021), p. 035006.

[15] Yifan Liu et al. "Superconducting nanowire single-photon detector enhanced near-infrared II portable confocal microscopy for tissue imaging with indocyanine green". In: *Opt. Lett.* 49.22 (Nov. 2024), pp. 6349–6352.

[16] J.P. Allmaras et al. “Intrinsic Timing Jitter and Latency in Superconducting Nanowire Single-photon Detectors”. In: *Physical Review Applied* 11.3 (Mar. 2019).

[17] A. G. Kozorezov et al. “Fano fluctuations in superconducting-nanowire single-photon detectors”. In: *Physical Review B* 96.5 (Aug. 2017).

[18] Chandra M Natarajan, Michael G Tanner, and Robert H Hadfield. “Superconducting nanowire single-photon detectors: physics and applications”. In: *Superconductor Science and Technology* 25.6 (Apr. 2012), p. 063001.

[19] WeiJun Zhang et al. “NbN superconducting nanowire single-photon detector with efficiency over 90% at 1550 nm wavelength operational at compact cryocooler temperature”. In: *Science China Physics, Mechanics & Astronomy* 60.12 (Oct. 2017).

[20] Shigehito Miki et al. “High performance fiber-coupled NbTiN superconducting nanowire single photon detectors with Gifford-McMahon cryocooler”. In: *Opt. Express* 21.8 (Apr. 2013), pp. 10208–10214.

[21] B. T. Matthias, T. H. Geballe, and V. B. Compton. “Superconductivity”. In: *Rev. Mod. Phys.* 35 (1 Jan. 1963), pp. 1–22.

[22] Archan Banerjee et al. “Characterisation of amorphous molybdenum silicide (MoSi) superconducting thin films and nanowires”. In: *Superconductor Science and Technology* 30.8 (July 2017), p. 084010.

[23] I. Charaev et al. “Single-photon detection using large-scale high-temperature MgB_2 sensors at 20 K”. In: (2023).

[24] Sergey Cherednichenko et al. “Low kinetic inductance superconducting MgB_2 nanowires with a 130 ps relaxation time for single-photon detection applications”. In: *Superconductor Science and Technology* 34.4 (Feb. 2021), p. 044001.

[25] Takayuki Kubo. “Microscopic equivalence of the vortex-entry current and the depairing current in a superconducting thin-film strip”. In: (2026).

[26] Qingyuan Zhao et al. “Intrinsic timing jitter of superconducting nanowire single-photon detectors”. In: *Applied Physics B* 104 (2011), pp. 673–678.

[27] Niccolò Calandri et al. “Superconducting nanowire detector jitter limited by detector geometry”. In: *Applied Physics Letters* 109.15 (Oct. 2016).

[28] Boris Korzh et al. “Demonstration of sub-3 ps temporal resolution with a superconducting nanowire single-photon detector”. In: *Nature Photonics* 14.4 (Mar. 2020), pp. 250–255.

[29] Kristine M. Rosfjord et al. “Nanowire Single-photon detector with an integrated optical cavity and anti-reflection coating”. In: *Opt. Express* 14.2 (Jan. 2006), pp. 527–534.

[30] J. Chang et al. “Detecting telecom single photons with 99.52.07+0.5% system detection efficiency and high time resolution”. In: *APL Photonics* 6.3 (Mar. 2021).

[31] Daien He et al. “Unified Theory of Dark Count Rate and System Detection Efficiency for NbN, WSi Based Superconducting Single Photon Detectors”. In: (2025).

[32] J. Xie and H. Zhang. “Temporal and photon number resolution of superconducting nanowire single-photon detectors”. In: *Appl. Phys. B* 130 (2024), p. 113.

[33] Andrew Murphy et al. “Three Temperature Regimes in Superconducting Photon Detectors: Quantum, Thermal and Multiple Phase-Slips as Generators of Dark Counts”. In: *Scientific Reports* 5.1 (May 2015), p. 10174.

[34] M. Ejrnaes et al. “Superconductor to resistive state switching by multiple fluctuation events in NbTiN nanostrips”. In: *Scientific Reports* 9 (2019), p. 8053.

[35] Jeff Chiles et al. “New Constraints on Dark Photon Dark Matter with Superconducting Nanowire Detectors in an Optical Haloscope”. In: *Phys. Rev. Lett.* 128 (23 June 2022), p. 231802.

[36] Igor Aharonovich, Dirk R. Englund, and Milos Toth. “Solid-state single-photon emitters”. In: *Nature Photonics* 10 (2016), pp. 631–641.

[37] A. Buzzi, C. Papon, M. Pirro, et al. “Spectral tuning and nanoscale localization of single color centers in silicon via controllable strain”. In: *Nat Commun* 16 (2025), p. 8829.

[38] G. Carboni et al. “Cryo-CMOS Readout of Single-Photon Detectors for Color-Center Quantum Computers”. In: *2025 IEEE European Solid-State Electronics Research Conference (ESSERC)*. 2025, pp. 253–256.

[39] Andreas Reiserer and Gerhard Rempe. “Cavity-based quantum networks with single atoms and optical photons”. In: *Rev. Mod. Phys.* 87 (4 Dec. 2015), pp. 1379–1418.

[40] Dileep V. Reddy et al. “Superconducting nanowire single-photon detectors with 98% system detection efficiency at 1550nm”. In: *Optica* 7.12 (Dec. 2020), pp. 1649–1653.

[41] Marco Avesani et al. “Full daylight quantum-key-distribution at 1550 nm enabled by integrated silicon photonics”. In: *npj Quantum Information* 7 (2019).

[42] N A Peters et al. “Dense wavelength multiplexing of 1550nm QKD with strong classical channels in reconfigurable networking environments”. In: *New Journal of Physics* 11.4 (Apr. 2009), p. 045012.

[43] E.A. Dauler, M.A. Albota, and S. Constantine. “Frequency-correlated 1550-nm photon pairs for quantum communication”. In: *Postconference Digest Quantum Electronics and Laser Science, 2003. QELS.* 2003, 2 pp.-.

[44] Jascha A. Lau et al. “Superconducting single-photon detectors in the mid-infrared for physical chemistry and spectroscopy”. In: *Chemical Society Reviews* 52.3 (Feb. 2023), pp. 921–941.

[45] Chen L et al. “Ultra-sensitive mid-infrared emission spectrometer with sub-ns temporal resolution”. In: *Opt Express* 26.12 (2018), pp. 14859–14868.

[46] Abhilash Kulkarni, Niusha Bagheri, and Jerker Widengren. “Multiplexed Near-IR Detection of Single-Molecule Fluorescence Fluctuations Using a Single Superconducting Nanowire Single-Photon Detector”. In: *ACS Photonics* 12.4 (Mar. 2025), pp. 2233–2241.

[47] Ewan N. MacKenzie et al. “Photon counting carbon dioxide gas sensing at 2.05m wavelength”. In: *Quantum Optics and Photon Counting 2023*. Ed. by Ivan Prochazka and Roman Sobolewski. Vol. 12570. International Society for Optics and Photonics. SPIE, 2023, p. 1257009.

[48] Q Chen, F Zhou, and C Wei. “Sub-millikelvin-resolved superconducting nanowire single-photon detector operates with sub-pW infrared radiation power”. In: *Natl Sci Rev* 12.1 (Sept. 2024), nwae319.

[49] Francesco Bellei et al. “Free-space-coupled superconducting nanowire single-photon detectors for infrared optical communications”. In: *Opt. Express* 24.4 (Feb. 2016), pp. 3248–3257.

[50] Gregor G. Taylor et al. “Low-noise single-photon counting superconducting nanowire detectors at infrared wavelengths up to 29µm”. In: *Optica* 10.12 (Dec. 2023), pp. 1672–1678.

[51] Leon N. Cooper. “Superconductivity in the Neighborhood of Metallic Contacts”. In: *Physical Review Letters* 6.12 (June 1961), pp. 689–690.

[52] P. G. de Gennes. “Boundary Effects in Superconductors”. In: *Reviews of Modern Physics* 36.1 (Jan. 1964), pp. 225–237.

[53] Yachin Ivry et al. “Superconductor–superconductor bilayers for enhancing single-photon detection”. In: *Nanotechnology* 28.43 (Oct. 2017), p. 435205.

[54] N. R. Werthamer. “Theory of the Superconducting Transition Temperature and Energy Gap Function of Superposed Metal Films”. In: *Physical Review* 132.6 (Dec. 1963), pp. 2440–2445.

[55] Klaus D. Usadel. “Generalized Diffusion Equation for Superconducting Alloys”. In: *Phys. Rev. Lett.* 25 (8 Aug. 1970), pp. 507–509.

[56] N.N. Bogoljubov. “On a new method in the theory of superconductivity”. In: *Il Nuovo Cimento* 7.6 (1958), pp. 794–805.

[57] G. Eilenberger. “Transformation of Gorkov’s equation for type II superconductors into transport-like equations”. In: *Z. Physik* 214.2 (1968), pp. 195–213.

[58] F. S. Bergeret, A. F. Volkov, and K. B. Efetov. “Odd triplet superconductivity and related phenomena in superconductor-ferromagnet structures”. In: *Rev. Mod. Phys.* 77 (4 Nov. 2005), pp. 1321–1373.

[59] Matthias Eschrig. “Spin-polarized supercurrents for spintronics: a review of current progress”. In: *Reports on Progress in Physics* 78.10 (Sept. 2015), p. 104501.

[60] N. W. Ashcroft and N. D. Mermin. *Solid State Physics*. Holt, Rinehart and Winston, 1976.

[61] Wolfgang Belzig et al. “Quasiclassical Green’s function approach to mesoscopic superconductivity”. In: *Superlattices and Microstructures* 25.5 (1999), pp. 1251–1288.

[62] A V Zaitsev. “Quasiclassical equations of the theory of superconductivity for contiguous metals and the properties of constricted microcontacts”. In: *Sov. Phys. - JETP (Engl. Transl.); (United States)* 59:5 (May 1984).

[63] G. E. Blonder, M. Tinkham, and T. M. Klapwijk. “Transition from metallic to tunneling regimes in superconducting microconstrictions: Excess current, charge imbalance, and supercurrent conversion”. In: *Phys. Rev. B* 25 (7 Apr. 1982), pp. 4515–4532.

[64] A. A. Golubov, M. Yu. Kupriyanov, and E. Il’ichev. “The current-phase relation in Josephson junctions”. In: *Rev. Mod. Phys.* 76 (2 Apr. 2004), pp. 411–469.

[65] M. Yu. Kuprianov and V. F. Lukichev. “Influence of boundary transparency on the critical current of "dirty" SS’S structures”. In: *Sov. Phys. JETP* 67.6 (1988), pp. 1163–1168.

[66] Yuli V. Nazarov. “Novel circuit theory of Andreev reflection”. In: *Superlattices and Microstructures* 25.5-6 (May 1999), pp. 1221–1231.

[67] S. Kashiwaya and Y. Tanaka. “Surface states and tunneling spectroscopy of high-Tcsuperconductors”. In: *Superlattices and Microstructures* 25.5 (1999), pp. 1099–1114.

[68] A. Anthore, H. Pothier, and D. Esteve. “Density of States in a Superconductor Carrying a Supercurrent”. In: *Phys. Rev. Lett.* 90 (12 Mar. 2003), p. 127001.

[69] John R. Clem and V. G. Kogan. “Kinetic impedance and depairing in thin and narrow superconducting films”. In: *Phys. Rev. B* 86 (17 Nov. 2012), p. 174521.

[70] Songyuan Zhao et al. “Calculation and measurement of critical temperature in thin superconducting multilayers”. In: *Superconductor Science and Technology* 31.10 (Aug. 2018), p. 105004.

[71] Alex Gurevich. “Tuning vortex fluctuations and the resistive transition in superconducting films with a thin overlayer”. In: *Phys. Rev. B* 98 (2 July 2018), p. 024506.

[72] Yachin Ivry et al. “Universal scaling of the critical temperature for thin films near the superconducting-to-insulating transition”. In: *Phys. Rev. B* 90 (21 Dec. 2014), p. 214515.

[73] Xiucheng Wei et al. “Ultrathin epitaxial NbN superconducting films with high upper critical field grown at low temperature”. In: *Materials Research Letters* 9.8 (2021), pp. 336–342.

[74] A. Semenov et al. “Optical and transport properties of ultrathin NbN films and nanostructures”. In: *Phys. Rev. B* 80 (5 Aug. 2009), p. 054510.

[75] S Ezaki et al. “Localization and interaction effects in ultrathin epitaxial NbN superconducting films”. In: *Journal of Physics: Condensed Matter* 24.47 (Oct. 2012), p. 475702.

[76] W. L. McMillan. “Transition Temperature of Strong-Coupled Superconductors”. In: *Phys. Rev.* 167.2 (1968), pp. 331–344.

[77] A.M. Finkel’stein. “Suppression of superconductivity in homogeneously disordered systems”. In: *Physica B: Condensed Matter* 197.1 (1994), pp. 636–648.

[78] S. Grotowski, L. Zugliani, B. Jonas, et al. “Optimizing the growth conditions of superconducting MoSi thin films for single photon detection”. In: *Sci Rep* 15 (2025), p. 2438.

[79] Joseph Klafter and Michael F. Shlesinger. “On the relationship among three theories of relaxation in disordered systems”. In: *Proceedings of the National Academy of Sciences* 83.4 (1986), pp. 848–851.

[80] Franti šek Herman and Richard Hlubina. “Microscopic interpretation of the Dynes formula for the tunneling density of states”. In: *Phys. Rev. B* 94 (14 Oct. 2016), p. 144508.

[81] R. C. Dynes, V. Narayanamurti, and J. P. Garno. “Direct Measurement of Quasiparticle-Lifetime Broadening in a Strong-Coupled Superconductor”. In: *Phys. Rev. Lett.* 41 (21 Nov. 1978), pp. 1509–1512.

[82] S. Skalski, O. Betbeder-Matibet, and P. R. Weiss. “Properties of Superconducting Alloys Containing Paramagnetic Impurities”. In: *Phys. Rev.* 136.6A (1964), A1500–A1518.

[83] A. B. Migdal. “Interaction between Electrons and Lattice Vibrations in a Normal Metal”. In: *Sov. Phys. JETP* 7.6 (1958), pp. 996–1001.

[84] G. M. Eliashberg. “Interactions between Electrons and Lattice Vibrations in a Superconductor”. In: *Sov. Phys. JETP* 11.3 (1960), pp. 696–702.

[85] S. B. Kaplan et al. “Quasiparticle and phonon lifetimes in superconductors”. In: *Phys. Rev. B* 14 (11 Dec. 1976), pp. 4854–4873.

[86] Jhy-Jiun Chang and D. J. Scalapino. “Kinetic-equation approach to nonequilibrium superconductivity”. In: *Phys. Rev. B* 15 (5 Mar. 1977), pp. 2651–2670.

[87] J. J. Chang and D. J. Scalapino. “Nonequilibrium superconductivity”. In: *J Low Temp Phys* 31.1 (1978), pp. 1–32.

[88] Nikolai B. Kopnin. *Theory of Nonequilibrium Superconductivity*. Oxford: Oxford University Press, 2001.

[89] R. K. Pathria and P. D. Beale. *Statistical Mechanics*. 3rd ed. Elsevier, 2011.

[90] Alejandro Simon et al. “Ab initio modeling of nonequilibrium dynamics in superconducting detectors and qubits”. In: *Physical Review B* 112.17 (Nov. 2025).

[91] Allen Rothwarf and B. N. Taylor. “Measurement of Recombination Lifetimes in Superconductors”. In: *Phys. Rev. Lett.* 19 (1 July 1967), pp. 27–30.

[92] J. P. Carbotte. “Properties of boson-exchange superconductors”. In: *Rev. Mod. Phys.* 62 (4 Oct. 1990), pp. 1027–1157.

[93] Philip B. Allen and Božidar Mitrović. “Theory of Superconducting Tc”. In: ed. by Henry Ehrenreich, Frederick Seitz, and David Turnbull. Vol. 37. Solid State Physics. Academic Press, 1983, pp. 1–92.

[94] A. G. Kozorezov et al. “Quasiparticle-phonon downconversion in nonequilibrium superconductors”. In: *Phys. Rev. B* 61 (17 May 2000), pp. 11807–11819.

[95] Alex D. Semenov, Gregory N. Gol’tsman, and Alexander A. Korneev. “Quantum detection by current carrying superconducting film”. In: *Physica C: Superconductivity* 351.4 (2001), pp. 349–356.

[96] D. Yu. Vodolazov. “Single-Photon Detection by a Dirty Current-Carrying Superconducting Strip Based on the Kinetic-Equation Approach”. In: *Phys. Rev. Appl.* 7 (3 Mar. 2017), p. 034014.

[97] A Engel et al. “Detection mechanism of superconducting nanowire single-photon detectors”. In: *Superconductor Science and Technology* 28.11 (Sept. 2015), p. 114003.

[98] Alejandro Simon et al. “Fast Real-Axis Eliashberg Calculations: Full-bandwidth solutions beyond the constant density of states approximation”. In: *arXiv preprint arXiv:2603.18199* (2026).

[99] Alejandro Simon et al. “Ultrafast dynamics and light-induced superconductivity from first principles”. In: *arXiv preprint arXiv:2603.18182* (2026).

[100] U. Fano. “Ionization Yield of Radiations. II. The Fluctuations of the Number of Ions”. In: *Phys. Rev.* 72.1 (1947), pp. 26–29.

[101] A. N. Zotova and D. Y. Vodolazov. “Photon detection by current-carrying superconducting film: A time-dependent Ginzburg-Landau approach”. In: *Phys. Rev. B* 85 (2 Jan. 2012), p. 024509.

[102] Yu. P. Korneeva et al. “Superconducting single-photon detector made of MoSi film”. In: *Superconductor Science and Technology* 27.9 (2014), p. 095012.

[103] G. N. Gol’tsman et al. “Picosecond superconducting single-photon optical detector”. In: *Applied Physics Letters* 79.6 (2001), pp. 705–707.

[104] Francesca Incalza et al. “Fast-Recovery Epitaxial NbN Superconducting Nanowire Single-Photon Detectors with Saturated Efficiency at 1550 nm in Liquid Helium”. In: *Nano Letters* 26.21 (May 2026), pp. 6848–6856.

[105] V. B. Verma et al. “High-efficiency superconducting nanowire single-photon detectors fabricated from MoSi thin-films”. In: *Opt. Express* 23.26 (Dec. 2015), pp. 33792–33801.

[106] Misael Caloz et al. “High-detection efficiency and low-timing jitter with amorphous superconducting nanowire single-photon detectors”. In: *Applied Physics Letters* 112.6 (2018), p. 061103.

[107] Andrew J. Kerman et al. “Constriction-limited detection efficiency of superconducting nanowire single-photon detectors”. In: *Applied Physics Letters* 90.10 (Mar. 2007).

[108] J. J. Renema et al. “Universal response curve for nanowire superconducting single-photon detectors”. In: *Phys. Rev. B* 87 (17 May 2013), p. 174526.

[109] QNN group. *qnngds*. Version current. 2026. `https://github.com/qnngroup/qnngds`.

[110] Adam McCaughan, Alex Tait, and contributors. *phidl*. Version current. 2023. `https://github.com/amccaugh/phidl`.

[111] Quantum Nanostructures and Nanofabrication Group. `https://qnn-rle.mit.edu/`.

[112] John R. Clem and Karl K. Berggren. “Geometry-dependent critical currents in superconducting nanocircuits”. In: *Phys. Rev. B* 84 (17 Nov. 2011), p. 174510.

[113] Andrew J. Kerman et al. “Kinetic-inductance-limited reset time of superconducting nanowire photon counters”. In: *Applied Physics Letters* 88.11 (2006), p. 111116.

[114] Andrew J. Kerman et al. “Electrothermal feedback in superconducting nanowire single-photon detectors”. In: *Phys. Rev. B* 79 (10 Mar. 2009), 100509(R).

[115] Anthony J. Annunziata et al. “Reset dynamics and latching in niobium superconducting nanowire single-photon detectors”. In: *Journal of Applied Physics* 108.8 (2010), p. 084507.

[116] Anthony J Annunziata et al. “Tunable superconducting nanoinductors”. In: *Nanotechnology* 21.44 (Oct. 2010), p. 445202.

[117] D. M. Mattox. *Handbook of Physical Vapor Deposition (PVD) Processing*. 2nd ed. William Andrew/Elsevier, 2010.

[118] AJA International. *ATC Orion 8 Sputtering System*. `https://www.ajaint.com/system-atcflagship`.

[119] Xiaofu Zhang et al. “Physical properties of amorphous molybdenum silicide films for single-photon detectors”. In: *Superconductor Science and Technology* 34.9 (Aug. 2021), p. 095003.

[120] Elionix Inc. *ELS-F125 Electron Beam Lithography System*. `https://sts-elionix.com/product/els-f125/`.

[121] Elionix Inc. *ELS-HS50 Electron Beam Lithography System*. `https://sts-elionix.com/product/els-hs50/`.

[122] ZEON Corporation. *ZEP520A Technical Report*. Tech. rep. ZEON Corporation. `https://smif.pratt.duke.edu/sites/smif.pratt.duke.edu/files/operating/ZEP520ATechReport.pdf`.

[123] Plasma-Therm LLC. *210RL RIE Etch Tool*. https://corial.plasmatherm.com/en/products/corial-210rl-rie-etch-tool.

[124] Henkel. *Loctite GC 10 SAC305T3 Solder Paste*. https://www.farnell.com/datasheets/1952622.pdf.

[125] General Electric (GE). *GE Varnish*. https://www.cmr-direct.com/shop/category/all-wiring-cryogenic-wiring-heatsinking-encapsulation-ge-varnish-18.

[126] Film Sense. *FS-1 Multi-Wavelength Ellipsometer*. https://film-sense.com/film-sense-multi-wavelength-ellipsometer/.

[127] Andrew E. Dane et al. "Bias sputtered NbN and superconducting nanowire devices". In: *Applied Physics Letters* 111.12 (2017), p. 122601.

[128] Mariia Sidorova et al. "Electron energy relaxation in disordered superconducting NbN films". In: *Phys. Rev. B* 102 (5 Aug. 2020), p. 054501.

[129] Quantum Design. *Magnetic Property Measurement System (MPMS3)*. Accessed: 2026-08-23. https://qdusa.com/products/mpms3.html.

[130] A. I. Larkin and Yu. N. Ovchinnikov. "Nonlinear Conductivity of Superconductors in the Mixed State". In: *Soviet Physics JETP* 41.5 (1975). Russian original: Zh. Eksp. Teor. Fiz. 68, 1915–1927 (1975), pp. 960–965.

[131] Yu. P. Korneeva et al. "Different Single-Photon Response of Wide and Narrow Superconducting MoSi Strips". In: *Physical Review Applied* 13.2 (Feb. 2020).

[132] JDS Fitel. *HA9 Optical Attenuator*. https://assetrelay.com/shop/media/HA97E_Specification_Sheet.pdf.

[133] *Model 2002 Multimeter User's Manual*. Revision E. Keithley Instruments. 1996.

[134] S. Frasca et al. "Determining the depairing current in superconducting nanowire single-photon detectors". In: *Phys. Rev. B* 100 (5 Aug. 2019), p. 054520.

[135] Ruike Yang et al. "Study on structural, mechanical, electronic properties and Debye temperature of four NbN structures". In: *Computational and Theoretical Chemistry* 1196 (2021), p. 113113.

[136] Stefan Strohauer et al. "Current crowding–free superconducting nanowire single-photon detectors". In: *Science Advances* 11.13 (2025), eadt0502.